January 2015

Development of Particle Image Velocimetry for Plasma Induced Flow Measurements

Bhavini Singh
Purdue University

Follow this and additional works at: https://docs.lib.purdue.edu/open_access_theses

PURDUE UNIVERSITY
GRADUATE SCHOOL
Thesis/Dissertation Acceptance

This is to certify that the thesis/dissertation prepared

By Bhavini Singh

Entitled
Development of Particle Image Velocimetry for Plasma Induced Flow Measurements

For the degree of   Master of Science in Aeronautics and Astronautics   ▼

Is approved by the final examining committee:

Sally Bane
_____
Chair

Pavlos Vlachos

John Sullivan

To the best of my knowledge and as understood by the student in the Thesis/Dissertation Agreement, Publication Delay, and Certification Disclaimer (Graduate School Form 32), this thesis/dissertation adheres to the provisions of Purdue University's "Policy of Integrity in Research" and the use of copyright material.

Approved by Major Professor(s): Sally Bane

Approved by: Weinong Chen   12/4/2015
         Head of the Departmental Graduate Program   Date

DEVELOPMENT OF PARTICLE IMAGE VELOCIMETRY FOR PLASMA

INDUCED FLOW MEASUREMENTS

A Thesis

Submitted to the Faculty

of

Purdue University

by

Bhavini Singh

In Partial Fulfillment of the

Requirements for the Degree

of

Master of Science in Aeronautics and Astronautics

December 2015

Purdue University

West Lafayette, Indiana

For Mummy, Papa and Didi

ACKNOWLEDGEMENTS

lab-mates, especially to Lalit, Prashanth and Ravi. Thanks Lalit for being a sounding board, and for all the helpful advice. Thanks Prashanth for teaching me plumbing and for helping me set-up one of the most important parts of any experiment. Thanks Ravi for always letting me bother you for help. Thank you to my parents. I don't think I can ever be able to express how grateful I am for every opportunity you have given me, for all the sacrifices you have made for your children, and for always thinking of us first. You are the reason I am where I am, and the reason behind any successes I may achieve. I love you guys. Thanks to my sister, you have managed to be my guardian, my best friend and my home away from home. I would have been miserable here without you. Thanks to Stuart for being the most loving and patient partner I could have asked for. Your work ethic is something I aspire to. Thank you for putting up with me ☺. Thanks to my best friends Nanda and Ashley for being an important part of my day to day, and for always reminding me how wonderful it is not to be a broke graduate student.

Finally, thank you to the First Year Engineering department and the Aeronautics and Astronautics department for providing me with assistantships that have funded my masters education.

TABLE OF CONTENTS

LIST OF TABLES

LIST OF FIGURES

ABSTRACT

Singh, Bhavini. M.S.A.A., Purdue University, December 2015. Characterization of Flow Control Actuators Based on Spark Discharge Plasmas Using Particle Image Velocimetry. Major Professor: Sally Bane.

There has been an increased interest in the use of flow control in aerodynamics and combustion to improve efficiency and reduce emissions. Plasma flow control is one way by using active flow control affect these desired changes. Spark plasma actuators have capabilities of inducing heat and momentum to the flow field. The flow field generated by this plasma induces complex pressure and temperature gradients that lead to the development of complex flow structures. The experiment described in this research is particularly difficult due to its small scale, and the dynamic range of velocities that are induced by the flow field. This flow field is yet to be quantified by previous research. The flow field generated by spark plasma has not been quantified to date. The development of a set-up to capture and process preliminary findings of the flow field generated by a spark plasma under quiescent conditions is imperative to understanding the capabilities of this plasma actuator.

A 2-D PIV system is used to analyze the flow field from a spark plasma actuator. An Nd:YAG laser is pulsed at a frequency of 10kHz to illuminate the test section. A Photron FASTCAM SA-Z camera is operated at 20,000 fps to take double frame images of the flow field. The flow field is generated between two electrodes connected to a DC power supply containing a high voltage transformer rated up to 45kV. The test section enclosed in a steel chamber with fused quartz windows for optical access is seeded with aluminum dioxide (Al_2O_3) particles with a manufacture specified nominal diameter of 0.3μm. PRANA (PIV Research and ANAlysis), a PIV processing software is used to process the captured images of the flow field. A multipass, method with deform is used to

process instantaneous velocity fields and an ensemble correlation with deform is used to process the average velocity field. Robust phase correlation is used in each of the methods to correlate image pairs. Velocity field interpolation is performed using a bicubic interpolation method and image interpolation back onto the rectilinear grid is done using a windowed-sinc filter with a blackman window. 64 x 64 pixel interrogation windows are used to analyze the instantaneous flow field and 48 x 48 pixel interrogation windows are used to analyze the ensemble correlated flow field. Vector post processing is performed using a median filter for the universal outlier detection method, and a Gaussian smoothing function is applied on the velocity field in the initial passes.

Three different phase averaging techniques are examined to determine the best method to assess twenty sets of instantaneous data taken under similar conditions. Ensemble correlation, ensemble averaging and correlation of ensemble images are the three methods tested. A final determination of the best method is left for future work, but for the purposes of this experiment, ensemble correlation was used to present phase averaged images as prior art found this to be the best way to increase signal to noise ratio (SNR) among the three. Ensemble averaging conserves the most information contained in the instantaneous flow field. The repeatability of the flow field is assessed and the turbulent nature of the flow field is revealed. Voltage measurements show that there is varying standard deviation in the voltage during the spark. Analysis of the flow field shows 70-90% deviations in magnitude of velocity. Preliminary results show flow concentrated in the center of the electrode gap at initial times, followed by an outward flow toward the surrounding gas. The effect of electrode gap on the flow field generated is also briefly studied, with larger gaps showing higher magnitudes of velocity and faster decay rates.

The system is capable of measuring flow fields generated by the spark plasma and a characterization of the process is possible in the future using the some improvements to the set-up.

CHAPTER 1. INTRODUCTION & BACKGROUND

1.1   Motivation

Over the past several decades, the cost of hydrocarbon fuels and fast depletion of natural resources has increased and therefore there is a critical need for efficiency in aircraft to reduce fuel consumption. With the fast-paced globalization that is taking place in the world, there is a necessity to travel large distances in short periods of time. With 80% more occupancy than other forms of transportation [1] and being a large contributor to employment and the world's economy, the demand for air transport will only increase. Higher demand for air transportation means more fuel usage. The booming American commercial aviation industry used about 16 billion gallons of fuel in the year 2014 costing up to USD 47 billion compared to 2004 when 18 billion gallons of fuel was used with a total cost of USD 20.8 billion [2]. It is clear that although more fuel-efficient vehicles are being built now compared to a decade ago, the rate of increase in fuel cost is too rapid to reflect any monetary benefit from the increased efficiency. With the projected increase in passengers and flights, this cost is only set to rise. In the year 2013, 705 million tons of carbon dioxide waste was produced by the commercial aviation industry [1]. In order to minimize cost, curb the waste, attempt to stay the depletion of a natural resource and ensure the continued success of the aviation industry, numerous approaches have been taken. According to an ICAO environmental report in 2010, the efficiency of aircraft has increased by 40% over the last decade, with projections of further increase by 2025 [3]. The same report states that it is expected that 94% of commercial aircraft will have next-generation technology geared toward increasing aircraft efficiency by 2036. A partnership between NASA, the US Air Force, and the Boeing Company to develop blended wings to reduce interference drag is one example of recent innovations geared toward efficiency

improvement in aircraft. This particular collaboration resulted in fuel savings of 10,000 gallons per year for 737-700 aircraft [4].

Flow control is one method that is being used to increase the efficiency of aircraft. It is also being investigated as a method to improve the efficiency of jet engines while reducing noise as well as emissions and as an aid in thermal management of supersonic aircraft. Flow control involves alteration of flow close to the surface of an aerodynamic body and can be done actively or passively. It often involves either inducing or delaying laminar to turbulent transition or separation. Flow control may be used to induce turbulence so as to enhance mixing of flow in order to delay separation and reduce pressure drag or enable the aircraft to achieve higher angles of attack and reduce take-off and landing distances [5]. Delaying transition from laminar to turbulent on the other hand may be useful in reduction of skin friction thus reducing drag, improving fuel efficiency and enabling higher flight speeds. A desirable flow control actuator would be one that has the capability of being turned on or off as needed, is relatively inexpensive to manufacture, does not add appreciable weight to the aircraft and that is capable of reducing drag so as to minimize expenditure on fuel, minimize pollution and increase aircraft range and speed.

Plasma actuators for flow control is a growing field of interest with a great deal of research showing the promise of dielectric barrier discharge actuators to improve airfoil performance. The relatively small amount of current research on flow control using spark/arc plasmas focuses on harnessing the localized energy input of the plasma to increase the local temperature and pressure. In the current work, we begin characterization of new methods of flow control based on spark plasma actuators. Instead of using only the energy input of the plasma, we propose that the local fluid dynamics induced by the spark discharge can be used to change the surrounding flow field. The complex flow field induced by the spark is yet to be fully characterized. To be able to identify ways to use spark plasma as a flow control mechanism, it is critical to first understand the flow field generated by the spark. Particle image velocimetry (PIV) can be used to observe and measure the time-dependent flow field and facilitate this understanding. The goal of this work is to design and develop such a PIV system and demonstrate its capabilities to

measure the spark-induced flow fields on the relevant spatial and time scales. Future work will focus on the characterization of the flow field generated by the plasma.

1.2   Aerodynamic Flow Control

The simplest definition of flow control is the process of alteration of the behavior of a flow field. Gad el Hak [6] quotes Flatt [9] as having defined boundary layer flow control, specifically, as: "Boundary layer control includes any mechanism or process through which the boundary layer of a fluid flow is caused to behave differently than it normally would were the flow developing naturally along a smooth straight surface". There are two main categories of flow control mechanisms, passive and active flow control. Passive flow control has been used on aircraft for decades and typically involves modifications made to the geometry of an aircraft to change the near-surface flow structure. Vortex generators, flaps and slats are some examples of passive flow control devices. Passive flow control devices, as the name may suggest, affect the flow in a steady manner and are always "turned on". In many cases it has been noted that passive flow control devices add weight to the aircraft, affect undesirable change to the flow in some instances and pose the threat of malfunction due to wear [5]. Contrarily, active flow control devices require an event to initialize the actuators so that they may change the flow as desired. These have the capability of being turned on and off, and in the case of plasma actuators, add negligible if any additional weight to the aircraft. Plasma flow control, the main focus of this research, is one example of an active flow control mechanism that is not in constant interference with the air flow.

To examine how to improve aircraft efficiency using flow control, it is necessary to understand the physical factors that govern motion of fluid close to the aircraft surface. Ludwig Prandtl introduced the boundary layer theory to the world in 1904 [10]. This unified theoretical hydrodynamics with experimental observations and explained that the flow over a body can be divided into two regions: one where viscosity can be ignored, and one where viscosity cannot be ignored. The latter is called the boundary layer, a thin region over the surface of the body in the flow where viscous effects are significant. A boundary layer can be laminar or turbulent. In the laminar boundary layer, the fluid moves in the

same direction everywhere within the region, however in a turbulent boundary layer, there is mixing of the fluid and non-uniformity or chaos in the direction of fluid flow.

In many cases, turbulence leads to increased drag, which is undesirable for any aircraft. Total drag experienced on an aircraft includes pressure drag and skin friction drag. Pressure drag includes induced drag (in subsonic flows) or wave drag (in transonic and supersonic flows) as well as form drag. Flow separation increases pressure drag, as flow detaches from a surface, a separation bubble forms between the flow and the surface. This separation bubble adds downward force from the pressure in the bubble, for example in the case of wings. The modified shape that results from separation affects the flow characteristics over the body and reduces lift and adds drag. Turbulent flow structures such as vortices that can arise due to flow separation, baroclinic torque, viscous forces, increase skin friction drag over an aerodynamic body. Though there are cases where turbulent flow increases skin friction drag, it does have some desirable attributes. Mixing is enhanced in turbulent flows, a useful feature for combustors and for delaying flow separation. Turbulent boundary layers enhance mixing of the flow close to the aerodynamic surface and that above it, avoiding the zero velocity close to the surface of the body that leads to boundary layer separation and hence reduced form drag. Turbulent flows also have higher rates of heat and mass transfer, a useful feature for heat exchangers.

Different alterations to the boundary layer can be made via flow control. Affecting the boundary layer to delay transition is one such alteration. This can be desirable if skin friction drag needs to be decreased on an aerodynamic body. If one thinks of the initial turbulent structures that begin to form in an otherwise laminar flow reagime in a simplistic form as waves in one phase, then it would be possible to diminish these waves by countering the turbulent flow. New waves that are out of phase to those in the turbulent structure can be introduced into the flow and an interaction between the two out of phase flow structures retard the onset of turbulence. The onset of separation can be delayed by inducing momentum into the flow close to the surface of an aerodynamic body to speed up the flow or by inducing turbulence in the flow to enhance mixing close to the boundary layer to prevent flow separation. In addition to lower fuel consumption and therefore cost,

a reduction in overall drag would mean higher attainable aircraft speeds, longer range for aircraft as well as the ability to carry heavier payloads.

A great deal of research has focused on understanding the physics behind the transition phase of flow from laminar to turbulent. Numerous factors have been found to affect or enhance this transition, with some better understood than others. The roots of these disturbances are many. Amplification of Tollmien-Schlichting (T-S) waves has given insight into the route of the transition process, as have Taylor-Gortler vortices. In order to delay transition, the random forcing disturbances discussed by Reshotko, or the cause of the amplification of T-S waves or onset of Taylor Gortler vortices need to be suppressed. Altering the shape of the velocity profile is necessary to prevent the growth of instabilities that lead to turbulence and separation. Inducing wall motion via use of flexible coatings was found to be one mechanism of flow control that can be used to delay transition [6]. Heating and cooling of walls can also be used to change viscosity effects on the flow and hence affect the boundary layer. For example, cooling of the walls has been found to reduce amplification of T-S waves [6]. Wave cancellation techniques have also been theoretically tested as methods of delaying transition. A mechanical representation of these via an active flow control device could be used to delay transition to turbulence. Liepman et al [6] use active feedback control methods to amplify then cancel Tollmien-Schlichting waves to delay transition. Passive methods also exist that delay transition [7] and have found that adding a well-defined roughness element to an aerodynamic body can delay transition of a boundary layer and reduce skin friction drag.

Similarly, the onset of flow separation can be delayed using flow control. Flow separation is caused due to the presence of an adverse pressure gradient. The velocity of the boundary layer close to the wall goes to zero leading to flow reversal. Adding momentum to the region close to the wall has been found to be an effective method of separation control. Adding momentum accelerates the flow close to the wall, thus ensuring that velocity of the flow at the wall is not zero. In such cases, turbulent flow is more favorable for flow attachment since the flow mixing in the boundary layer combines flow moving in either direction, while adding momentum to the flow close to the wall and preventing flow reversal. Adding wall jets directed in the direction of free stream flow also

helps prevent separation, as it accelerates flow close to the surface of the wall. The added momentum to the initial flow delays flow separation due to the adverse pressure gradient created from wall friction slowing down flow close to the wall. Acoustic excitations have also been used to induce flow reattachment [11]. Magnetohydrodynamic (MHD) flow control has also been used [11] where the flow is converted into an electrically conducting fluid (such as plasma) and interacts with the magnetic field created around it. Suction is another method used for postponing flow separation where small amounts of fluid are drawn very close to the surface of the aerodynamic body. The suction brings in higher speed flow that is closer to the freestream into the region with low speed flow in the boundary layer. This accelerated flow close to the surface of the body preventing an occurrence of 0 velocity close to the surface as well as flow reversal.

1.3   Plasma Flow Control

Using plasmas to generate the effects in the boundary layer discussed in the previous section is the main focus of this thesis. Successful implementation of plasma actuators has been detailed by numerous researchers [14]-[28]. Plasmas add momentum, vorticity and/or heat to the flow or induce turbulence and mixing through several different mechanisms such as high temperature and high voltage gas discharges [5]-[19]. Plasma actuators are appealing because they do not require the use of any moving mechanical parts, can be turned on and off, and can be actuated at high frequencies. There are cold or non-thermal plasma actuators as well as hot or thermal plasma actuators. In cold plasmas, the electron temperature is very high while the temperature of the large species is close to ambient, therefore it is cool to the touch. Hot plasmas on the other hand approach a state of local thermodynamic equilibrium [17], therefore when large amounts of energy are added to a region via an actuator, the gas in the region gets heated as well. These active flow control devices generally consist of two electrodes between which the plasma is generated.

The most popular method of flow control using non-thermal plasma has been the dielectric barrier discharge (DBD) plasma actuator, first developed in the early 2000s [18]. One of the electrodes in a single dielectric barrier discharge (SDBD) plasma actuator is

fully covered in dielectric material while the other is left exposed. A high voltage is applied between the electrodes and ionization of air in the region of the gap begins. The plasma formed generates a body force on the gas in the surrounding region, accelerating it away from the exposed electrode [19]. This induced flow is generally referred to as the *ionic wind*. For flow control, the DBD actuators is used to generate a wall jet that alters the boundary layer profile close to the surface. Since its first implementation, the DBD plasma actuator has been further researched, improved and employed in a variety of applications such as boundary layer transition delay and control of vortex shedding [14],[20]. However, it is widely acknowledged that while DBD plasma actuators allow for high frequency actuation, the body force it can exert on the flow, and hence the momentum it can add to the flow, is fairly small. The maximum induced flow velocity tangential to the surface is on the order of <10 m/s, even with multiple actuators [20]. Also, non-thermal plasma actuators are currently limited to flow control applications near atmospheric pressure and with free-stream velocities on the order of a few hundred meters per second or lower [21].

Other non-thermal plasmas such as corona discharge actuators have been used for flow control purposes, since they also produce an ionic wind. The electric wind itself has been found to have relatively small velocities of less than 5 m/s [5] with the maximum velocity obtained about 1 mm from the wall region where the actuators are embedded.

A small number of researchers have been working on using electric sparks or arcs for flow control, primarily focusing on two methods. The first method is the plasma jet, where a spark is used to rapidly heat and pressurize the air in a small surface cavity, causing the hot, high-pressure air to rush out of the cavity through a nozzle to form a jet. This flow control mechanism has been studied by various researchers over the past 10 years, beginning with the SparkJet device for supersonic flow control [22] and continuing with research in the past few years for both subsonic [23]-[24] and supersonic [25]-[27] applications. A small amount of work has been done on a second electrical arc mechanism referred to as arc filaments. Arc filament actuators have been developed where localized heating of the flow by the electric arc is used to excite instability modes of high-Reynolds number jets to increase mixing or reduce noise [28]-[30]. Thus far, arc filament actuators have been studied for flow control by only a couple of research groups.

In prior work [31] it was observed that a thermal spark discharge initiates a highly complex flow field that is strongly dependent on the discharge energy and electrode/spark gap geometry. Leonov and colleagues [32], [33] have also extensively studied the mechanism of local gasdynamic instability and jet formation in long spark discharge channels and proposed applications for supersonic mixing and ignition. To assess the possible mechanisms for controlling the external flow, it is critical to first characterize and understand the fluid dynamics induced by the spark discharge.

1.4   Spark Plasma

To generate a spark, the surrounding medium (in our case air) needs to be ionized. To do this, a large amount of energy must be deposited in a small region so as to breakdown the air. The voltage breakdown threshold is dependent on the gap between the electrodes as well as the pressure in which the experiment is being performed. At atmospheric pressure, with electrode gaps on the order of 1-10 mm, 10s of kV are required to breakdown air. The spark lasts a short duration during which a bright channel (like miniature lightning) can be seen in the gap. This dissipates quickly leaving a glow in the channel of hot plasma formed from the ionized molecules. A shockwave accompanies the spark due to the very fast rise in pressure and temperature in the spark channel. The rate at which energy is deposited in the gap is faster than the acoustic time scale.

The relationship between breakdown voltage necessary for a discharge to occur and the pressure and gap length is given by Paschen's Law, discovered by Friedrich Paschen in 1889. It relates the breakdown voltage to the product of pressure and gap distance, p*d. In his experiments, Paschen found that if the pressure between two plates was reduced, the breakdown voltage also decreased to a minimum value after which further decrease in pressure resulted in an increase in breakdown voltage. The same was found to be true regarding the distance between the plates: for decreasing gap distance, the voltage breakdown threshold decreased to a minimum after which a further decrease in distance between the plates led to an increase in the breakdown threshold.

Figure 1-1 shows a Paschen curves for various gases at relatively low pressures < 100 Torr. The curves show a minimum breakdown voltage, also known as Stoletov's point, where the cost of ionization is minimized.
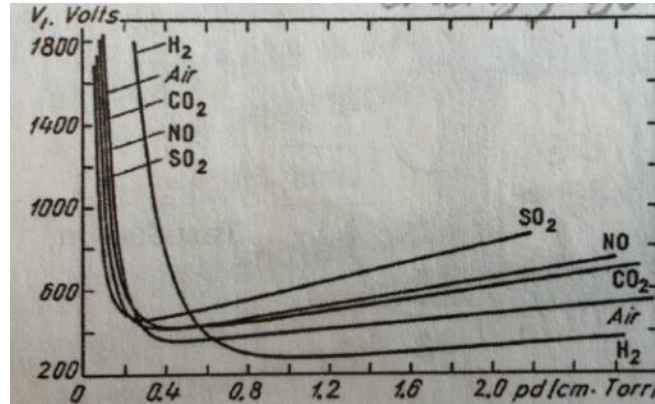
Figure 1-1: Paschen curve showing relationship between voltage and pressure and electrode gap distance at low pressures for several gases [34]

To understand the breakdown mechanisms involved in a spark discharge, it is necessary to explain the Townsend mechanism. When an electric field between two electrodes is large enough, free electrons are accelerated from the cathode. During the acceleration process, the electrons come into contact with air molecules and knock off more electrons from the air molecules creating ions. The electrons are continuously accelerated toward the anode while spreading out due to diffusion, while the ions remain mostly fixed in space. In low pressures, this is the mechanism for glow discharges.

At values of p*d greater than 200 torr·cm and at very high voltages like those needed for spark generation in STP, the Townsend mechanism is no longer valid. The Townsend theory breaks down due to several reasons, including that the loss of electrons due to diffusion is less likely at higher pressures and that the secondary emission due to ion impact is ignored because the ions are practically immobile during the short duration of the spark. For higher pressures (atmospheric pressure and higher) and the higher associated voltages, streamer breakdown is used to more effectively explain the breakdown mechanism for sparks. A streamer can be described as a very thin ionized channel between the electrodes. Large electric fields in the region of the two electrodes accelerate electrons

as in the case of Townsend breakdown, forming the primary avalanche. The exact mechanism of streamer formation involves photoionization in the region of the primary avalanche by energetic photons emitted by excited atoms in this primary avalanche. In air, these atoms are nitrogen atoms. When the space charge created by the primary avalanche is close to the external field applied in the gap, a streamer forms. The location where this condition is reached determines whether a positive or negative (cathode directed or anode directed) streamer will be formed. If this condition is met a distance away from the cathode less than the distance to the anode, the avalanche transforms into a streamer which is anode directed. Considering a cathode directed streamer, the electrons formed by the photons from the primary avalanche then lead to secondary avalanches as can be seen in Figure 1-2. At time t_2 the secondary avalanche is pulled into the streamer. When the secondary avalanche is pulled into the thin streamer channel, the electrons combine with the ions from the primary avalanche to form a quasi-neutral plasma as well as excite more atoms leading to formation of more photons. This process continues leading the growth of the streamer from the anode to the cathode. In an anode directed streamer, the difference is that since the electrons are travelling in the direction of the streamer, the secondary avalanches are formed ahead of the streamer. The electrons join the path of ions left by the secondary avalanches and form the plasma.
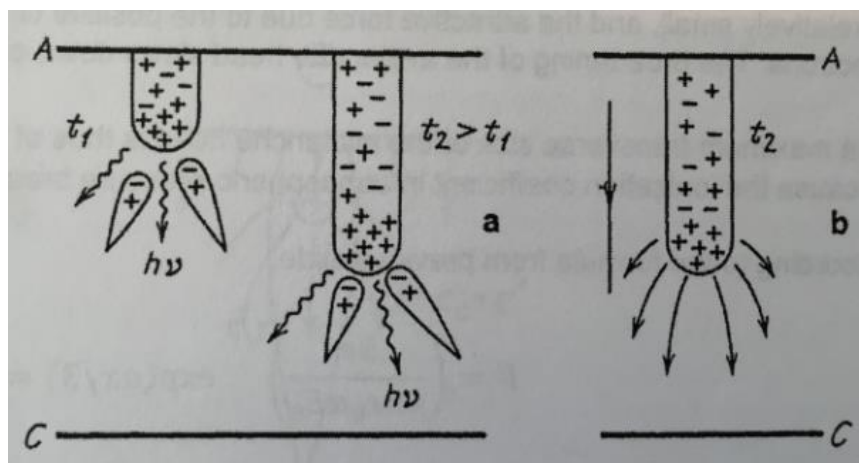
Figure 1-2: Cathode directed streamer discharge showing combination of primary and secondary avalanches into the streamer [34]

The continuous bombardment of the air molecules by high energy electrons leads to transfer of a large amount of energy into the gap resulting in high temperatures in the region of the spark. The violent nature of the breakdown leads to thermal instabilities in the region. The plasma created in this manner is very hot and it is suggested that the degree of ionization increases with an increase in this thermal temperature. This large temperature increase leads to high pressure in the spark channel, producing a shock wave that propagates away from the electrode gap. The shock wave geometry will depend on the electrode configuration; for example, for two pointed electrodes separated by a few millimeters, the shock wave is cylindrical near the center of the gap and spherical near the electrode surfaces [31]. This shock wave geometry is responsible for the complex flow field that follows its departure [31], [35]. The spark duration is less than 1μs. If the spark duration is very short, then the shock wave also exists for a very short period of time. This shock wave can be used to control high-speed flow over a body by acting as an obstacle [28]. Prior work [28], [29] also suggests that should these sparks be pulsed, the shocks can be generated at fixed intervals and used to manipulate flow even more effectively. In the case of a single pulse however, once the spark and shock dissipate, the mechanisms affecting the flow include the conduction of the heat deposited in the channel to the surrounding region as well as the motion of the gas due to the shock wave. This is also part of the spark plasma flow control mechanism for lower speed flows.

1.5   Particle Image Velocimetry

Particle image velocimetry (PIV) has been widely used for nearly three decades and there has been constant work to improve and advance the technique. PIV developed from a need by researchers to understand turbulent flows [36]. Using 2-D PIV has proved useful in identifying turbulent flow structures and quantifying velocity fields that were previously characterized only qualitatively at best. Stereoscopic PIV is a technique which allows one to measure all three components of velocity. There are numerous other PIV measurement techniques geared to specific research requirements. For example micro-PIV allows for

measuring flows in microfluidic devices and tomographic-PIV is an even more accurate way of obtaining 3-D velocity fields.

PIV involves seeding a test section with tracer particles to observe the flow second hand. These particles are expected to follow the flow almost exactly. The test region is illuminated by a pulsed high power light source and imaged with a high speed camera. In 2-D PIV the camera is placed perpendicular to the test section which is placed in the thinnest region of the light sheet created from the light source. Once images are taken, various processing techniques are used to determine the displacement of tracer particles, and hence quantify two components of flow velocity. The design and set-up of the PIV system and the analysis used primarily depends on four factors and which take priority: the required spatial and temporal resolutions and the minimum and maximum flow velocities expected [39].

1.5.1   Tracer Particles

The PIV measurement technique is indirect as it involves seeding the test section with tracer particles and measuring the motion of these particles to extract the velocity. Melling et al. [37] and Hamdi et al. [38] give thorough analyses on different tracer particles and how they behave under varying velocities, temperatures and electric fields. The three main characteristics of tracer particles that are most desirable are:

(1) The tracer particles should be small enough to follow the flow accurately but also large enough to be visible by the camera [38],[39];

(2) The size and density of the particles need to be such that sedimentation and inertial effects can be neglected [39];

(3) The physical characteristics of the particles should be such that charge and polarization effects are negligible [39].

One of the main physical factors that must be carefully considered is the size and density of the tracer particles. Particles that are too large experience significant velocity lag and are unable to follow the flow accurately. The Stokes number and settling time of tracer particles is thus a good indicator of how well the particles will be expected to follow the flow. The Stokes number and settling time are given by Equations (1.1) and (1.2):

$$Stk = \frac{\tau_s u_0}{l} \tag{1.1}$$

$$\tau_s = \frac{d_p^2 \rho_p}{18\mu} \tag{1.2}$$

The Stokes number defines how closely the particles can follow the flow. For Stokes number less than or equal to 10^{-3} the deviation of the tracer particles is negligible [42]. In flows where there is an observed shock wave that the tracer particles must follow, it was found that particles less than 0.3 µm recovered relatively faster from the shock compared to larger particles [37]. Titanium dioxide (TiO_2) and aluminum oxide (Al_2O_3) have been found to be good tracer particles for high temperature flows such as combustion [39]. Using particles with densities close to the density of the fluid they are tracking helps alleviate the issue of sedimentation. In cases where the density of a particle is much greater than the density of the fluid, the relaxation time is a good indication of how long the tracer particles will be able to "hang" in the seeded fluid awaiting fluid motion to follow.

Ensuring that tracer particle response time across shocks is fast enough is even more problematic. The high pressure difference before and after the shock requires that relaxation time and Stokes number of the tracer particles be further analyzed beyond the subsonic speed analysis presented above. It has been found by numerous authors that using experimental data to observe the response of different tracer particles across shocks has been the best method for particle selection [40],[41],[42]. Most literature recommends the use of titanium dioxide tracer particles with diameters less than 0.5µm [40]. Urban and Mungal [41] found that for the titanium dioxide and aluminum particles tested, the nominal diameter of the particles was not an accurate predictor of actual particle sizes as some were much larger. Urban found in his PhD thesis [42] that while nominal diameters of titanium dioxide of 0.015 µm theoretically yielded response times on the order of 8.2 ns and 0.3 µm aluminum oxide particles yielded response times of 2.3 µs, the actual response times were an order of magnitude higher due to particle agglomeration. Urban found that the actual agglomerated particle size could only be found experimentally. He discovered that the actual response time of titanium dioxide was 3.5 µs, corresponding to a particle diameter

of 0.4 µm, while the response time for aluminum oxide was 20-28 µs, corresponding to a particle diameter of 1.2 µm.

In flows experiencing large electric fields, there is a possibility that the tracer particles may get charged. The potential difference created between two electrodes during formation of a spark causes ionization of the gas around the electrodes, leading to formation of plasma. If this gas is seeded with material, there is a possibility that the tracer particles in the region between the electrodes may acquire some charge due to the same electron bombardment that leads to ionization of the gas. In such cases, it is important to consider the effect of electrohydrodynamics (EHD) on the tracer particles to ensure that these electrical force effects do not hinder the tracer particles from accurately following induced flow. Hamdi and colleagues [38] performed extensive research on determining the best tracer particles to use in EHD flows. The group ran an experiment with different tracer particles seeding a region with corona discharge. It was determined that the particles that would have the least effect on the original current and voltage characteristics of the gas they were seeded in would be those that did not acquire any charge or a negligible amount of charge. Pitot tube measurements along with PIV measurements were used to quantitatively determine which particles followed the flow most exactly. Silica, titanium dioxide, cigarette and incense smoke particles were determined to be the best for EHD flows, with all of these particles following the flow almost exactly and not acquiring any charge. Zouzou et al. noted that for particles larger than 2µm, field charging was dominant while for particles smaller than 0.2 µm, thermal diffusion was more probable [43]. A detailed discussion on how the best tracer particles were determined for the present experiments is included in Appendix C.

Another important factor to consider when selecting tracer particles is the light scattering behavior. In PIV analysis, the intensity of particle images is used to correlate image pairs and determine displacement. Light scattered by particles is directly related to the size and ratio of refractive index of the particles to that of the medium in which they are suspended [39]. When considering smaller particles for flows in air, the refractive index of the tracers becomes important. Silica for example is preferred to titanium dioxide and aluminum oxide due to its high refractive index and hence better light scattering

characteristics. Figure 1-3 shows Mie scattering behavior of particles of different size where the circular contours represent the intensity of scattered light. It shows that larger particles have more even scattering and therefore for a camera placed at 90°, it is clear that very small particles with more back scattered light would be less desirable. In cases where the particles need to be small enough to follow high speed flows and flows with shocks, stronger light sources are required to make up for the lowered scattering from the tracers themselves.

(a)

(b)

(c)
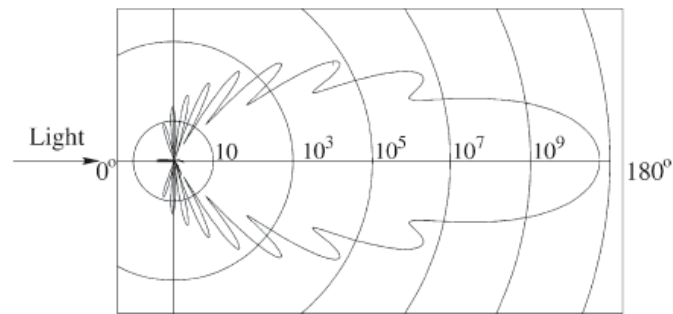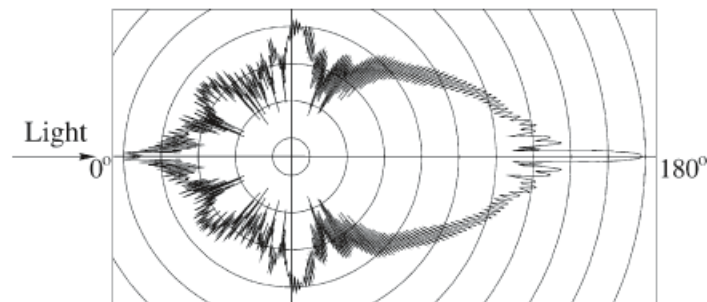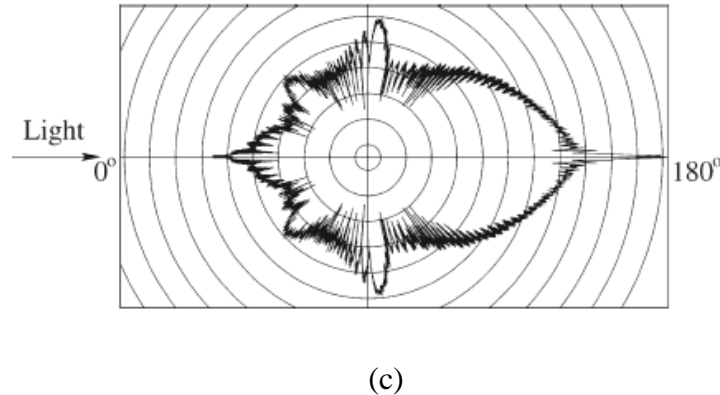
Figure 1-3: Light scattering by (a) 1 μm, (b)10 μm, and (c) 30 μm particles in water [39]

1.5.2   Light Sources and Light Sheet Optics
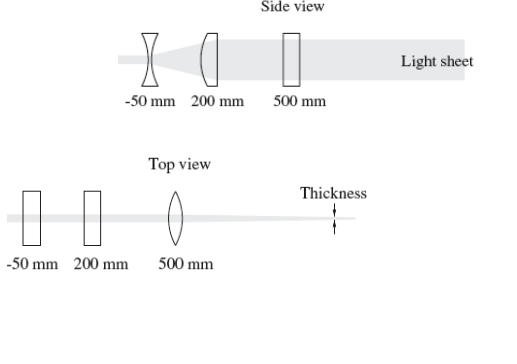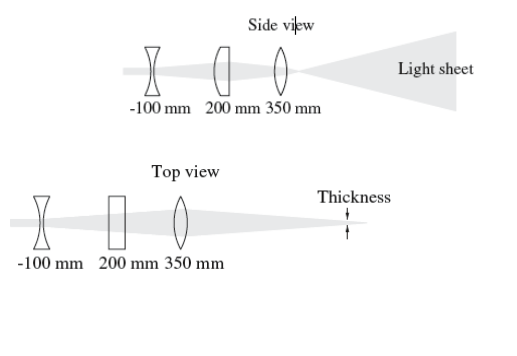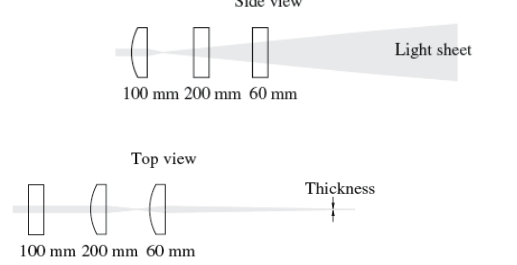
High-powered pulsed light sources are a necessity for PIV. These allow for imaging of small particles that can effectively scatter the large amount of light provided as well as imaging of high fluid velocities. The most common light source used in PIV is a pulsed laser. Laser is an acronym for light amplification by stimulated radiation. In quantum mechanics, energy levels change in steps. The spacing between energy levels gets smaller for energy levels higher above the ground state, with electrons at higher energy levels having more energy than electrons at the lower energy levels. When the energy in the electrons gets high enough, the electron escapes from the atom, leading to ionization. As Albert Einstein proposed, one can stimulate emission such that, if one has an excited atom that is illuminated with photons having the same energy as that between the transition states (higher to lower), the stimulated emission would have the same wavelength and be in phase with the light wave that stimulated it [44]. Most atoms and molecules tend to be at their lowest possible energy level (equilibrium) under "normal" conditions. Because these atoms and molecules always tend to lower energy levels, the population, which is the number of atoms/molecules at each energy level [44], is unevenly distributed, with very few atoms and molecules at higher energy levels. To ensure that stimulated emissions dominate, population inversion is required. This is a condition where there are more atoms in the excited state than in the lower level. This way, it is more likely that photons will stimulate emission rather than be absorbed by those in lower energy levels. In the case of population inversion, "the stimulated emission can produce a cascade of light" [44]. In a laser,

population inversion is achieved by both population of the upper energy levels and depopulation of the lower energy levels [44].

Population inversion can be achieved in 2 main ways: optically (using pulsed light emitted by a powerful lamp or by a laser beam) and electrically (by radio frequency or pulsed current flowing in a conductive medium) [46]. In the case of an Nd:YAG solid-state laser, it is optically excited using a diode pump or a stack of diode pumps. The internal Q-switching (quality switching) of the laser allows for production of high power short duration light pulses which are of higher intensity than continuous wave light. The characteristic quality factor or Q measures internal loss in a laser; the value of Q is inversely related to the amount of loss. A Q-switch changes the mode in the cavity of the laser where the laser light can either be transmitted or absorbed and repetition leads to the generation of a series of small pulses. The short light pulses on the order of 10 ns ensure that the particles imaged in this time are essentially motionless in space, thus avoiding particle streaking.

The light that comes out of the laser is usually too small in diameter to be able to illuminate most regions of interest, thus a laser sheet must be generated. In most cases, cylindrical lenses are used to generate the light sheet so as to expand the beam in one direction (for 2-D PIV) and to focus the light sheet to an appropriate thickness in the third direction. Spherical lenses may also be used and are in general easier to manufacture than cylindrical lenses. Three common systems for generating light sheets are shown in Table 1.1.

Table 1.1: Different types of laser sheets and their characteristics [39]

Side view -50 mm 200 mm 500 mm Light sheet Top view -50 mm 200 mm 500 mm Thickness	• Three cylindrical lenses (diverging lens and two convex lenses) • First lens used to diverge incoming laser beam • Second lens used to generate constant height • Third lens used to focus bean down to a thin waist • Least versatile set-up
Side view -100 mm 200 mm 350 mm Light sheet Top view -100 mm 200 mm 350 mm Thickness	• Two spherical lenses (diverging and converging lenses) and one cylindrical lens (converging lens) • Thickness of light sheet is changed by moving the spherical lenses with respect to each other; light sheet height controlled by cylindrical lens • Light sheet height and thickness cannot be changed independently
Side view 100 mm 200 mm 60 mm Light sheet Top view 100 mm 200 mm 60 mm Thickness	• Three cylindrical lenses, all convex lenses • Light sheet height and thickness can be changed independently • Energy per unit area is very high at critical regions in this set-up and need to be shielded

1.5.3   Imaging and Pulse Timing

PIV measurements require that the laser be pulsed and that the timing between the two pulses can be precisely controlled so the particle displacement can be accurately captured to determine flow velocity. High-speed cameras are also a key feature in most PIV set-ups. CCD (charge coupled device) cameras and CMOS (complementary metal-oxide semiconductor) cameras are the most commonly used cameras in PIV applications. CCD cameras experience longer frame transfer times with analog-to-digital conversion being relatively slow. Interline transfer CCD cameras and CMOS cameras have faster

transfer rates allowing for imaging of very high speed flows with little to no loss of information during the transfer period.

The two most common methods of taking 2-D PIV images are single-frame, double-exposure and double-frame, single-exposure recordings. In the past when cameras had lower frame transfer speeds, the single-frame double exposure approach was used. In this method, both laser pulses would illuminate the same frame and the frame would be evaluated using autocorrelation methods. This method is not the most efficient for PIV as it is difficult to determine the direction of particle motion since it is not known which particles were recorded from the first laser pulse and which ones were recorded from the second. With easier access to high speed cameras, single exposure double-frame recordings (frame straddling) have become more common and a preferred method of taking PIV images. In this approach, double-frame images are taken with the first pulse of the laser illuminating the first frame at a time t_1 and the second laser pulse illuminating the second frame at a time t_2 as shown in Figure 1-4. The difference between the two times is the laser pulse separation (Δt between L1 and L2 in Figure 1-4). The time between the two laser pulses (the difference between the start time of one laser pulse and the start time of the second laser pulse), Δt, is a critical parameter. To determine the appropriate value of dt one needs to consider the displacement of the tracer particles. Following the quarter-rule [39], for a given interrogation window size, the maximum displacement should at least one quarter of the window dimension. For example, the optimum amount of particle shift for PIV in a 32 x 32 interrogation window size is about 8 pixels. Once the scaling between pixels and the distance in meters is determined, and assuming that the approximate velocity of the flow under examination is known, the value of dt can be determined:

$$\Delta t = \frac{\text{displacement}\,(\text{m})}{\text{velocity}\,(\text{m/s})} \tag{1.3}$$
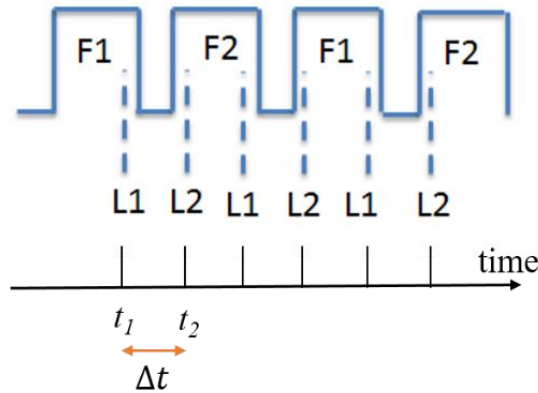
Figure 1-4: Laser pulses illuminating individual frames in a dual frame recording

1.5.4 Analysis

1.5.4.1 Overview of PIV evaluation techniques

The main objective in PIV is to measure the velocity of the flow by first measuring the displacement of particles. When a flow is seeded with particles and imaged between two laser pulses, it is expected that the particles illuminated by the second laser pulse will have been displaced from the particles illuminated by the first laser pulse by a certain distance $d(x,y)$. In order to quantitatively determine this displacement, a significant portion of the same particles from the first illumination would have to be present in the second illumination. In general, the second image consists of the spatial displacement $(d(x,y))$ as well as some additive noise $(n(x,y))$. The noise arises from particles moving out of the image interrogation region and three dimensionality of the flow [48]. Digital PIV (DPIV) methods rely on correlation principles to evaluate displacement between particles in two consecutive images. The general explanation of the correlation principle that follows seeks to provide insight into the main mechanism used in determining this particle displacement.

One of the key properties used to track the particles is the particle intensity. Particles from the first illumination are defined as $I(m,n)$ and particles from the second illumination are defined as $I'(m,n)$ where I is the intensity. To obtain an accurate spatial distribution of the velocity field, the field of view is divided into smaller sections called interrogation windows as shown in Figure 1-5. Particles from each illumination in the interrogation window are compared using various displacement values $d(x,y)$ to

determine the actual distance the particles moved. For a shift or displacement where the particles align, the sum of the product of pixel intensities is the highest, leading to a high correlation value. Each interrogation window thus represents one velocity vector. Note that the cross correlation between two images yields a first order displacement, therefore choosing a small enough interrogation window is critical in determining small scale flow structures [39].
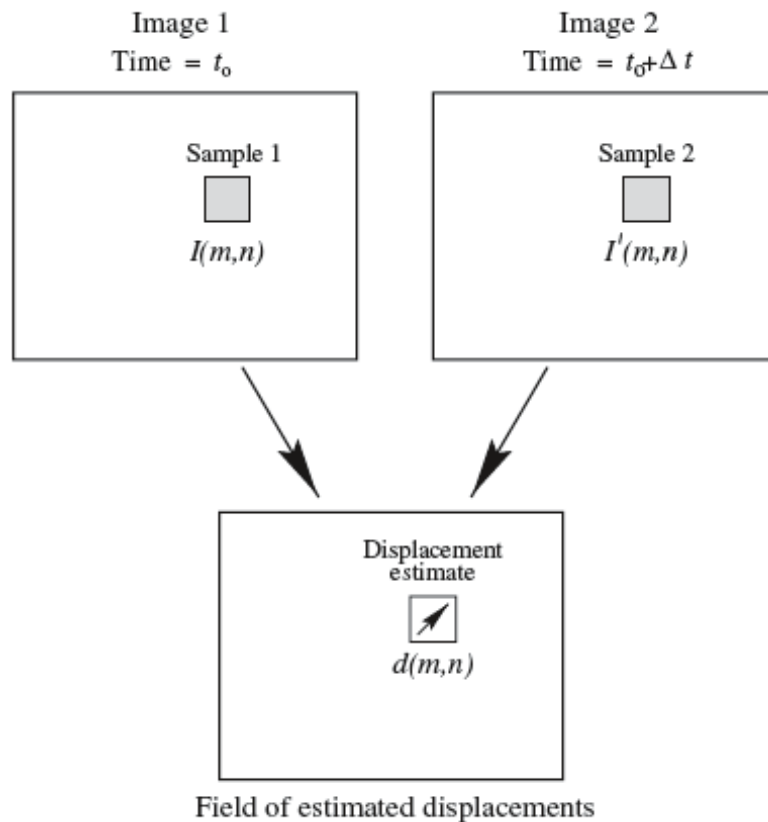
Figure 1-5: Interrogation windows from two images taken a time Δt apart and the corresponding displacement estimate [39]

Auto-correlation and cross-correlation are the two main methods used in PIV analysis [39]. In a double-exposed image, the displaced pattern is superimposed on the original pattern and analyzed using auto-correlation methods. This was a popular method used to analyze PIV images taken as photographs. Covariance, a measure of how much two random variables change together, is used to determine displacement. In this method,

there are three dominant correlation peaks, the central peak is covariance of each particle with itself and two displacement correlation peaks on either side of the central peak, obtained from correlation of the particle images in the first exposure with their corresponding images in the second exposure and vice versa. These peaks do not give information on the directionality of flow, though there are additional methods of determining this [49]. Autocorrelation is less used in present day PIV due its directional ambiguity [49] and the development of high speed cameras has also done away with the need to doubly illuminate a single frame to track tracer particles.

In practice, seeding of test sections in PIV is generally high and individual particle tracking becomes difficult and time consuming [50]. It becomes necessary to use digital methods in PIV to determine these flow fields. In a cross correlation analysis, a cross correlation function is used to determine the best match between images from the two different illuminations. As explained earlier in this section, the function I is traced in I' to determine the best match and products of the overlapping intensities give the correlation value, with the highest correlation value corresponding to the best match of particles for a particular shift. Processing is performed in each interrogation window pair (from frame one and frame two) to determine the vector best describing the flow behavior in the interrogation windows. In present day PIV, images are thousands of pixels by thousands of pixels, requiring numerous interrogation windows and multiple attempts at determining the optimal shift for each interrogation window and therefore an efficient computing technique is required. The correlation theorem states that "the cross correlation of two functions is equivalent to a complex conjugate multiplication of the Fourier transforms". Fast Fourier Transforms (FFTs) thus reduce computation time and are frequently used for PIV analysis. The image signals are converted to FFTs, whose complex conjugate multiplication is determined. An inverse of this is found, which corresponds to the correlation plane.

Additional processing techniques need to be used to account for issues with using FFT to perform cross correlation analysis. Fourier transforms are by definition an integral sum from -∞ to ∞. When analyzing finite images, an assumption that the data is periodic and repeats itself is needed to use FFTs. Windowing removes edge discontinuities by

convolving the original function with another function to smooth the edges. Aliasing, an issue that arises when displacement or more broadly, a signal is greater than half of the interrogation window or sample size, a violation of the Nyquist theorem [39], is an example of one of the issues that arises from an FFT analysis of non-periodic data. To ensure that there is no aliasing, a good interrogation window size and pulse separation must be chosen to ensure a minimum displacement of ¼ of the interrogation window size. Another effect that needs to be considered is weighting of the windows to ensure there are no bias errors. Bias errors also arise due to periodicity of correlation data. As the first interrogation window I is traced or shifted over I' as discussed above, there is less data correlated to each other, for example, at the edge of the correlation plane, only half of the tracer particles contribute to the information gathered. If a weighting factor is not put in place, then the measurements will be biased to lower values, since after the initial shift, all that follow contain less data. The measurements obtained are averages of the actual velocity field in the interrogation region, therefore larger displacements are not well accounted for, leading to a bias toward lower velocities.

1.5.4.2 DPIV techniques used in PRANA

PRANA is a graphical user interphase written in MATLAB programming language that began its development at Virginia Polytechnic Institute and State University. It is used to perform digital PIV analysis. It employs Fourier based cross correlation methods to analyze images as discussed previously. It contains a wide range of processing options that suit the user's needs to output the desired velocity field.

To ensure that particle images from both illuminations have the same background intensity, some pre-processing techniques such as background subtraction need to be applied. This eliminates effects of non-uniform illumination along the laser sheet due to reflections or non-uniform light intensities between the two laser pulses. Different filters can also be applied on the images if the level of intensity of particles contributing to the analysis is known. This then ensures that only contributing particles within specified intensity ranges are processed.

Multi-pass interrogation is often used to analyze images. In this processing method a first pass is executed with an interrogation window size that obeys the ¼ rule. This first

pass is used to determine the mean displacement of particles. The results of this pass must then be validated using post processing techniques discussed below as it will be used by subsequent passes to more accurately show displacement. The second pass is then displaced by the average values determined in the previous pass. This improves signal to noise ratio and accounts for more matches in particles [39]. A convergence criterion such as a minimum correlation value for all passes can be specified to improve accuracy, but to ensure a finite computation time in the absence of convergence a maximum number of passes can be specified as well. Generally, this value is set to 3 [39].

The grid resolution of the interrogation regions can also be changed from one pass to another. The second pass could have a smaller interrogation region as can the following passes, so that both small and large displacements are accounted for (increased dynamic spatial range). The final pass usually should have no outlier removal or smoothing as part of its post processing, as this should be done in the preceding passes. When using multi-grid methods, velocity interpolation between the different grid sizes in the different passes needs to be performed. Bicubic interpolation is a popular method.

In many cases, flow is non-uniform and it becomes necessary to obtain accurate displacement of flows with high shear, rotation and other sources of large velocity gradients. Image deformation is a technique that can be used to better capture such displacements. Similar to offsetting the interrogation windows based on average displacement, the entire PIV images can be shifted as well. A windowed-sinc filter with Blackman window is used to interpolate the deformed imaged back onto the rectilinear grid [57]. In this method, if the initial shift between two windows is known or can be estimated, this shift estimation can be used to deform the interrogation windows used to analyze the two images (taken at t and Δt) to better capture large velocity gradients. This deformation needs to be mapped back onto the rectilinear grid. This is done by convolving the sinc function shown in equation (1.4) with the signal being analyzed creates a low pass filter such that frequencies below f_c are passed [39]. This is especially useful when dealing with large velocity gradients as it smooths spurious fluctuations. The Blackman filter smooths the spiked edges of the filtered function that arises due to truncation of the sinc function [51].

$$h(i) = \sin\frac{2\pi i f_c}{i\pi} \tag{1.4}$$

The robust phase correlation (RPC) technique is used to correlate image pairs. This technique increases the signal to noise ratio and has been found to "reduce bias errors as well as peak locking in rotational flows with high shear" [52]. Phase correlation eliminates the magnitude component of the correlation and retains the phase-only components. These result in more prominent correlation peaks, allowing for more accurate determination of particle displacement.

Avoiding peak locking effects, especially in high shear flows is important. Peak locking arises when there is bias in displacement to integer pixel values [52]. Inaccuracies in sub-pixel displacement estimations are the main cause for peak locking [39]. Sub-pixel accuracy is obtained by using a three point Gaussian peak fit that is weighted. The Gaussian peak fit equation is shown in equation (1.5). Since the peak fit assigns values closer to the origin higher weights than those further out, the correlation values determined need to be divided by the corresponding weight factors before applying the Gaussian fit [39].

$$f(x) = C\exp[\frac{-(x_0 - x)^2}{k}]$$
$$x_0 = i + \frac{\ln R_{(i-1,j)} - \ln R_{(i+1,j)}}{2\ln R_{(i-1,j)} - 4\ln R_{(i,j)} + 2\ln R_{(i+1,j)}} \tag{1.5}$$

1.5.4.3   Post processing and Vorticity approximations

Where C is the maximum amplitude of the correlation peak, k describes the spread of the peak on the x axis of the correlation plane. x_0, the center of the correlation peak and is defined by scanning the correlation plane R to find the maximum correlation value R(i,j) and the surrounding correlation values.

The previous section discusses the smoothing and validation of all but the last pass when analyzing images. By observation, it is easy to see spurious vectors in certain regions of the flow. The elimination of this incorrect data is part of post processing. Calculating vorticity is important for fluid dynamics and is usually an approximation of the evaluated displacement vectors. This is also discussed in this section.

Imposing a mean or median filter is common when validating results, both these methods are universal outlier detection methods. Mean displacement of vectors in an interrogation region can be used to look for outliers. If a velocity value is outside the mean value by a specified factor, this velocity value is eliminated. Similarly, velocity values outside of a specified range of the median of the velocity vectors are deleted. The median filter is preferred to the mean in higher speed flows or flows with large velocity gradients. The median filter looks for the most frequent velocity in a specified region while the mean averages the velocity, thus in regions experiencing extremely high and low velocities, with the high velocities being the "bad" vectors, the mean does not necessarily reflect a true representation of the velocity in the region. A minimum correlation threshold can also be used to identify incorrect correlation values and hence serve as a validation technique. Correlation is a good representation of desired velocities, however is not always an accurate representation of valid displacements [39]. Gaussian smoothing of the velocity field is needed in initial passes when using any of these filters that remove vectors that do not meet the set criteria. The smoothing provides continuity between the eliminated velocity values.

Differentiation schemes must be used to calculate the vorticity of the flow field. Accurate determination of vorticity is dependent on the differentiation scheme used on the velocity vectors obtained from the PIV analysis. Central differencing schemes have been found to have the least uncertainty of the standard differentiation schemes including forward difference, backward difference, central difference, Richardson extrapolation and the least squared method [39]. Using the circulation method has been found to have even lower uncertainty than any of the standard differencing schemes as it uses more data points to calculate the vorticity [39] as will be seen below. Vorticity can be defined in terms of circulation by applying Stokes theorem as:

$$\overline{(\omega_z)}_{i,j} = \frac{1}{A}\Gamma_{i,j} = \frac{1}{A}\oint_{1(X,Y)}(U,V)\times dl \tag{1.6}$$

Where $\overline{(\omega_z)}_{i,j}$ is the average vorticity in an enclosed area, A. $\Gamma_{i,j}$ is the circulation at point (i,j). U and V represent the velocities in the X and Y directions respectively, and l

represents the enclosed area, defined by X and Y coordinates. If one considers the vorticity enclosed in a rectangle as shown in Figure 1-6, the average vorticity is found by dividing the local circulation at (i,j) by the enclosed area.
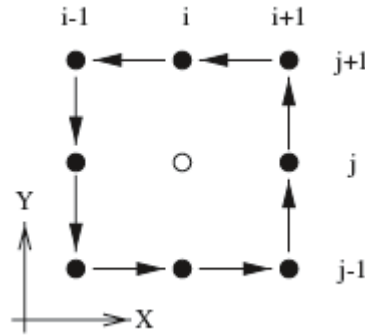
Figure 1-6: Vorticity estimation contour at (i,j) by finding circulation [39]

Therefore, while vorticity is the curl of the velocity vector, and circulation in an enclosed space is the line integral of velocity in that space, both can be related as in equation (1.6). The circulation in the region shown in Figure 1-6 can be estimated using the 8 points shown and can be used to find vorticity using equations (1.7) and (1.8). These equations are similar to integration using the trapezoidal rule.

$$(\omega_Z)_{i,j} \triangleq A\frac{\Gamma_{i,j}}{4\Delta X \Delta Y} \tag{1.7}$$

$$\Gamma_{i,j} = \frac{1}{2}\Delta X(U_{i-1,j-1}+2U_{i,j-1}+U_{i+1,j-1})+\frac{1}{2}\Delta Y(V_{i+1,j-1}+2V_{i+1,j}+V_{i+1,j+1})$$
$$-\frac{1}{2}\Delta X(U_{i+1,j+1}+2U_{i,j+1}+U_{i-1,j+1})-\frac{1}{2}\Delta Y(V_{i-1,j+1}+2V_{i-1,j}+V_{i-1,j-1}) \tag{1.8}$$

Where, ΔX and ΔY represent the grid spacing between interrogation windows. Note that the center of the X,Y plane corresponds with the center of the rectangular contour in Figure 1-6.

CHAPTER 2. EXPERIMENTAL SET-UP

2.1   Experimental Set-Up

2.1.1   Experiment Overview

A schematic overview and a photograph of the experimental set-up are is shown in Figure 2-1 and Figure 2-2, respectively. The main components shown include a Q-switched Nd:YAG laser, the test section with the electrodes, and a Photron SA-Z camera which is placed perpendicular to the test section. The laser sheet is generated using 3 cylindrical lenses to create a collimated sheet that is converged in one direction to facilitate 2D PIV. There is a periscope installed at the beginning of the sheet to lower the height of the sheet off the table. The electrodes are enclosed in a pressure tight steel chamber with optical access. The specifications of the critical experiment components are given in Table 2.1 and are described in detail in the following sections.
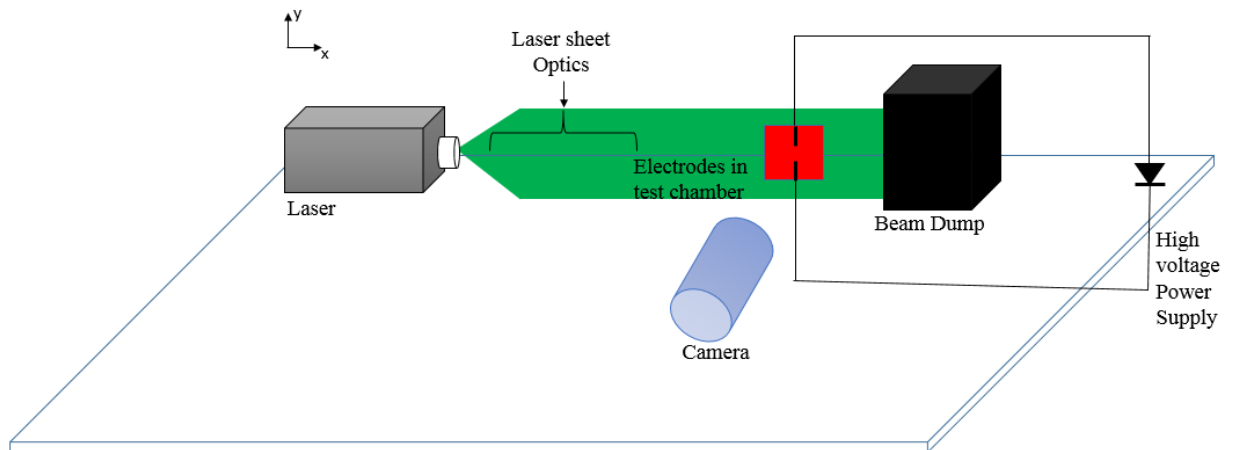
Figure 2-1: Schematic overview of the experimental set-up.
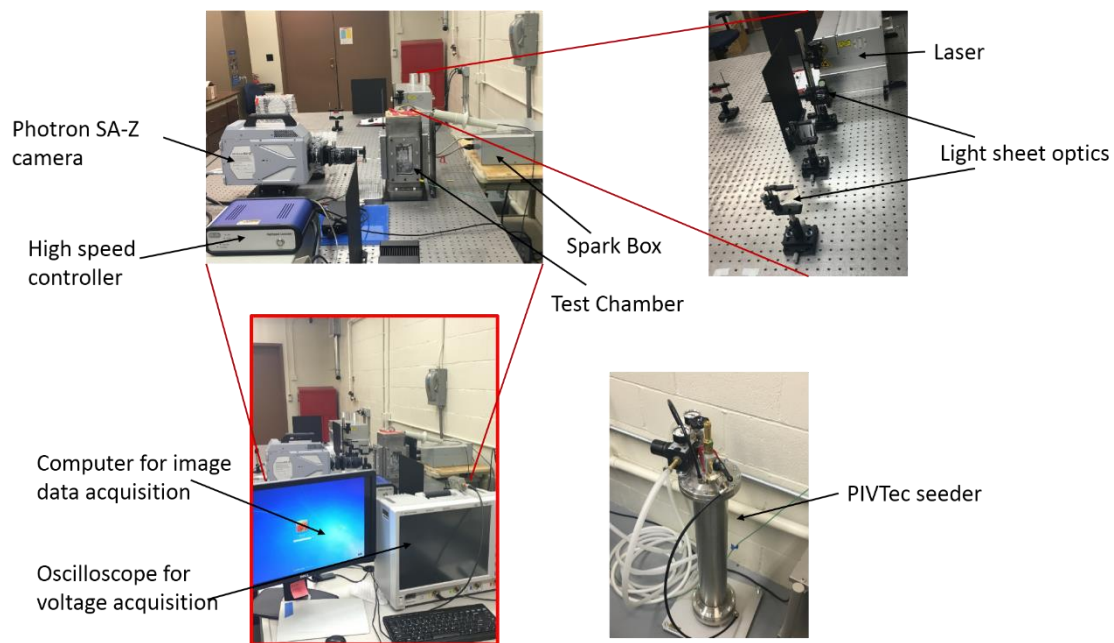
Figure 2-2: Photograph showing the experimental set-up.

Table 2.1: Experiment system components and specifications

Component	Description	Specifications/Properties
Laser	• Nd:YAG (532nm; 10ns pulse duration)	• Operated at 10 kHz (3.6 mJ pulse energy)
Camera + Lens	• Photron Fastcam SA-Z • 105mm Nikon Nikorr	• Operated at 20,000 fps (10,000 fps - dual frame mode) • Resolution: 1024 x 1024 pixels; FOV: 40 x 40 mm
Circuit	• Spark discharge system used to generate plasma	• Breakdown voltage up to 45 kV (0.5 J) • Discharge time ~ 1 μs • Spark gap 10mm; 5mm
Software	• Davis 8.2.3 (LaVision) • PRANA	• Davis software used to synchronize system components and save images • PRANA software used to process images for PIV
Seeding	• Al$_2$O$_3$ particles – Martinswerk MR70	• Size : 0.2 - 5 μm [54] • Solid density: 3960 Kg/m^3 • Bulk density: 900 Kg/m^3 • Stokes number: 0.002 (at 18m/s assuming 0.3 μm particle diameter)
Seeder	• PIVSolid 8S	• Fluidized bed of solid particles • Can operate at pressures up to 8 bar • De-agglomerates particles

2.1.2 Particle Image Velocimetry

This experiment uses a diode-pumped, solid-state level four INNOSLAB laser purchased from EdgeWave. The solid lasing or gain medium that is pumped with a laser diode is Neodym (Nd3+ ions) doped YAG (yttrium-aluminum-garnet) crystals. The system includes a laser head consisting of two independently triggerable oscillators, a power supply, a water chiller and an external frequency doubling and beam combining box. The Nd:YAG laser is Q-switched, allowing for generation of high-energy short pulses, and frequency doubled using KD*P crystals. The resulting light emitted by the laser has a wavelength of 532 nm (green light) and the beams shape is square (5 mm x 5 mm) as a result of the slabs of YAG used to generate the beams. Each frequency doubled beam is capable of a pulse repetition rate from a single shot to 10 kHz with a maximum average

power of 27 W. The pulse energy when the laser is optimized for 10 kHz is 3.6 mJ. The pulse duration is 10 ns. The two beams are adjusted such that they overlap in this experiment. The standard operating procedure used for the laser is provided in Appendix B.

The laser sheet optics consist of 3 cylindrical laser lenses as shown in Figure 2-3; the specifications of the optics used and the resulting sheet geometry is given in Table 2.2. The first lens is a plano-concave lens with focal length -50.8 mm used to expand the 5 mm x 5 mm square beam produced by the laser in both the x and y direction. The expanded laser sheet is then collimated using a 300 mm focal length plano-convex lens with the height of the laser sheet depending on the distance between the plano-concave lens and the first plano-convex lens. The final plano-convex lens, focal length 700mm, converges the beam to a thin waist, allowing for 2-D PIV imaging.

(a)

(b)
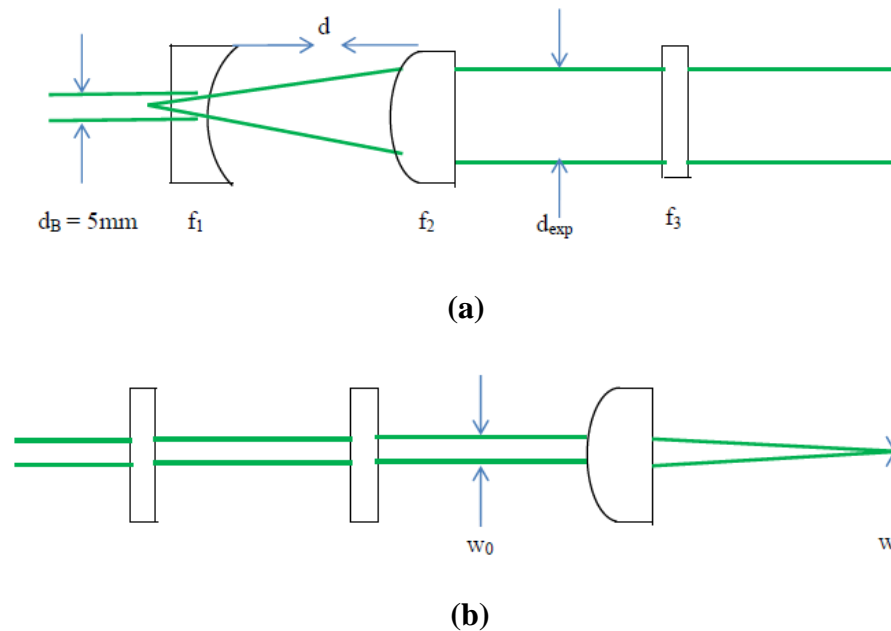
Figure 2-3: (a) Side view of laser sheet (b) Top view of laser sheet

Table 2.2: Specifications of laser sheet optics and resulting sheet geometry.

Labels	Definition	Measurement (mm)
d_B	Laser beam diameter	5
f_1	Focal length (Concave lens) - 25.4 x 25.4	-50.8
f_2	Focal length (Convex lens) - 50.8 x 50.8	300
f_3	Focal length (Convex lens) - 50.8 x 50.8	700
d_{exp}	Laser sheet height	28
w_0	Initial beam wait	5
w	Final beam waist	< 1

There is a periscope installed at the beginning of the sheet to lower the height of the sheet so it is aligned with the electrodes. The distance between the first two lenses, *d,* was chosen to be 250 mm based on the height requirement of the laser sheet and by applying the theory of reversibility to align the focus of the diverging lens to that of the converging lens. The maximum possible height of the laser sheet is 2 inches based on the dimensions of the two plano-convex lenses. An additional constraint was placed on the laser sheet height by the maximum required gap between the electrodes, 20 mm. This desired spark gap size determined the minimum height of the laser sheet. The height of the laser sheet was determined theoretically as shown in Figure 2-4 to confirm that the optics arrangement would produce the desired height. The laser sheet height was estimated to be 1.35 inches, which was reasonably close to the actual sheet height (1.1 inches) obtained with the completed set-up.
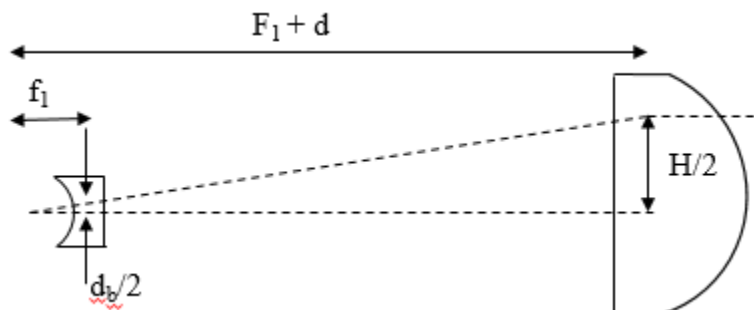
Figure 2-4: Geometry used to approximate height of the laser sheet

A Photron FASTCAM SA-Z high-speed camera is used to record the PIV images with a 105 mm Nikon lens used for focusing. The FASTCAM SA-Z CMOS camera is capable of imaging at up to 20,000 fps at the full resolution of 1024 x 1024 pixels and up to 2.1 million fps at reduced resolution. The monochrome camera captures 12-bit uncompressed data with a 1 µs shutter speed. A LaVision high speed controller (HSCv2) is used to synchronize and trigger the laser, the camera and the spark discharge. Figure 2-5 shows the timing diagram for an experiment with the camera operating at 10,000 fps in dual frame mode, each laser head operating at 10 kHz with a pulse separation of 20 µs, and the spark synchronized with the laser to trigger with the first pair of laser pulses.
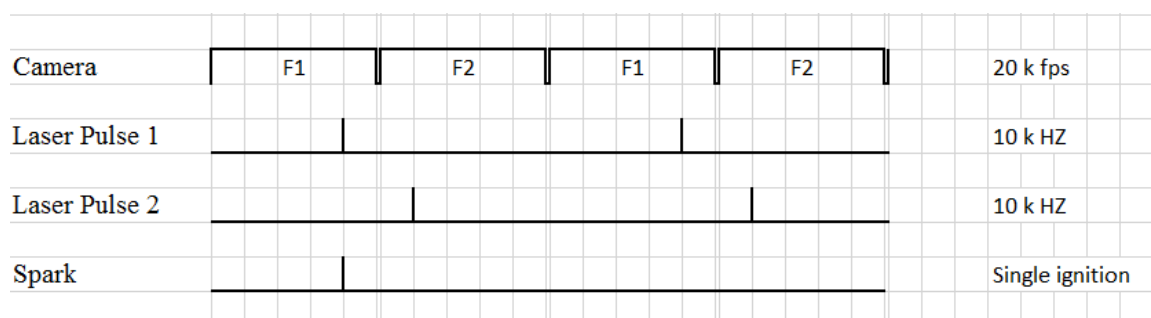
Figure 2-5: Experiment timing diagram

The tracer particles used to seed the flow are alumina (MR-70) particles obtained from Martinswerk. The manufacturer stated diameter of these particles is 0.3 µm, and their density is 3960 kg/m^3. It should be noted, however, that though the exact particle size was not determined by this research group, previous researchers that have used the same

particles to perform PIV analysis have reported actual particle diameters ranging from 0.2 μm to 5 μm with the average particle diameter being closer to 0.8 μm [52]. The agglomerates of the alumina particles were closer to 50 μm in diameter, however it is assumed for this experiment that once the particles were de-agglomerated by the seeder they did nor re-agglomerate in the test section.

2.1.3   Plasma Generation

Figure 2-6 shows the circuit used to generate the spark plasma. The circuit is comprised of three sub-circuits that are described in detail in [55]. The first circuit transforms 120 VAC supplied by a wall outlet to 300 VDC which is then used in the remaining two sub-circuits. The second sub-circuit charges a capacitor to 300 VDC when armed with a 5 VDC signal. An external TTL signal is used to trigger the third sub-circuit which causes the capacitor to discharge through an EG&G high voltage pulse transformer that is rated up to 45 kV (0.5 J). This voltage is sufficient for breakdown in electrode gaps up to 20 mm and larger [55].
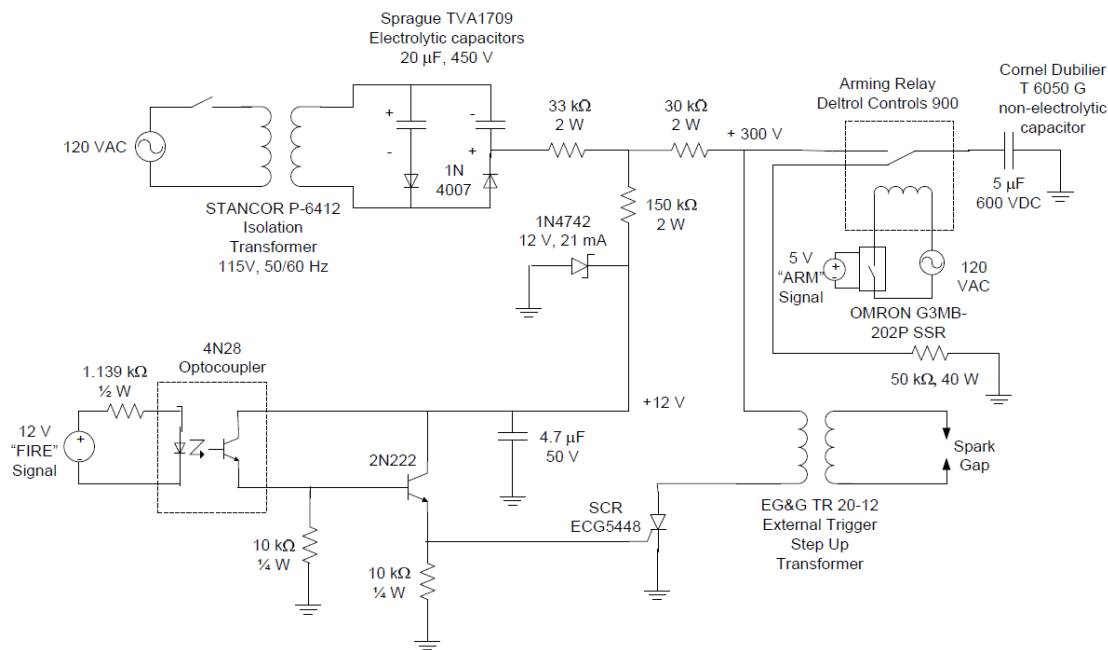
Figure 2-6: Diagram of the discharge circuit used to generate the spark.

A steel, pressure-tight rectangular chamber, shown in Figure 2-7, is used to enclose the test section holding the electrodes. The chamber walls are 1 inch thick, as the chamber was designed to ultimately be used with high pressures. Fused quartz windows are held in place with O-ring sealed flanges on the chamber. The electrode wires and seeder have holes on the top flange for access into the chamber. There is also a manually controlled vent to expel excess tracer particles from the chamber. The electrodes are mounted on the bottom flange of the test chamber. The diameter of the electrodes used is 2.8 mm (0.112"). The geometry of electrodes used in the experimental set- up is shown in Figure 2-8 and the spark gap is varied between 8mm, 5mm and 2mm.
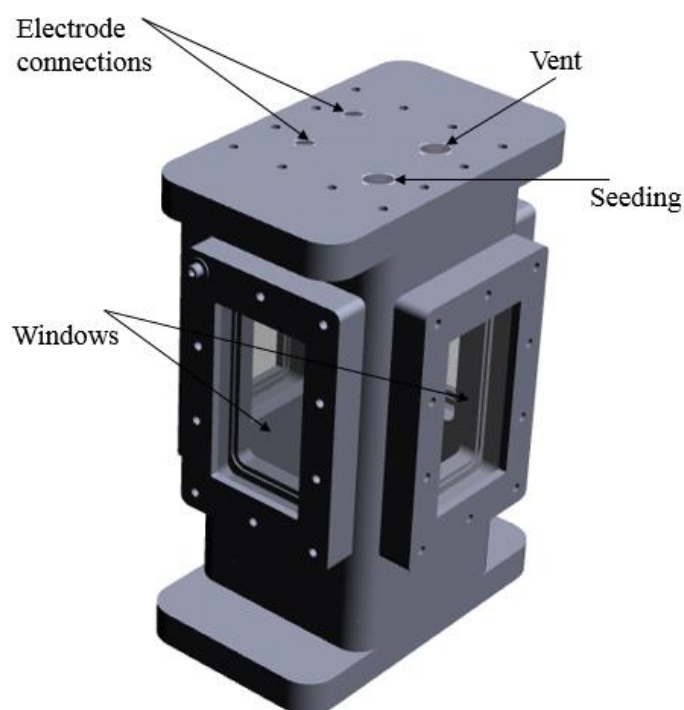
Figure 2-7: CATIA model of test chamber
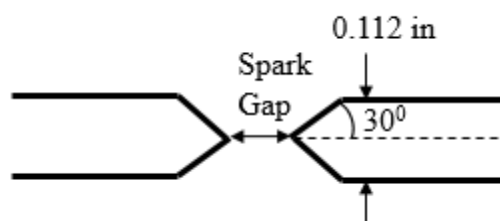
Figure 2-8: Geometry of electrodes with cone-shaped tips [35]

2.2 Experimental Procedure

The first step of the procedure was to calibrate the camera to set the length scales. A dot paper consisting of 1 mm dots spaced at 5mm was used as a 2-D calibration target. An image of the calibration target was taken using the DaVis software where the dot spacing and dot size were defined. Before taking the image the number of cameras in the set-up as well as the coordinate system and origin must be specified. A validation of the implementation of the PIV measurement technique using the set-up was performed using a known flow. The exit flow from a sonic nozzle was used. A discussion of the validation is presented in Appendix Appendix A.

CHAPTER 3. PIV IMAGE PROCESSING PROCEDURES

Once images were obtained at the desired camera frame rate, laser pulse, and pulse separation, the next step was to process the results. The images were processed within the PRANA software described in Section 1.5.4.2. Three different processing techniques were utilized:

(1) Use of a geometric mask to specify the region of interest where the flow is to be observed

(2) Determination of the optimal interrogation window resolution

(3) Vector post-processing to filter the final results to show flow trends

3.1 Pre-processing of Images

An appropriate geometric mask for the images is used to define the region of interest for vector processing. The maximum field of view of the camera lens, approximately 30 mm x 30 mm, encompassed a larger area than the region of interest (ROI). The primary masking technique used was the enabling of portions of the image showing the desired flow field during processing. The ROI was thus 6 mm by 9 mm for the sonic nozzle and varied based on the size of the electrode gap for the spark. Figure 3-1 shows an example of the mask used to include certain regions of the image for the 10 mm electrode gap case.

Note that the seeding density in the region of interest is of great importance. Numerous researchers [50], [56] have found that increasing the seeding density improves the correlation and thus decreases the occurrence of spurious vectors. They suggest that a

 minimum of 10 particles per interrogation region must be maintained to ensure good correlation between image pairs.
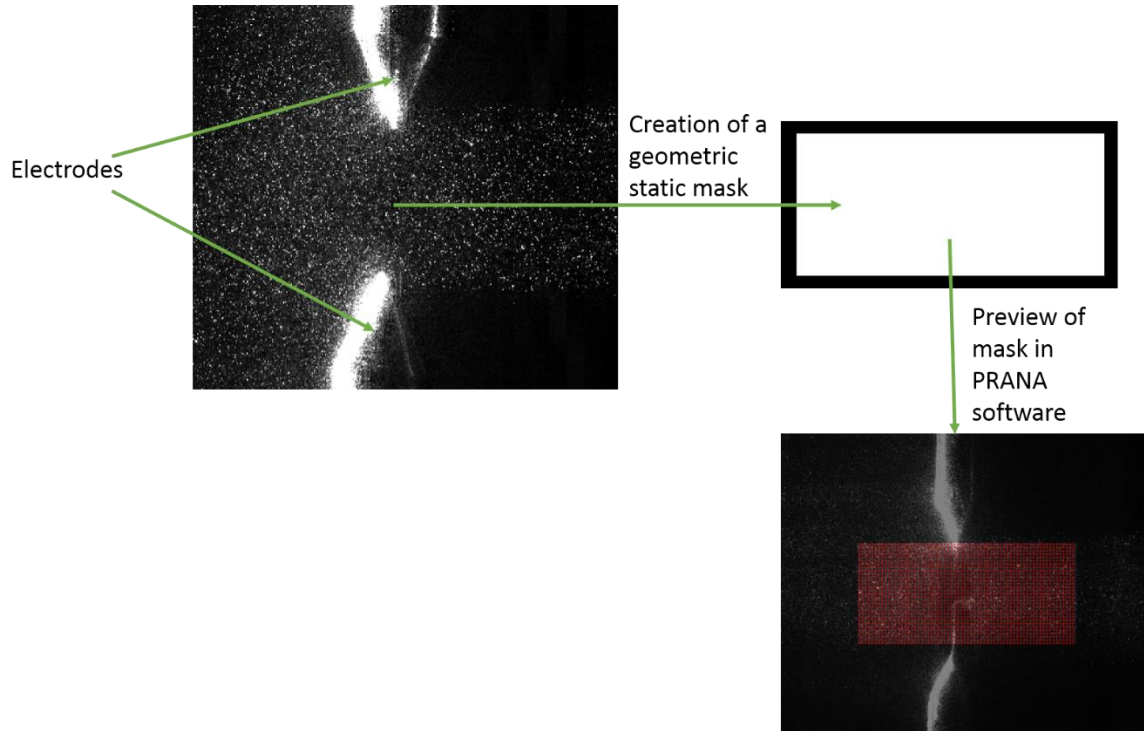
Figure 3-1: Image masking used to eliminate regions outside the ROI.

3.2   Determination of Optimal Interrogation Window Region

A 5mm electrode gap is used to assess interrogation window resolutions of 96 x 96 pixels, 64 x 64 pixels and 48 x 48 pixels. The different grid resolutions tested are 16 x 16 pixel, 8 x 8 pixel, 4 x 4 pixel and 2 x 2 pixel grid resolutions.

Before processing of the region of interest, windowing is performed on the image. Generally, interrogation window sizes are rectangular grids. When cross correlating two interrogation windows in two images, issues associated with aliasing may arise at the edges of the interrogation window. In order to mitigate effects of aliasing, a tapered Gaussian windowing function is incorporated [57]. This allows for a smooth transition to the edges of the window. In PRANA, the window resolution is usually 50% of the window size. A differentiation between the two is made in Figure 3-2. The following discussion will be based on size of the interrogation window resolution, hereon referred simply as window resolution.
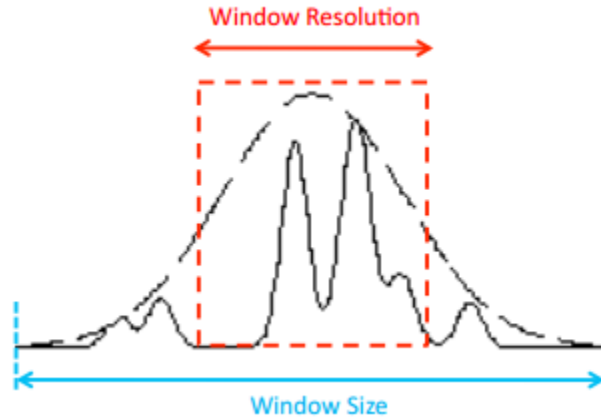
Figure 3-2: Interrogation window resolution and window size [57]

To determine the appropriate window resolution, an analysis was first performed to determine the smallest resolution that could be used to cross-correlate the two double frame images and produce meaningful vectors. Previous work [35] had shown that at times greater than 100 µs after the spark breakdown the expected velocity would be less than 10 m/s, which would correspond to a displacement of approximately 5-7 pixels. This velocity measure was used to validate results obtained from this analysis, such that the velocity obtained was within the same order of magnitude.

Results of the cross correlation analysis can depend strongly on the interrogation window resolution. For each window resolution, an averaged velocity vector is used to represent the flow in that window. For large window resolutions containing numerous small flow structures, a single velocity vector will be unable to properly resolve the complexity of the flow. For extremely small window resolutions, however, tracking particle displacement becomes more difficult as it is harder to maintain the same particles in two consecutive frames for cross-correlation. Figure 3-3 shows a set of images taken at 10 kHz with 10 µs pulse separation whose corresponding velocity vectors are analyzed with different window resolutions. These images represent flow induced approximately 1000 µs after the spark breakdown. Note that expected displacements at this time should be less than 2 pixels/frame.
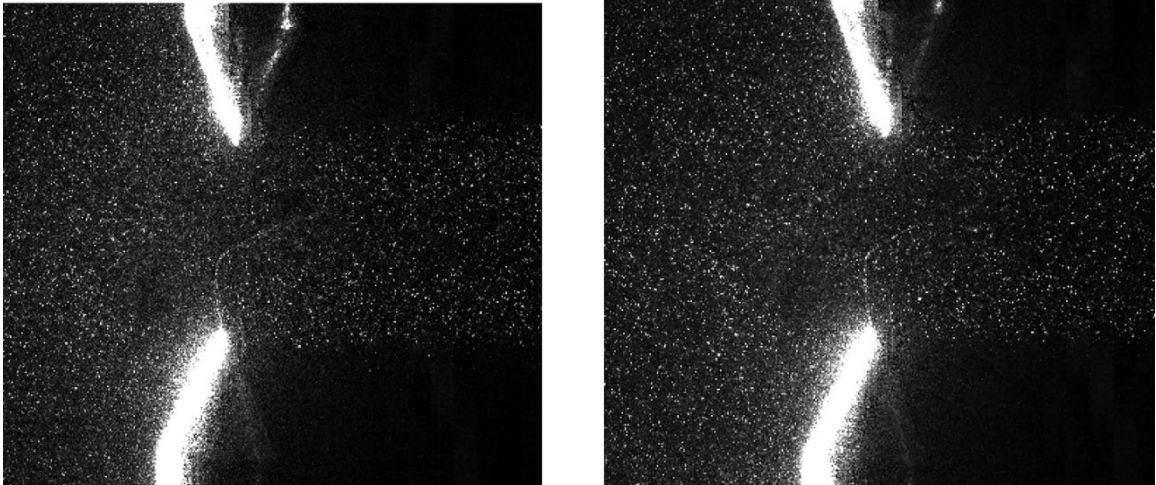
Figure 3-3: Particle images (double frame) at approximately 1000 µs after spark ignition.

In order to assess the appropriateness of the interrogatin window resolution and maintain the same number of vectors within an interrogation region, the grid resolution was maintained for each test case. For example, for a 96 x 96 pixel window resolution, the grid resolution was maintained at 8 x 8 pixels resulting in 91.67% overlap, while for a 48 x 48 window resolution, mainitaning the same grid resolution resulted in an overlap of 83.33%. The relationship between grid resolution and overlap is shown in Figure 3-4 by using a 32 x 32 pixel interrogation window and a 50% overlap. These values were chosen for simplicity. To determine a grid independent-solution, i.e. a solution that gives similar velocity measurements across all interrogation window resolutions, it was necessary to assess different grid sizes as well. Thus, once the optimal interrogation window resolution was determined, it was tested with grid resolutions of 2 x 2 pixe,4 x 4 pixel,8 x 8 pixel and 16 x 16 pixel. The entire field of view was about 400 x 300 pixels for the 5 mm gap.
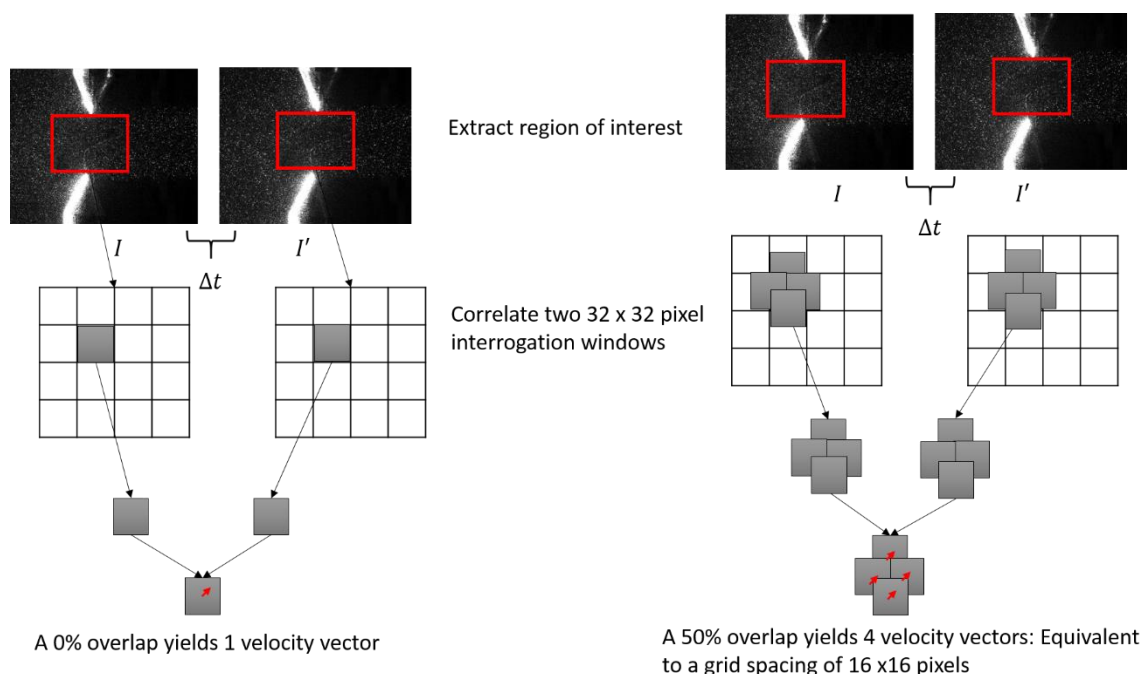
Figure 3-4: Relationship between overlap and grid resolution defined in terms of PIV cross correlation analysis

Figure 3-5 shows the velocity values obtained. The first main difference to notice between the 96 x 96 pixel window resolution results and the other two window resolutions is that the velocities resolved by the 96 x 96 pixel interrogation window resolution are biased to lower values than those in the other two, lower window resolutions. The 64 x 64 pixel and 48 x 48 pixel interrogation window resolutions resolve smaller flow structures better than the 96 x 96 pixel resolution. The green circles in the 64 x 64 pixel window resolution show the small vortical structures not captured by the 96 x 96 pixel window. The maximum resolved velocity in the 64 x 64 pixel window resolution is greater than that of the larger resolution window, at 1.2 pixels per frame compared to 0.7 pixels per frame for the 96 x 96 pixel case. The results using the 48 x 48 pixel window resolution are very similar to those using the 64 x 64 window resolution; the main difference is that the smaller window resolution results in a slightly higher maximum velocity of 1.3 pixel per frame. The smaller flow structures around the spark gap and close to the surface of the electrodes are more visible in the 48 x 48 pixel interrogation window resolution, similar to the 64 x 64 pixel window resolution as shown in Figure 3-5 (c). An attempt to reduce the

interrogation window size further to 32 x 32 pixels results in numerous spurious velocity values that hinder proper resolution of the flow field. Though the 48 x 48 pixel window resolution would be more desirable than the 64 x 64 pixel size for determination of smaller flow structures, it was found that when analyzing all the 20 datasets for the 100 different time steps, a 64 x 64 pixel interrogation window produced velocity flow fields with less outliers than the 48 x 48 pixel interrogation window. For this reason, the individual datasets were analyzed with a 64 x 64 pixel interrogation window resolution, while the ensemble correlation datasets, discussed later, which had no significant outliers in the smaller interrogation region, were analyzed with a 48 x 48 pixel interrogation region.

(a)

(b)

(c)
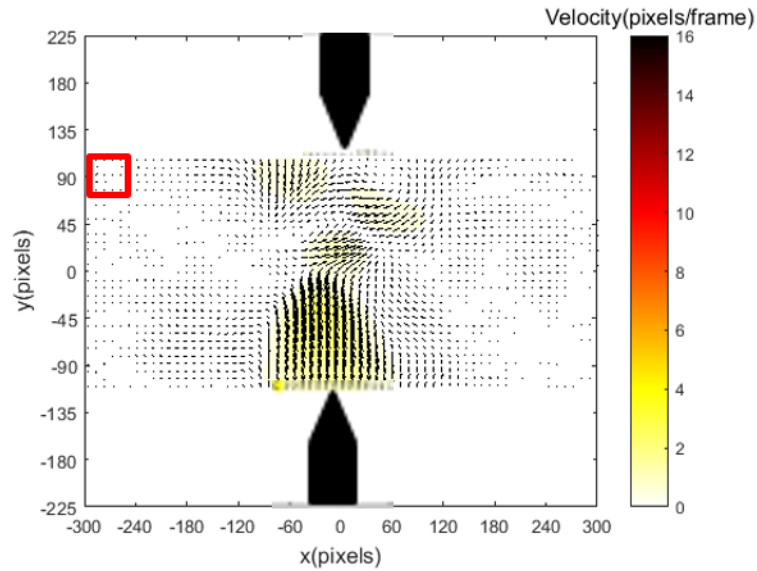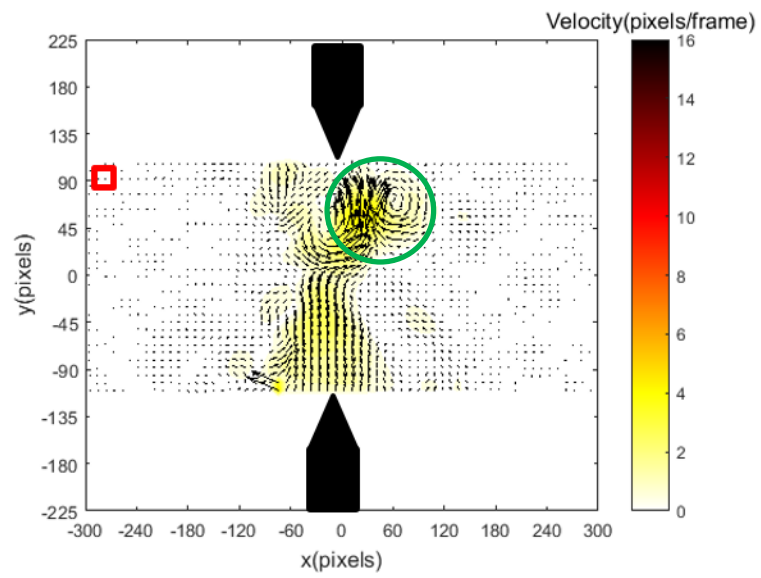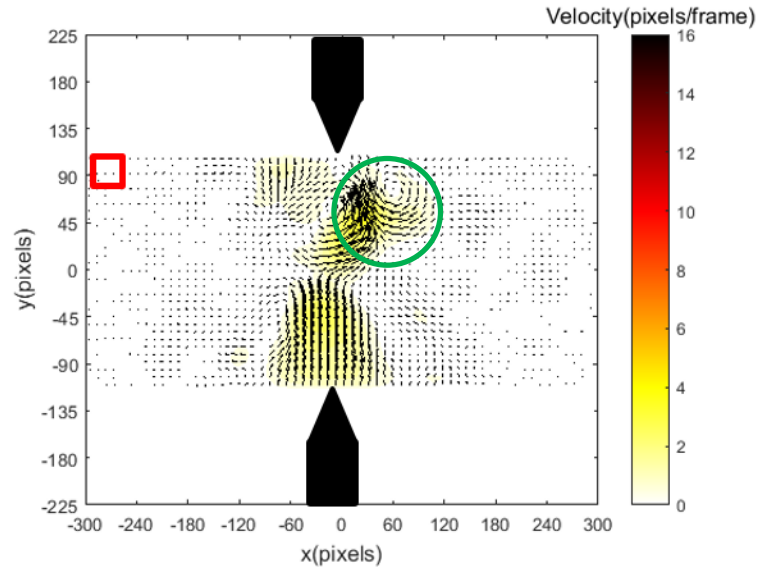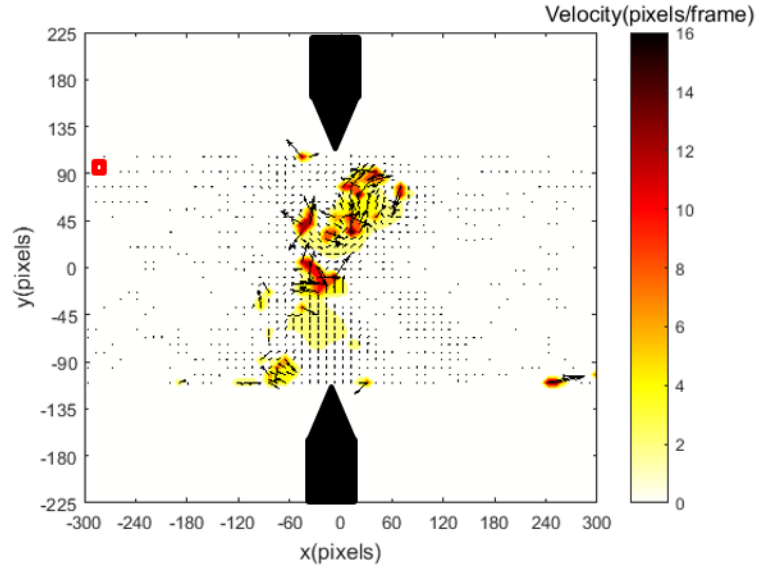
(d)

Figure 3-5: Flow field obtained using a multi-pass (a) 96 x 96 pixel interrogation window resolution, (b) 64 x 64 pixel interrogation window resolution (c) 48 x 48 pixel interrogation window resolution, and (d) 32 x 32 pixel interrogation window resolution with grid resolution of 8 x 8 pixels, approximately 1000 µs after spark ignition (laser frequency 10kHz and pulse separation 10 µs).

It is important to also determine the optimal grid resolution or overlap between images during processing. Though it is important to ensure that the velocity is independent of grid resolution it is also important that the overlap between images, which is directly related to the grid resolution, is within reason. It should be ensured that the overlap is not so large that the signal from particle intensities in both frames are not sharing too much information. The overlap value depends on the velocity gradients in the flow as well as the seeding density, most authors choose overlaps between 50% and 75% [56]. For this flow, it was necessary to determine the best overlap or grid resolution that would resolve the flow. It is also important to ensure that computation time is not too lengthy as smaller grid resolution means more vector locations are processed. Examples using two extremes of the grid resolutions, 2 x 2 pixels and 16 x 16 pixels, are shown in Figure 3-6(a) and (d), respectively. In the former, the overlap between images is over 93%. The large degree of overlap means there is a repetition of information in the interrogation regions, leading to possibly inaccurate or repetitive velocity measurements, in this case however, comparing

the 2 X 2 pixel grid resolution to the 4 x 4 pixel and 8 x 8 pixel grid resolutions does not show significant differences in flow structure . In the 16 x 16 pixel resolution case (Figure 3-6(d)), on the other hand, there are too few vectors describing the flow, making it difficult to observe small flow strucures and details of the flow field. Resolutions of 4 x 4 and 8 x 8 pixels both represent a happy medium between the more extreme grid resolutions. The 8 x 8 pixel resolution is chosen due to decreased computation time and similar velocity results to that of the 4 x 4 pixel grid resolution, while still showing the significant small flow structures.

(a)

(b)

(c)

(d)
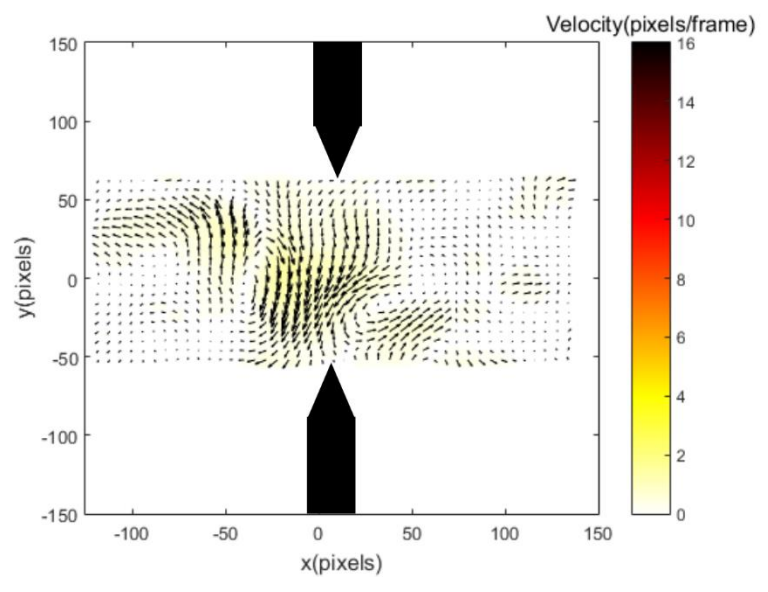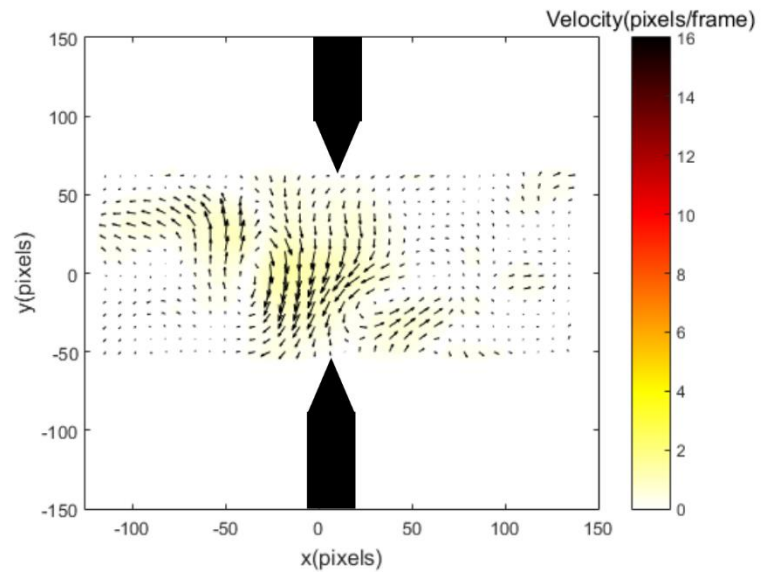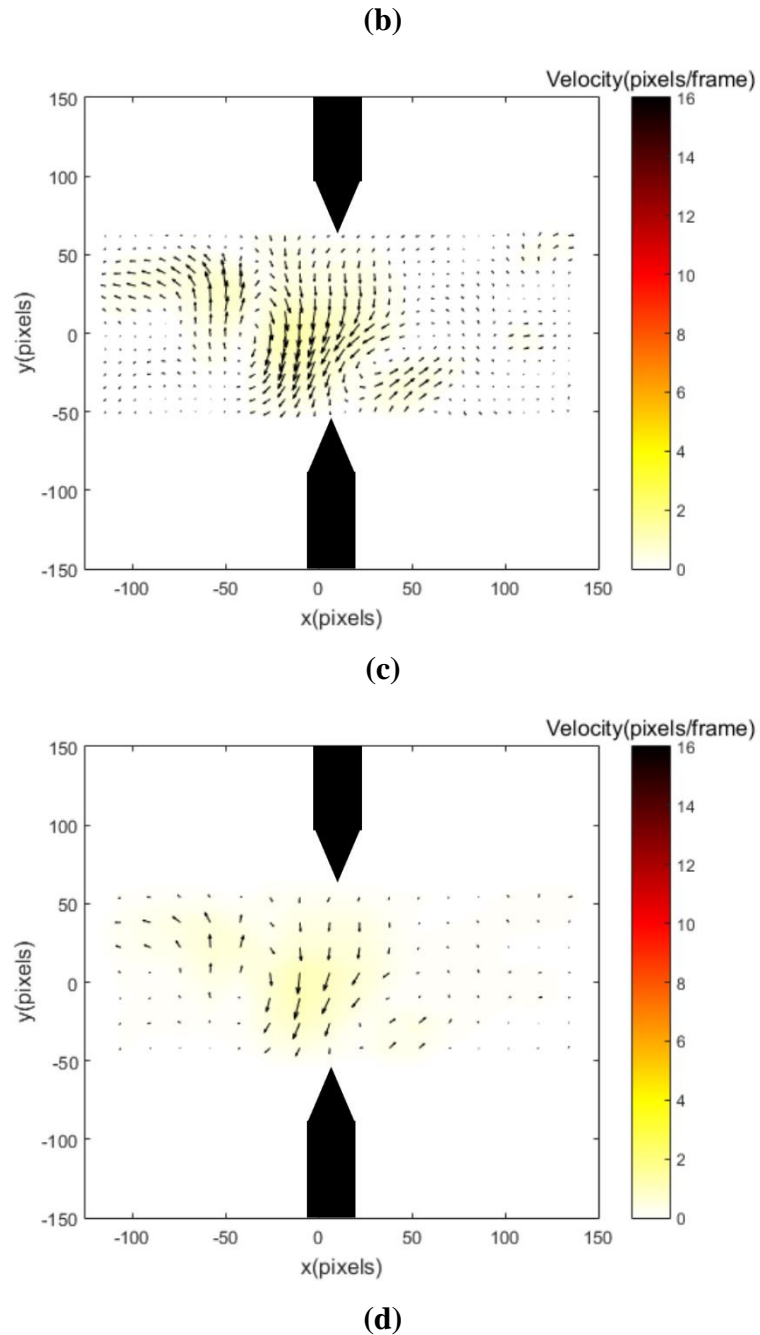
Figure 3-6: Flow field obtained using multi-pass 48 x 48 pixel interrogation window with grid resolution of (a)2 x2 pixels, (b) 4 x 4 pixels, (c) 8 x 8 pixels, and (d) 16 x 16 pixels approximately 1000 μs after spark ignition (laser frequency 10kHz and pulse separation 10 μs).

In some instances it is necessary to capture both large and small displacements in the same flow. For example, in cases where there are small scale flow structures in a high

speed flow regime, it would be difficult to correctly analyze the flow using either just a large interrogation window to capture particle displacements in the high speed regime or a small interrogation window to capture the small scale flow structures. It then becomes necessary to analyze the flow in multigrid-multi-pass mode. This means that the first few passes would have larger interrogation window resolutions to capture the large particle displacements, and the final passes use smaller windows to capture the smaller displacements. Multi-pass processing, has been found to give better results than single pass processing [39], [58]. In multi-pass with deform processing, the program runs through the first and second frames to determine the mean particle displacement. Based on the results of the first pass, the window is shifted and deformed depending on the mean particle displacement determined from the previous pass. This ensures that even large displacements of the particles are captured and displayed with reasonable confidence.

This process is illustrated in Figure 3-7 for the spark-induced flow in a 5 mm gap and 8 mm gap. Results so far have shown that in some cases using a constant interrogation window size of 48 x 48 pixels compared to a multigrid method of 64 x 64 pixels at initial passes and then a 48 x 48 pixel interrogation window size at later passes is capable of resolving the flow field just as well as can be seen in Figure 3-7(a) and (b). However, in other instances, such as the one shown in (c) and (d) the latter method shows better resolution of the flow field. This is observed from the resolution of the flow field in the center of the electrode gap. In the constant window size, a deformed flow structure in the center region closer to the top electrode is observed while in the decreasing window case, this structure is fully resolved. This is a subject of ongoing research, and therefore for the current work a constant window size of 48 x 48 pixels was used to reduce computation time.
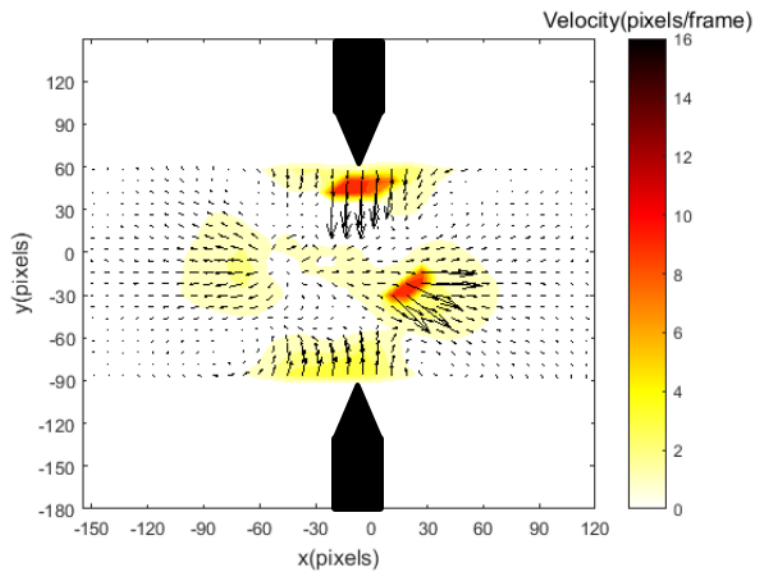
(a)
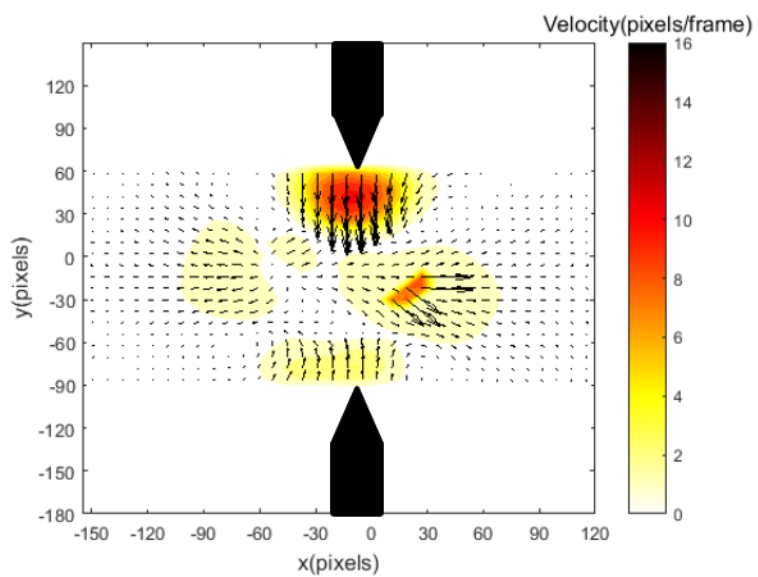
(b)
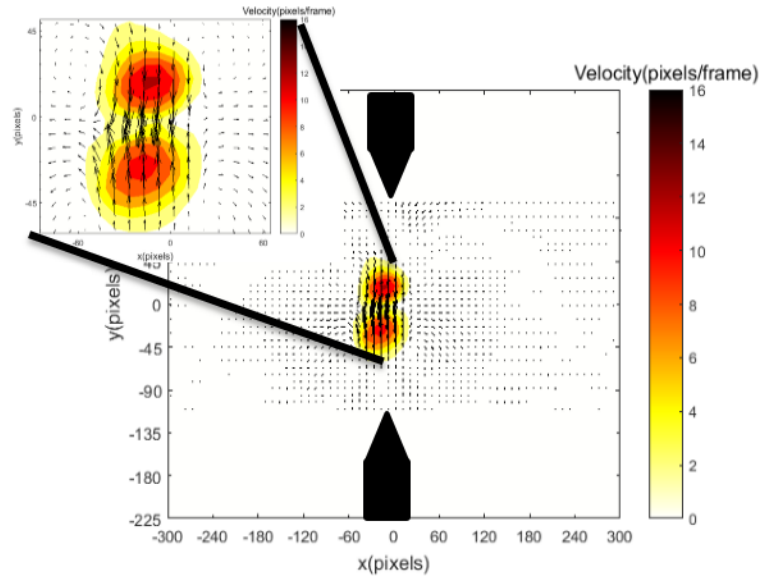
(c)
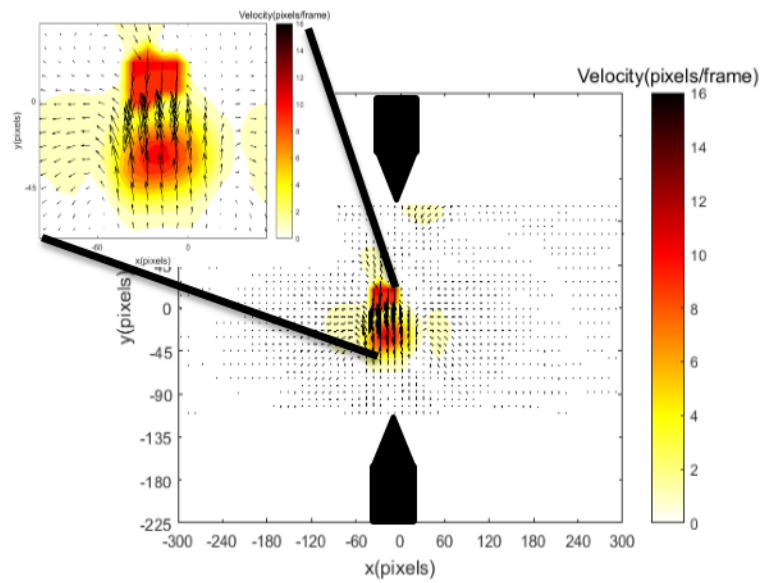
(d)

Figure 3-7: Flow field obtained using multi-pass analysis with (a) decreasing window resolution (64 x 64 pixel to 48 x 48 pixel), (b) constant window resolution of 48 x 48 pixel, for a 5mm electrode gap (laser frequency 10kHz, pulse separation 30μs) (c) decreasing window resolution (64 x 64 pixel to 48 x 48 pixel) and (d) constant window resolution of 48 x 48 pixel, for an 8mm electrode gap (laser frequency 10kHz, pulse separation 20μs) approximately 200 μs after spark ignition

The final correlation process used to determine the instantaneous flow field vectors involves a post processed, 64 x 64 pixel multi-pass constant resolution interrogation window, with deform. Ensemble correlation processing is performed using a 48 x 48 pixel multi-pass constant resolution interrogation window, with deform. The deform process ensures that regions of high shear in the flow are captured and analyzed without bias. The final grid resolution was set to 8 x 8 pixels, resulting in a window overlap of 83.33% for the 48 x 48 pixel window and 87.5% for the 64 x 64 pixel window.

3.3   Vector post processing

The velocity field obtained from all passes but for the last pass were validated using post processing techniques.   One of the post processing methods involved a median universal outlier detection method, where vectors a set number of mean absolute deviations from the mean are considered outliers. In this work, the method is used to consider all vectors within a 3 x 3 pixel region of the velocity flow field and remove velocity vectors that were 3 standard deviations higher than the median of the 3 x 3 pixel region. Smoothing was also applied to the initial passes. A Gaussian filer weight of 2 was applied to ensure there was no distortion of the velocity field between deformations and to eliminate high frequency noise [57]. Thus, this smoothing was applied to each vector field by taking the mean velocity value of the neighboring grid points (within 2 grid points).

Given that 20 datasets were taken of each time interval of data, it is possible to determine the average flow field by phase averaging the datasets. Ensemble correlation sums up the correlation peaks obtained from each of the 20 datasets to obtain a more prominent correlation peak that serves for all of the datasets. This method has been found to improve flow measurements in Micro-PIV or in uniform flows such as pipe flows, where it is expected that the flow field does not change significantly with time [59], [60]. For this particular experiment, the phase averaging and ensemble correlation are used under the assumption that the flow field at each instant of time for the different experiments should be very similar. This theory will be tested and assessed in the results and discussion section of this thesis.

3.4   Summary of processing steps used in PRANA

The processing performed in PRANA can be summarized by the flowchart shown in Figure 3-8. Once a static mask is used to define the region of interest, the evaluation method needs to be determined. If instantaneous data is required, the multigrid – multipass method with deform is chosen. If an average velocity field is desired, the ensemble with deform method is chosen. The next step is to choose the number of passes, followed by which the grid set-up needs to be defined for each pass. For constant interrogation window resolution, the window resolution and grid size remain the same. The correlation options are then chosen, with the robust phase correlation being the best choice for this flow field. A three point Gaussian estimator is chosen to approximate sub-pixel peak location. For each pass, the velocity interpolation method is set to bicubic, and the deformed image interpolation is set to a sinc with blackman filter. The convergence criteria is set to 0.05. The convergence criteria is the normalized difference between velocity values between consecutive iterations. If the convergence criteria is not met, and the maximum number of iterations has not been exceeded, the next iteration deforms the image further, back-interpolates the image onto the rectilinear grid, and interpolates the velocity field, until the minimum criteria are met. This pass is then post processed using a median filter and smoothing. The information from the first pass is used to analyze the second (last) pass, set at one iteration with no post processing. The final output can then be displayed.
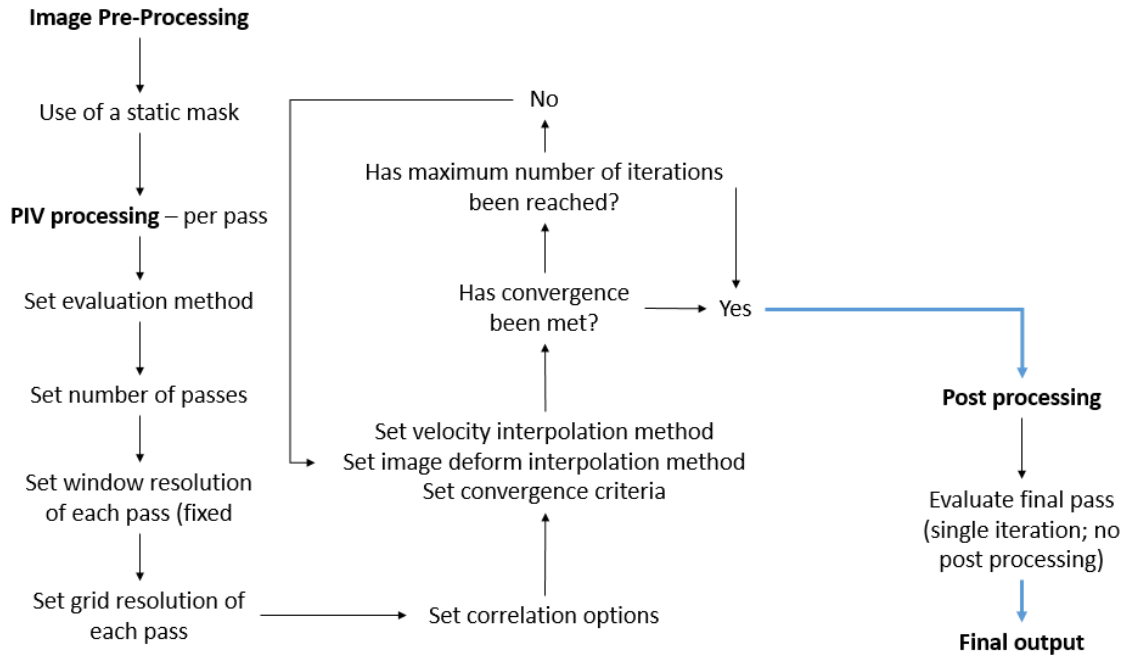
Figure 3-8: Processing steps taken in PRANA to analyze image pairs

3.5   Determination of Pulse Separation for Spark Measurements

Before datasets could be recorded for use with the analysis techniques described in the previous section, the appropriate laser pulse separation had to be determined. Because the exact flow velocity induced by the spark is not known a priori, the flows were analyzed in different phases to determine the optimal laser pulse separation, Δt. The laser sheet was positioned such that the thinnest point of the sheet plane was in the center of the electrode gap. A Δt of 10µs was used first and the maximum pixel displacement was observed to be approximately 3 pixels in a 64 x 64 pixel interrogation window for a 5 mm spark gap. Referring back to the ¼ rule established by previous PIV researchers [39],[48], the displacement of 2 pixels was much less than this suggested maximum. Increasing the pulse separation between the two laser pulses would help get the displacement value closer to 1/4th of the interrogation window resolution, which would be close to 16 pixels. The maximum displacement with an increase in pulse separation to 30 µs is shown in Figure 3-9(b). For all the different datasets this maximum displacement value ranged from 10-14 pixels and was thus determined to be a close enough approximation to the ¼ rule. A similar

procedure was used to determine the optimal pulse separation for the two other electrode gap sizes tested, 2 mm and 8 mm. The pulse separations used are shown in Table 3.1.

(a) **(b)**
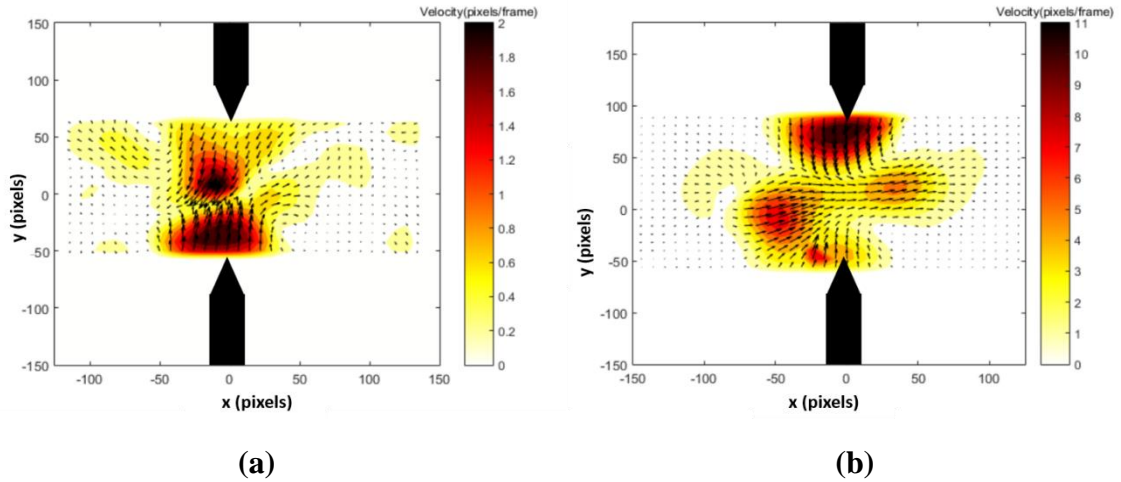
Figure 3-9: Velocity obtained using pulse separations of (a) 10 µs and (b) 30 µs with an interrogation window resolution of 64 x 64 pixels for a 5 mm spark gap

Table 3.1: Pulse separations used for the different spark gaps lengths

Spark Gap Length	Pulse Separation
2 mm	40 µs
5 mm	30 µs
8 mm	20 µs

CHAPTER 4. RESULTS AND DISCUSSION

The experiments are conducted under quiescent conditions at standard room temperature and pressure using cone shaped electrodes with sharp tips. The flow structures induced by the spark plasma are analyzed spatially and temporally for three different electrode gaps: 8, 5, and 2 mm. The difference in flow structures between the electrode configurations is examined and the velocity and vorticity fields are obtained using the PIV system and analysis described in the previous chapters. The results demonstrate the large amount of information that can be obtained about the plasma-induced flow field as well as the limitations of the current PIV system.

The nature of the flow induced by the spark is extremely complex. This thesis attempts shed light on the small structures of the flow field as well as the larger structures dominating the flow. The PIV results discussed in this section were obtained in dual frame mode at 10 kHz laser pulse frequency and pulse separations of 20 μs for the 8 mm gap, 30 μs for the 5 mm gap and 40 μs for the 2 mm gap.

Based on previous work on flow induced by spark plasmas [31],[35], the general flow trends expected are:

- A blast wave is initiated by the expansion of the spark plasma channel, pushing the flow out of the center of the spark gap
- The complex pressure gradients caused by the shockwave induces a complex flow field that evolves over time.
- Vorticity is observed in the region of the spark gap, close to the surface of the electrodes as well as in the center of the gap as hot gas moves outward toward the surrounding region of the spark gap. Possible sources of the vorticity are baroclinic torque in the initial stages of flow development and viscosity and mixing of cold and hot gas in the later stages of the flow

- The magnitude of velocity and vorticity decreases with time [35].

The spark channel expansion is accompanied by a shockwave. Measuring the velocities within the first microseconds of the flow is essential when trying to understand the initial effect the shockwave has on the flow. Electrical measurements taken during the spark discharge show that there is a sharp rise in the voltage within the first 5 μs. The current and energy deposited is also at its maximum during this time as was found in previous research [35]. Schlieren visualization of the shockwave and electrical measurements of the spark during this time would provide insight on the nature and duration of the shock wave. In the current set-up, the spark is triggered to fire with the first laser pulse. The next pair of images are taken 100μs after this trigger event. In these images, a clear plasma channel is seen as shown in Figure 4-1. As is expected, an accurate analysis of the vector field using PIV correlation techniques in the region of the plasma channel is hindered due to the glow of the plasma channel. Therefore, measuring anything in the first few microseconds after the breakdown, when the plasma is very hot and emitting light, is extremely difficult.
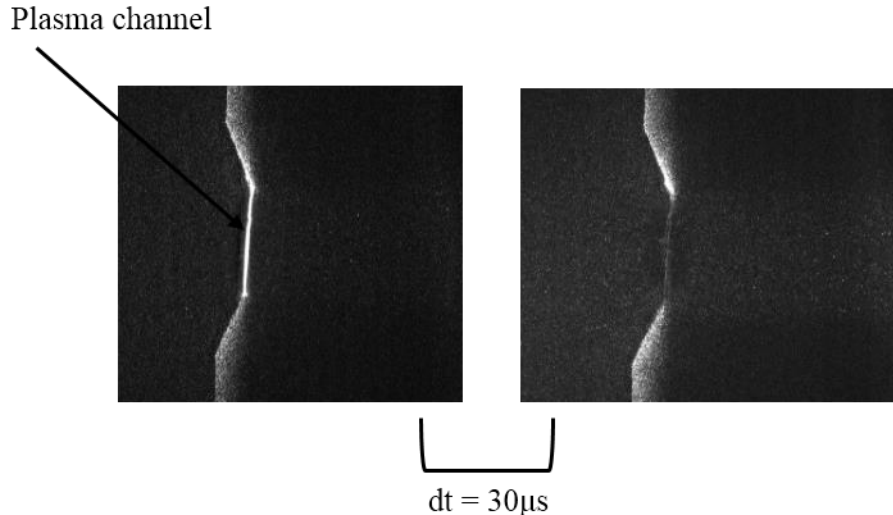
Figure 4-1: Plasma channel observed in 5 mm electrode gap approximately 100 μs after the spark breakdown (pulse separation of 30 μs).

PIV analysis was performed on the images in Figure 4-1 and the resulting ensemble correlated velocity field approximately 100 μs after the spark breakdown is shown in

Figure 4-2. In an ensemble correlation the correlation peaks from instantaneous image pairs is summed to get a correlation peak that is more prominent. This is discussed further in the next section. It is unclear whether the tracer particles in this region are recognized, and whether the velocity fields shown capture the particle movement between frames. There is a concentration of velocity in the center as is expected from the deposition of energy in this region by the spark, and there is some initial outward motion, however, the effect of the glow on flow analysis is still unclear. The instantaneous velocities have a wide range compared to the ensemble correlated image shown. In many cases the instantaneous velocity was as high 50 m/s.

For the reasons discussed above, a PIV analysis at such a short time after the spark is not possible with the current set-up; schlieren visualization and other optical methods will be explored in future work. Therefore, the PIV analysis focuses on the flow starting approximately 200 μs after the spark discharge.
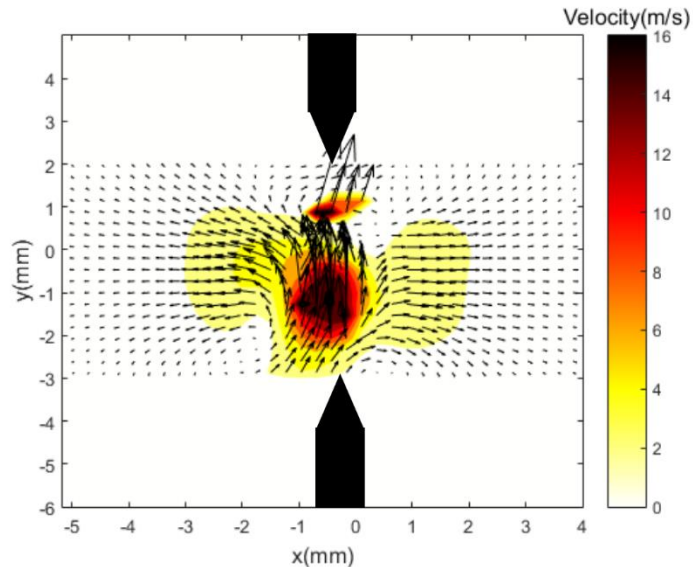
Figure 4-2: Ensemble correlated velocity approximately 100 μs after the spark for a 5 mm electrode gap

4.1   Test Parameters

Once the electrodes are placed as accurately as possible in the thinnest region of the laser sheet and the vessel is sealed, the test section is seeded with smoke particles. The seeding is introduced in small quantities until about 10 particles or slightly more are

observed in the chosen interrogation window of the camera image. The test parameters used in the experiments are given in Table 4.1. The laser was optimized for a frequency of 10 kHz and three different time intervals between pulses. The next section presents an analysis to determine the best method to average the flow field generated for each time interval using 20 experiments performed for each electrode gap configuration. Three different techniques are used. The induced velocity is time-dependent and is observed to decay over prolonged periods. The temporal analysis of the flow field is presented for each electrode gap from about 200 μs to 10 ms after the spark breakdown. A total of 20 datasets were taken for each of the test cases below. This was done to determine the repeatability of the experiment as well as to obtain insight into the different averaging techniques.

Table 4.1: Experimental test parameters and PIV system settings.

Spark Gap (mm)	Laser Frequency (Hz)	dt (μs)	Camera Frame Rate (fps)
8	10,000	20	20,000
5	10,000	30	20,000
2	10,000	40	20,000

The pixel per frame displacements that were seen in the experimental analysis section are converted to m/s in the results section to give a better physical understanding of the flow phenomena. The calibration yielded 30 pixels per 1 mm. Thus for each of the pulse separations, 1 pixel/frame displacement was equivalent to 1.65 m/s, 1.1 m/s and 0.824 m/s for the 20 μs, 30 μs and 40 μs pulse separations, respectively.

4.2   Spatial Distribution of the Flow Field

A spatial analysis of the flow is performed in 5 regions around the electrodes. For the 8 mm gap the analysis regions are:

- Region 1 (C1) corresponds to -3 mm $< x <$ 2 mm & $0 < y <$ 3.75 mm
- Region 2 (C2) corresponds to -3 mm $< x <$ 2 mm & -3.75 mm $< y <$ 0
- Region 3 (R1) corresponds to 2 mm $< x <$ 10 mm & $0 < y <$ -3.75 mm
- Region 4 (R2) corresponds to 2 mm $< x <$ 10 mm & -3.75 mm $< y <$ 0
- Region 5 (L1) corresponds to -10 mm $< x <$ 3 mm & $0 < y <$ 3.75 mm

- Region 6 (L2) corresponds to -10 mm $< x <$ 3 mm & -3.75 mm $< y <$ 0

For the 5 mm gap the analysis regions are:

- Region 1 (C1) corresponds to -1.5 mm $< x <$ 1 mm & -0.5 mm $< y <$ 2 mm
- Region 2 (C2) corresponds to -1.5 mm $< x <$ 1 mm & -0.5 mm $< y <$ -3 mm
- Region 3 (R1) corresponds to 1 mm $< x <$ 4 mm & -0.5 mm $< y <$ 2 mm
- Region 4 (R2) corresponds to 1 mm $< x <$ 4 mm & -0.5 mm $< y <$ -3 mm
- Region 5 (L1) corresponds to -1.5 mm $< x <$ -5 mm & -0.5 mm $< y <$ 2 mm
- Region 6 (L2) corresponds to -1.5 mm $< x <$ -5 mm & -0.5 mm $< y <$ -3 mm

For the 2 mm gap the analysis regions are:

- Region 1 (C1) corresponds to -1.3 mm $< x <$ 1.3 mm & 0 $< y <$ 1 mm
- Region 2 (C2) corresponds to -1.3 mm $< x <$ 1.3 mm & 0 mm $< y <$ -1.2 mm
- Region 3 (R1) corresponds to 1.3 mm $< x <$ 5 mm & 0 $< y <$ 1 mm
- Region 4 (R2) corresponds to -1.3 mm $< x <$ 5 mm & 0 mm $< y <$ -1.2 mm
- Region 5 (L1) corresponds to 1.3 mm $< x <$ 5 mm & 0 $< y <$ 1 mm
- Region 6 (L2) corresponds to -1.3 mm $< x <$ 5 mm & 0 mm $< y <$ -1.2 mm

These regions are shown in Figure 4-3(a) and (b) for the 5 mm gap. The centerline of the analysis region is also shown, and is aligned with the centerline of the electrodes.
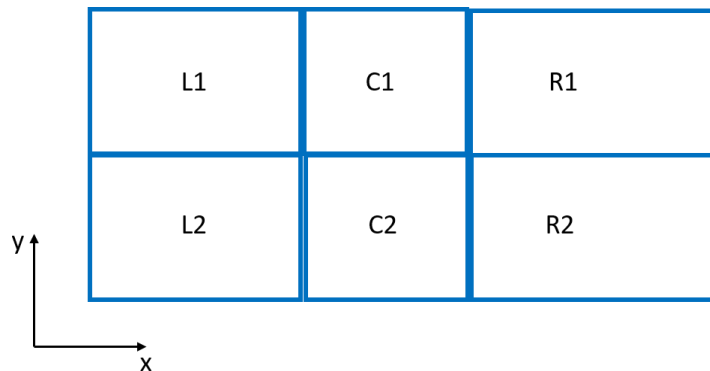
(a)
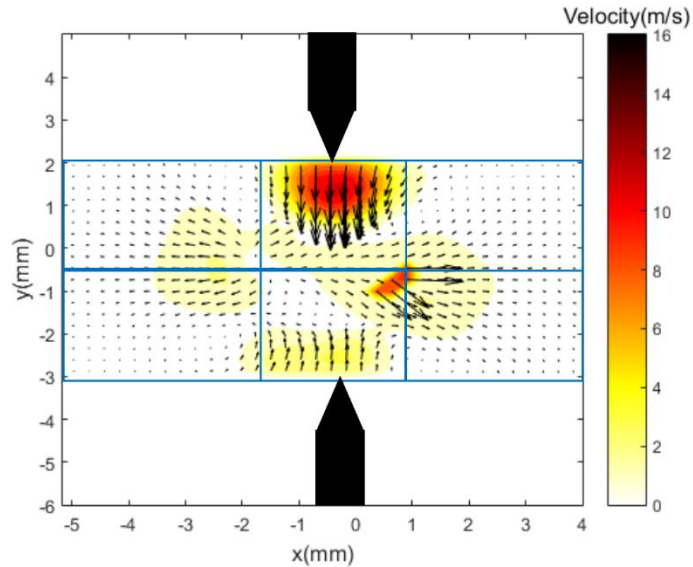
(b)

Figure 4-3: Example of region definitions for the 5 mm electrode gap

4.2.1   Examination of Ensemble Correlation, Ensemble Averaging and
Correlation of Ensemble Images as Analysis Methods for the Flow Field

Twenty separate experiments were conducted for each electrode gap. In each experiment, 100 image pairs were taken at a frequency of 10 kHz. The spark and laser are synchronized such that the spark is triggered by the first laser pulse for each of the experiments. Thus in the analysis, a set of 20 pairs of images taken approximately 200 µs after the spark are considered to be in phase, as is the case for a set of 20 pairs of images 300 µs after the spark and so on.

In order to increase signal to noise ratio and present the most accurate averaged result of all trials, so as to eliminate effects of spurious vectors due to inhomogeneous seeding or poor image acquisition in certain runs, it is necessary to determine the best method of averaging measurements from each experiment. Phase averaged correlations are thus performed. In this manner, a more collective representation of the flow field will be determined versus instantaneous depictions of the flow field which may vary from experiment to experiment. The three methods that are investigated are ensemble correlation, ensemble averaging, and correlation of the ensemble of images. Ensemble correlation

involves the sum of correlation peaks from individual experiments, to find an overall peak that is more prominent. Ensemble averaging involves the averaging of velocity vectors found from the correlation of individual image pairs to determine the mean flow field. The third method, correlation of the ensemble of images, involves superimposing the 20 image pairs to produce one image pair that contains information from all the images in the 20 experiments and performing a correlation on this ensemble image.

To assess these three averaging methods, results are studied for velocities obtained for a 5mm electrode gap, 200 µs after the spark as this is the earliest resolvable time for the flow field. Figure 4-4 shows the velocity fields obtained using the three different methods. The fields obtained using ensemble correlation (Figure 4-4(a)) and ensemble averaging (Figure 4-4(b)) resemble each other in structure. There are two regions of high velocity close to the tips of the electrodes as well as in the center of the gap on either side of the centerline defined in Figure 4-1(b). The ensemble correlated velocity field shows a maximum velocity close to 13 m/s while the ensemble averaged solution shows a maximum velocity close to 6 m/s. The flow structures remain the same between these two analyses with the flow generally moving out of the center of the electrode gap and moving toward the center of the electrode gap from the electrodes. The correlation of ensemble images shown in Figure 4-4(c) depicts a different velocity field than in the previous two cases. There is one region close to the top electrode that resembles the other two cases however the remaining 3 regions of high velocity are not present. Flow in this case is still moving from the electrodes toward the center of the spark gap, and the flow in the center is moving out toward surrounding gas.
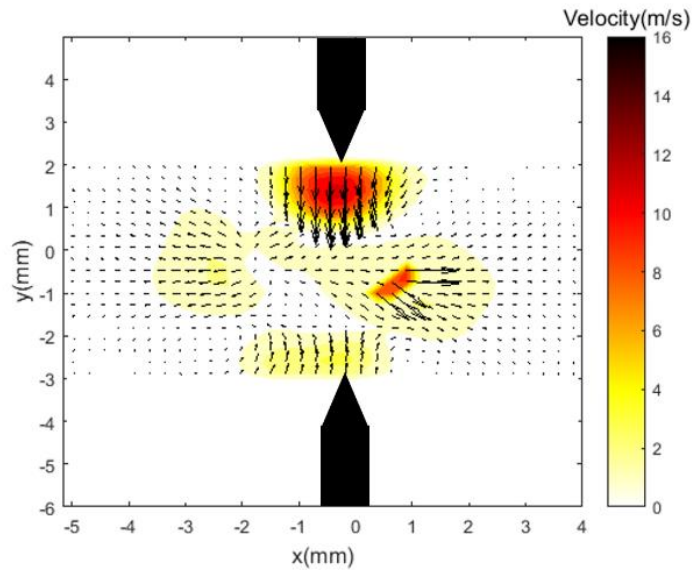
(a)
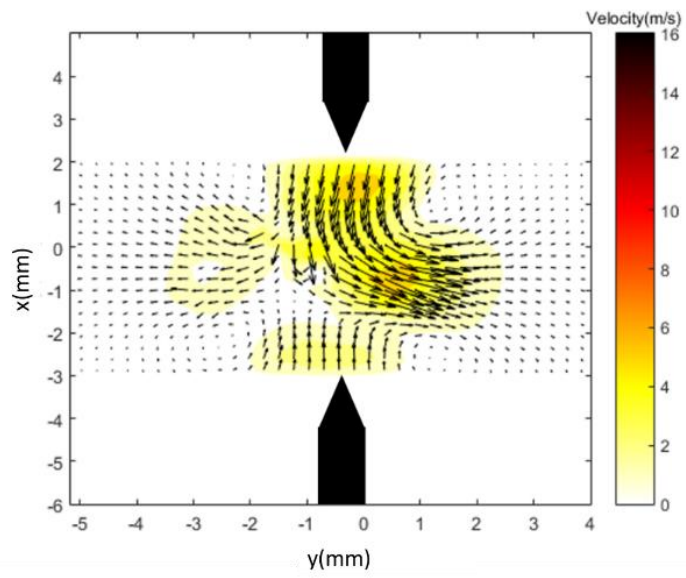
(b)
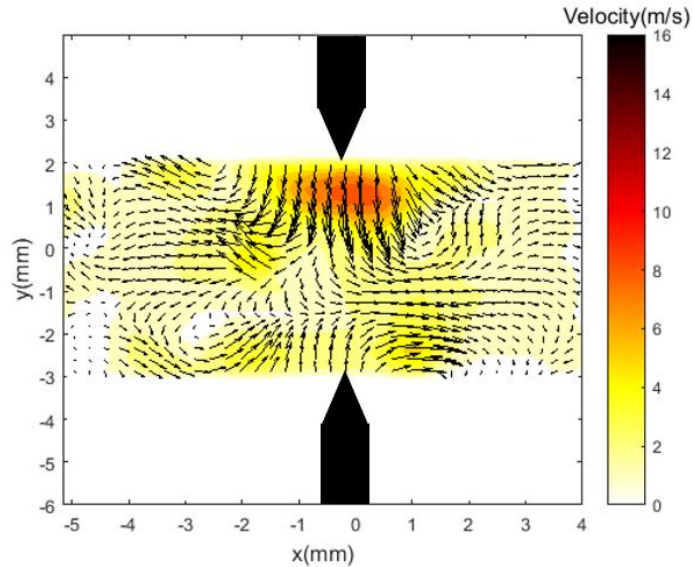
(c)

Figure 4-4: Average velocity field approximately 200 μs after the spark obtained from 20 datasets using (a) ensemble correlation, (b) ensemble averaging, and (c) correlation of ensemble image.

Similar velocity field investigations were performed at later times as well and it was found that the average velocity field generated from the correlation of ensemble images contained more outliers than the other two methods. It is possible that the high seeding density arising from the combination of 20 image pairs resulted in correlation errors. Hart [56] notes that when the seeding density is increased too much, the information between the tracer particles (spaces) is lost, which negatively affects correlation. The ensemble averaged velocity field contains more information than the ensemble correlated field. The instantaneous velocity fields are retained and can be helpful in finding Reynold's stresses and statistical information important for repeatability assessment.

Meinhert et al [68] conducted a similar experiment in a microfluidic flow channel where flow was uniform over time. The researchers performed an analysis of the three averaging techniques mentioned in order to determine which of the three produces the most reliable results and had the highest signal to noise ratio. In order to assess the quality of results, ensembles for each case were performed incrementally. That is, first 2 correlation values were added and the difference of the final velocity was compared to the true velocity

field. Correlation values from the third image pair were then summed and again compared, and so on until their 20th dataset. The same steps were used for the other two averaging techniques. The true velocity field was an ensemble correlation of their 20 datasets with smoothing. The number of velocity values across the spatial velocity field that were close to 10% of the true velocity field were then counted. From their analysis, it was evident that the ensemble correlation method produced the best results with addition of more datasets leading to improvement to valid measurements. The sum of velocity averages performed the worst, reaching about 88% validity at the second dataset then reducing to almost 60% with addition of more datasets. Meinhert et al explain that this is because the probability of spurious velocity vectors increases as the number of experiments increase. Correlation of ensemble images in this experiment performed better than the average of velocity fields, but worse than the ensemble correlation.

In the experiments conducted in this thesis, the results from correlation of ensemble images performed the worst, with approximately 2 in 5 phase averaged measurements showing presence of multiple velocity outliers. The other two measurement techniques had fewer outliers. The ensemble correlation though not helpful when information on the instantaneous velocity field is needed, seems to capture the flow field just as well as the ensemble averaged case. The ensemble correlation attempts to find the most probable displacement of particles based on information from all 20 image pairs by summing the correlation peaks from each. Unlike the velocity averaging technique, outliers in velocity data do not have as much of an impact in the final displacement due to the addition of correlation peaks and not actual velocity values. Thus, in image pairs where there are cases of spurious vectors, the effect of these images on the overall correlation is lessened if more of the remaining image pairs predict the same displacement. Signal to noise ratio is thus maximized for the ensemble correlation case.

4.2.2 Comparison of Flow Field and Voltage for Different Electrode Gaps

4.2.2.1 Velocity and Vorticity Fields for 8mm Electrode Gap

The velocity and vorticity fields induced by a spark in an 8 mm electrode gap are first studied approximately 200 μs and 400 μs after the spark breakdown. The flow field is

also investigated a long time period (4.9 ms) after the spark when it is expected that the overall flow velocity will be lower and there will be smaller flow structures throughout the region of interest.

The velocity field obtained approximately 200 µs after the spark for an 8 mm gap is shown in Figure 4-5 (a). The flow vectors near the electrodes (regions C1 and C2) are considered first. Near the upper electrode, in region C1, the flow is pointing toward the center of the electrode gap. There is a strong velocity field in the center of the gap where the zoomed in flow field shows the flow pointing downward, in the negative y direction. Adjacent to this strong velocity field is another one in the region C2 with velocity vectors pointing in the positive y direction. The flow field is somewhat symmetric about the y = 0 axis, with flow towards the electrodes and a second sink in region C2. The maximum velocity is approximately 16 m/s in both regions, but the high velocity is distributed over a slightly larger area in region C2. There is no significant effect of the spark on flow in regions R1-2 and L1-2 at this time. Approximately 400µs after the spark (Figure 4-5(b)) the flow in region C1 closest to the top electrode still moving toward the center of the electrode gap, however at a reduced velocity of about 2-3 m/s. The strong velocity fields that were present at about 200 µs after the spark are absent, however there is evidence of two wea vortices forming and moving outward toward the surrounding gas, as shown by the circled regions. Similarly for region C2, the flow close to the electrodes is moving toward the center of the electrode gap and the sink present at 200 µs is no longer there. One vortex is moving toward regions R1 and R2 and the other is moving toward regions L1 and L2. The typical flow velocity in these regions is about 1-2m/s and extends between approximately -6 mm in the x direction in L2 and -4 mm in L1. In regions R1 and R2, the effects of the spark are only seen to a distance of about 4mm in the x direction. Approximately 4.9 ms after the spark (Figure 4-5(c)), induced flow due to the spark is seen in all regions, however at much smaller magnitudes of velocity (on the order of 1 m/s or lower).

(a)

(b)

(c)
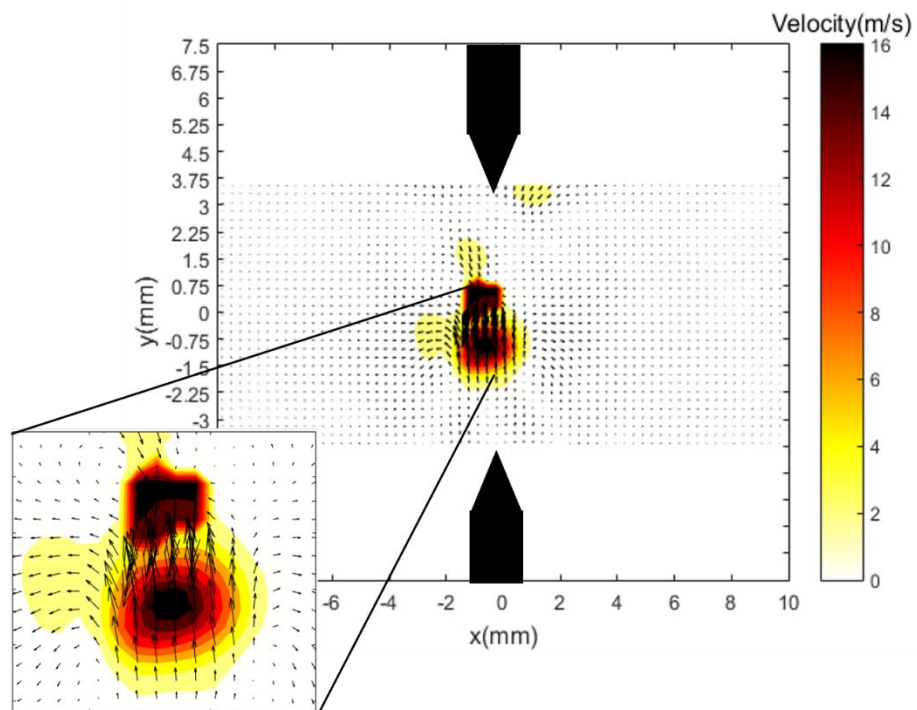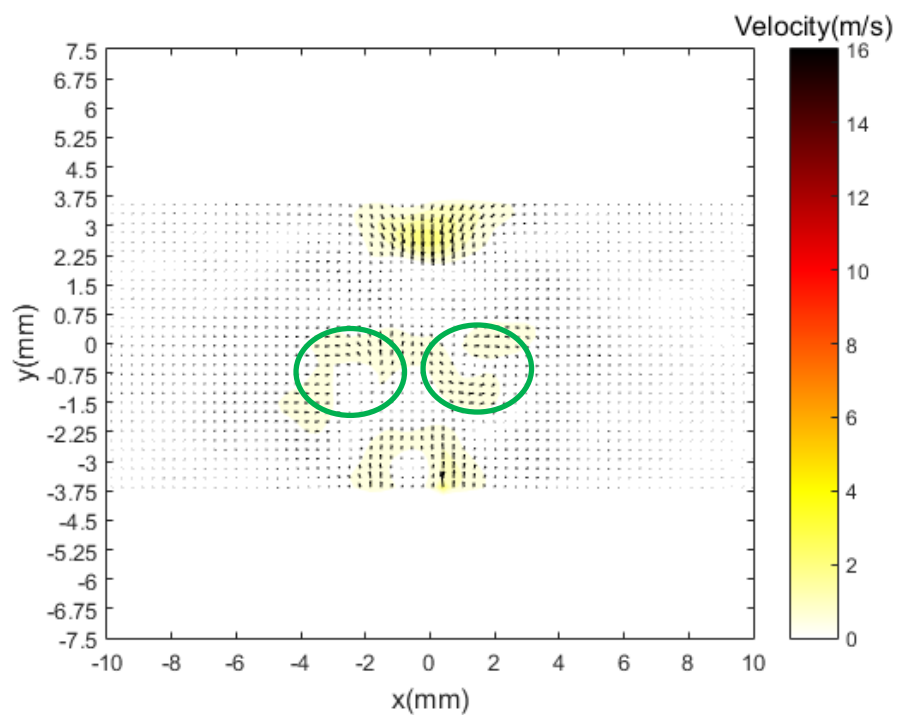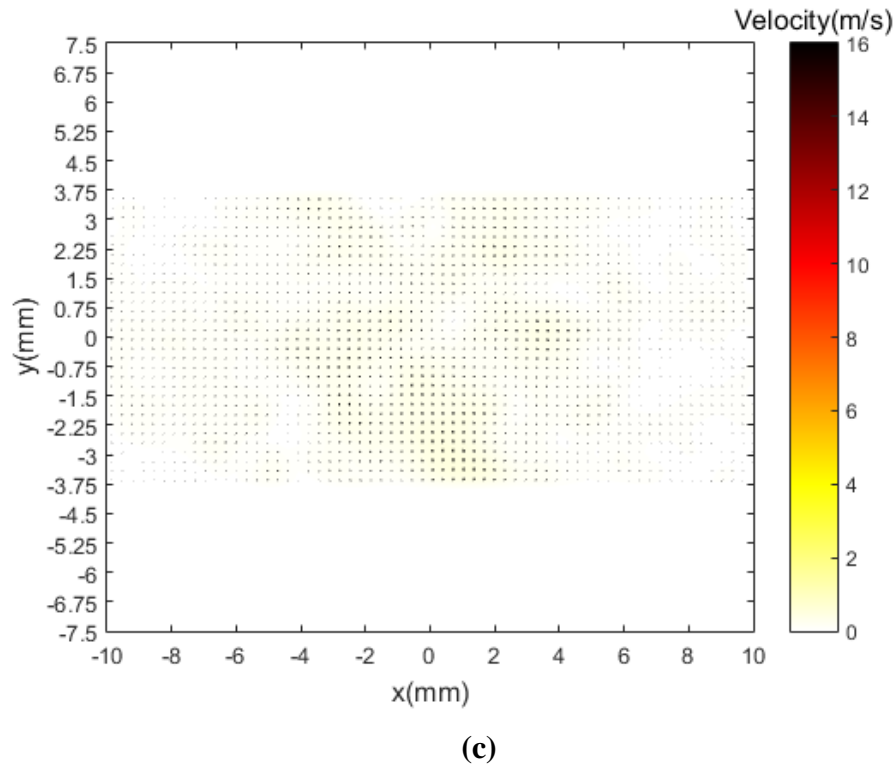
Figure 4-5: Ensemble correlated velocity fields approximately (a) 200 μs, (b) 400 μs, and (c) 4.9 ms after the spark for an 8 mm electrode gap

In the initial stages of the flow, as the hot gas kernel created by the spark plasma expands outward from the center of the gap, there is simultaneously an entrainment process occurring at a similar velocity bringing in fluid along the electrodes. This observed flow field suggests the existence of high pressures in the regions occupied by the hot gas kernel and lower pressures in the regions from which it departs. Small vortical structures are seen at later times in the flow in regions R1 and R2 as well as in regions L1 and L2 as can be inferred from the velocity plot approximately 4.9 ms after the spark. Figure 4-6(a) shows the vorticity field approximately 200 μs after the spark. There are two regions of positive vorticity in regions C1 and C2 and a region of negative vorticity of equal strength at the center of the electrode gap. The maximum vorticity observed is close to ± 8000 s^{-1}. One probable source of vorticity is baroclinic torque due to pressure and density misalignment in the expanding hot gas kernel. The formation of smaller vortices in R1, R2, L1 and L2 at later times could be attributed to viscous diffusion of the initial high vorticity developed in

the gap. More analysis at more time steps needs to be performed to understand the flow field. Correctly obtaining and interpreting the evolving velocity field will be the focus of the ongoing work.

(a)

(b)
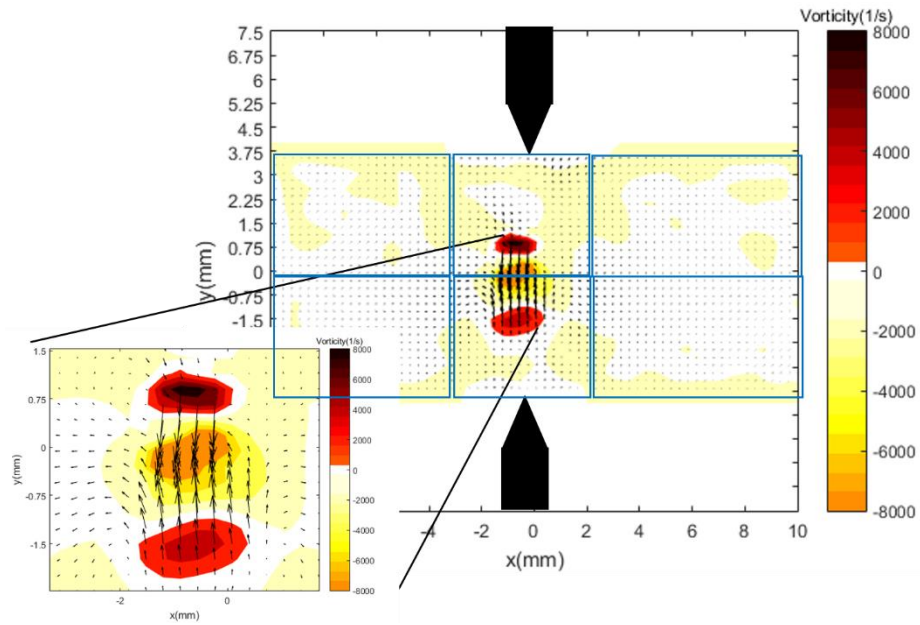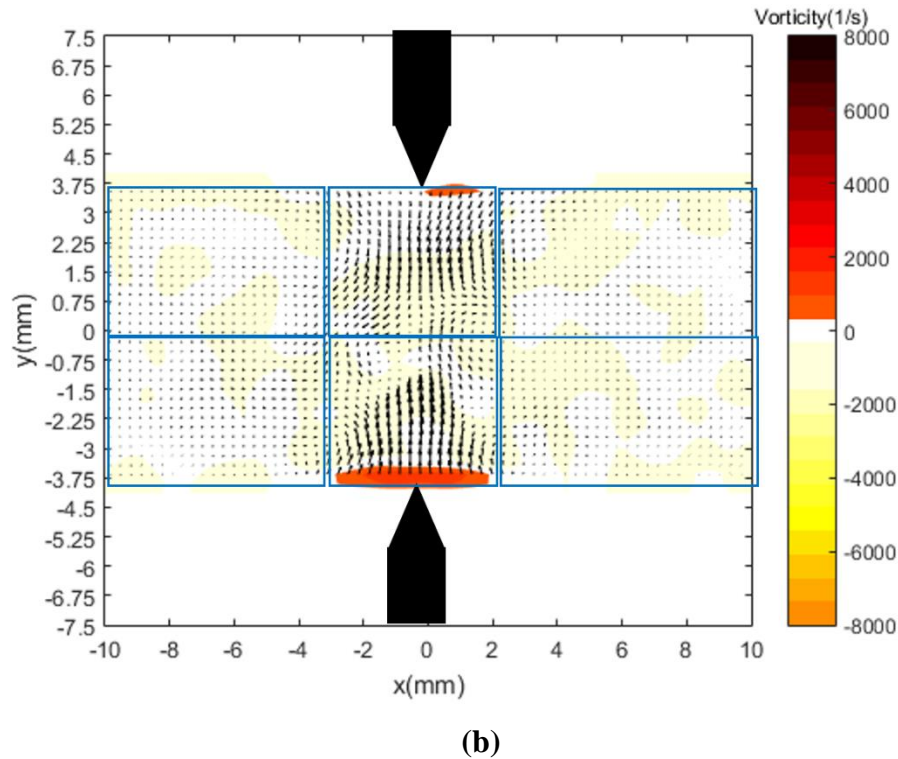
Figure 4-6: Vorticity fields approximately (a) 200 μs and (b) 1 ms after the spark for an 8 mm electrode gap

4.2.3 Comparison of Voltage and Magnitude of Induced Velocity for Different Gap Lengths

The effect of electrode gap length on the velocity field at 200 μs is considered, as the induced flow immediately following the spark will have a significant influence on the flow evolution at later times. The velocity fields at 200 μs for electrode gaps of 8, 5, and 2 mm are shown in Figure 4-7. Comparing first the 8 mm and 5 mm cases, the highest velocity concentration is within about a 2 mm region in C1 and C2 for the 8 mm case while in the 5 mm case this is only true for region C1. The induced velocity in C2 is much lower than that in C1 in the 5 mm case. Comparing the 5 mm and 2 mm cases, the induced velocity in the 2 mm case is very low and has already spread to the edges of the field of view. All three cases exhibit symmetry about the centerline of the electrodes, with the magnitude of induced velocity decreasing with decreasing electrode gap distance. From the generated flow field, it is also observed that the sinks are only seen in the 8mm gap. In the 5mm gap

and 2mm gaps, there is more flow outward than in the 8mm gap case. The presence of stronger velocity fields in the center of the electrode gap could be attributed to the larger amounts of energy deposited in the electrode gap. Another reason for the differences in flow structure could be due to the difference in shockwave structure among the three configurations. Previous research has shown that the electrode geometry used in these experiments experiences a spherical shock wave close to the surface of the electrodes and a cylindrical shock wave in the center of the gap [31]. These shock waves then affect the pressure gradient and flow field generated. Changing the gap between the electrodes would therefore have an effect on these factors. A detailed investigation of the effects of this shockwave on the flow field will be explored in future work. In all electrode configurations presented here, it is observed that there is flow towards the center of the spark gap near the electrodes.

(a)
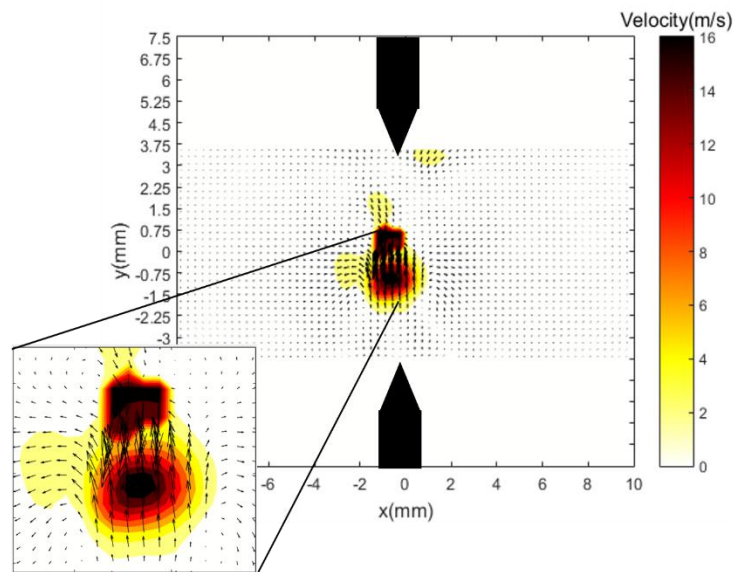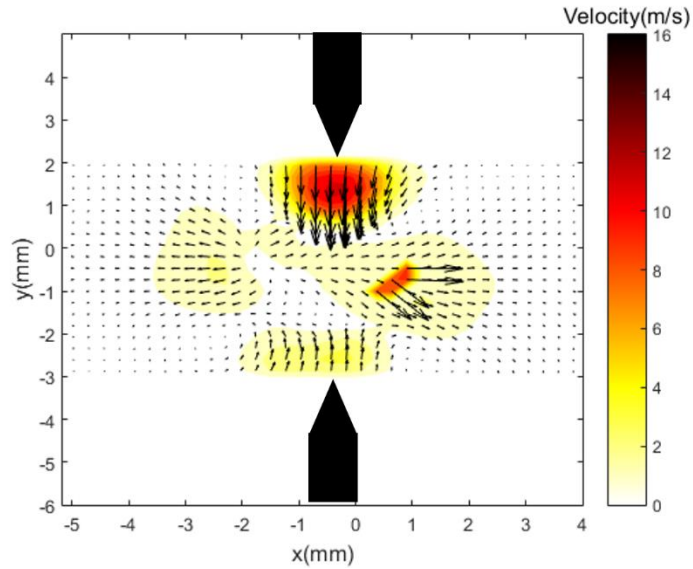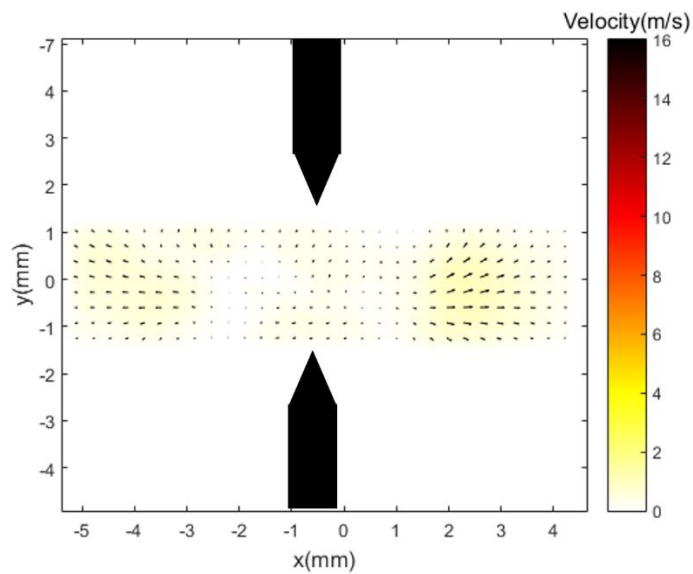
Figure 4-7: Ensemble correlated velocity fields approximately 200 μs after the spark for (a) 8 mm, (b) 5 mm, and (c) 2 mm electrode gaps

The voltage required to break down gas between two electrodes generally increases with increasing $p * d$ (pressure times distance between the electrodes), up to a certain value of $p * d$, as described by Paschen. At atmospheric pressure, and considering the gap sizes studied, it held true that for the 8 mm electrode gap, breakdown voltage was higher than

that of the 5 mm and 2 mm electrode gaps as can be seen in Figure 4-8. Higher voltage means a higher potential difference, hence greater electric field in the spark gap. For larger electrode gaps, more energy is deposited in the gap. This would explain the higher velocity fields observed in the 8 mm electrode gap compared to the 5 mm and 2 mm gaps. Higher energy deposited in the electrode gap means the plasma channel is hotter and at higher pressure. Therefore the emitted shock wave is stronger therefore inducing higher velocities and generating larger pressure gradients.
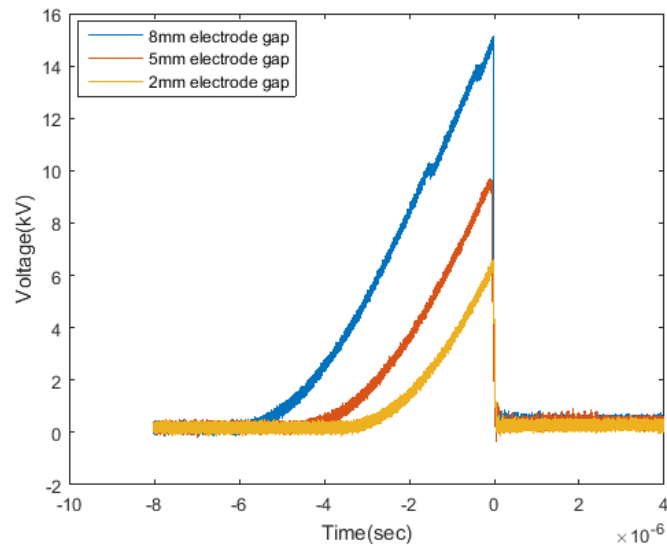
Figure 4-8: Typical breakdown voltage measurements of 8 mm, 5 mm and 2 mm electrode gaps

4.3   Temporal Evolution of the Flow Field

It is important to determine the duration over which the plasma effects remain in the surrounding gas and the magnitude of the associated velocity. The maximum overall velocity vs. time for the three electrode gaps is plotted in Figure 4-9. These values are normalized to the maximum overall velocity of each of the electrode gaps, shown in Table 4.2. The 8 mm gap, which exhibits the highest initial velocity, always shows the highest velocity decay rate. In all cases, by about 4-5 ms after the spark there is little to no change in the maximum velocity in the flow. At these times, there could still be some remaining flow effects due to the plasma, but they are not significant. All three electrode gaps show an initially high velocity 200 µs after the spark followed by a sharp decrease at about 300-

400 μs. This is more evident in the 8 mm and 5 mm electrode gap cases. Since the 2 mm electrode gap induces a very small velocity to the surrounding flow, its decrease to equilibrium velocity is not quite as sharp.

There are some fluctuations in the flow velocity at about 800 μs in the 8 mm case and at about 1200μs in the 5 mm case. These fluctuations could be due to an underestimation of velocity at prior times, that is at 700 μs and 1100 μs for 8 mm and 5 mm gaps respectively. The overall flow velocities are consistently smaller at all time steps for smaller electrode gaps.

The energy deposited in the center of the gap leads to the high velocities in this region initially. As the entrainment process from the electrodes and outward motion of the flow begins, there is a retardation in the magnitude of velocity resulting in the trend seen in the figure. The surrounding unaffected air has an average velocity on the order of 0.2 m/s. The minimum velocity values seen here that seem to stabilize for each of the electrode gaps are about 0.7 m/s, 0.5 m/s and 0.3 m/s for the 8 mm, 5 mm and 2 mm gaps, respectively. At about 10 ms after the spark, small effects of the plasma are still felt.
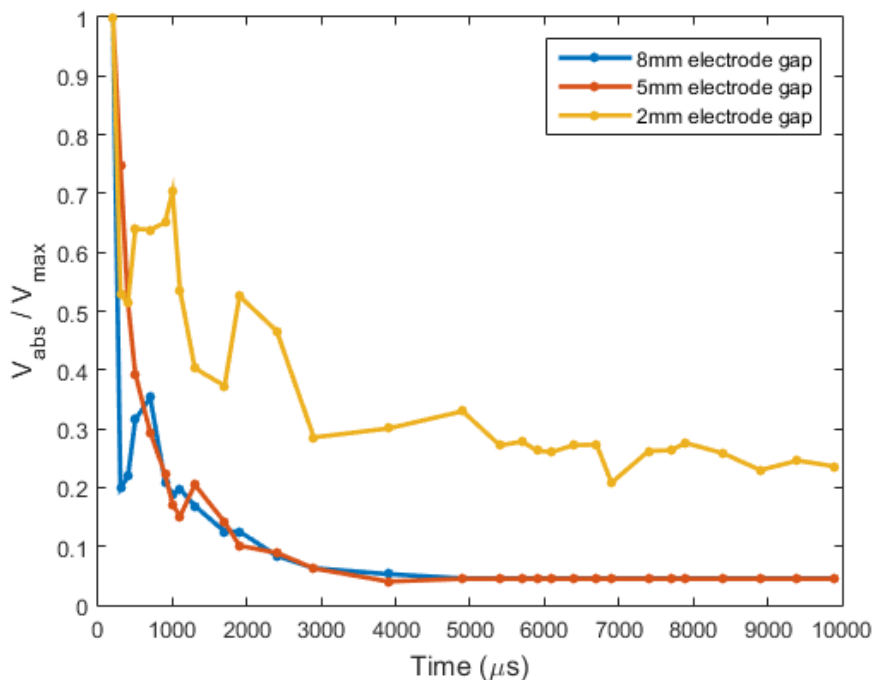
Figure 4-9: Temporal evolution of maximum overall velocity for 8 mm, 5 mm and 2 mm electrode gaps, normalized to maximum velocity

Table 4.2: Maximum overall velocities for each electrode gap

Electrode Gap	Maximum Velocity
8 mm	17.5 m/s
5 mm	11.4 m/s
2 mm	1.3 m/s

4.4   Repeatability of PIV Tests on Spark Discharge Plasma

4.4.1   Repeatability of Voltage Measurements

The first repeatability analysis was performed on breakdown voltage. The breakdown process is highly chaotic and therefore is not repeatable from test to test. The ionization channel may originate and end at different locations on the electrode surfaces and the path across the gap can vary. Therefore, it is important to consider the change in the breakdown voltage and plasma channel geometry between tests. In the current work, the variability of the breakdown voltage is assessed; the variability of the spark channel geometry will be considered in future work.

The voltage across the electrodes during the breakdown and spark discharge was measured using a Tektronix P6015A high voltage probe. The voltage waveforms from the 20 tests using an 8 mm electrode gap are shown in Figure 4-10(a). The first step after collecting voltage readings for all the experiments was to determine the time at which breakdown occurred, which varied slightly from test to test. Once the breakdown time was determined the instant corresponding to breakdown was defined as time $t = 0$ in each experiment. This indicates the first instant of spark formation that is of interest in the repeatability analysis. The time of breakdown was found by calculating the slope of the voltage plot. The rising voltage seen in Figure 4-10(a) is the measure of the output of the transformer in the spark box. At maximum voltage, breakdown occurs and the voltage drops immediately since the spark gap is now an ionized channel. The slope of the curve drops abruptly at the point of voltage breakdown and so a slope threshold of 0.12 is used to determine the time of breakdown. This number was chosen based on looking at the

slopes for different voltage values and determining the point at which the peak voltage was reached, as well as the slope of the curve after this peak voltage for each experiment. The actual slope values among experiments could differ by +/- 0.1 between experiments. The voltage during the spark for the 20 tests and the standard deviation of the voltage are shown in (b) and (c) respectively.

The standard deviation as a percentage of average voltage provides insight on the variability of the formation and geometry of the spark from test to test. As shown in the plots in Figure 4-11, the deviation from the average voltage increases as the time after breakdown increases. At early times following breakdown, the percent deviation of the voltage is between 5 and 30%. The maximum deviation observed in the 8 mm, 5 mm and 2 mm cases is 85%, 63% and 82% respectively. These deviations were observed at about 0.23ns 0.11ns and 6.5ns after the spark respectively. Most importantly, the breakdown voltage is somewhat repeatable for all three gaps, with a deviation of less than 10% at breakdown ($t = 0$). The energy deposited in the spark channel is directly related to the voltage, and the amount of energy will have a significant influence on the initial shock wave and subsequent flow evolution. Therefore, we believe that the repeatability of the breakdown voltage will have an effect on the similarity of the flow fields.
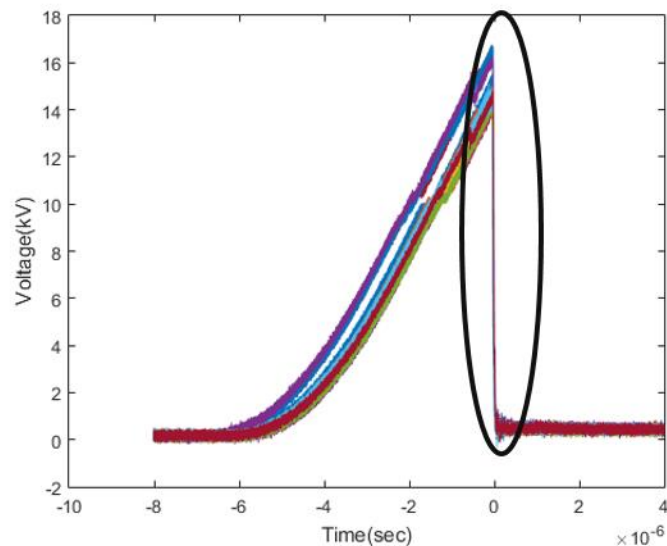
(a)
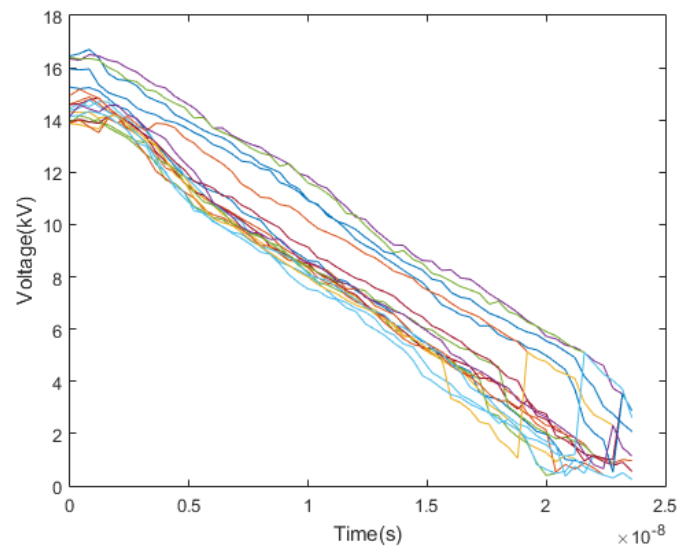
(b)
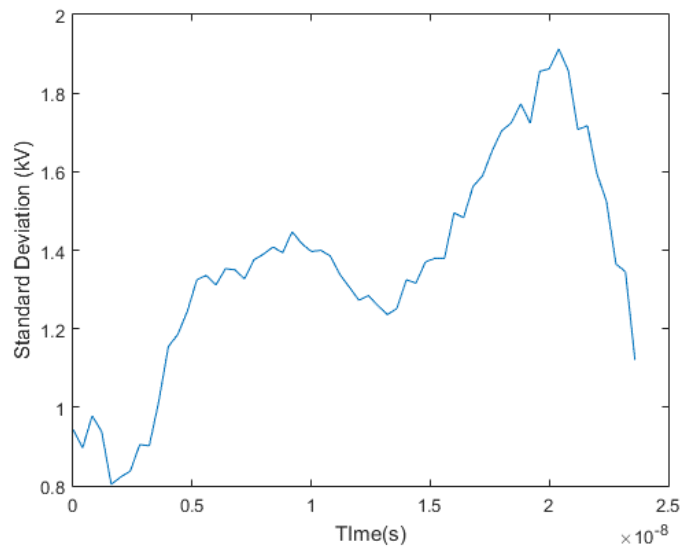
(c)

Figure 4-10: Graphs of voltage distribution for a 5mm electrode gap (a) for 20 datasets from the time the spark box is triggered to the end of the spark (b) for 20 datasets during the spark (c) for the standard deviation between the 20 datasets
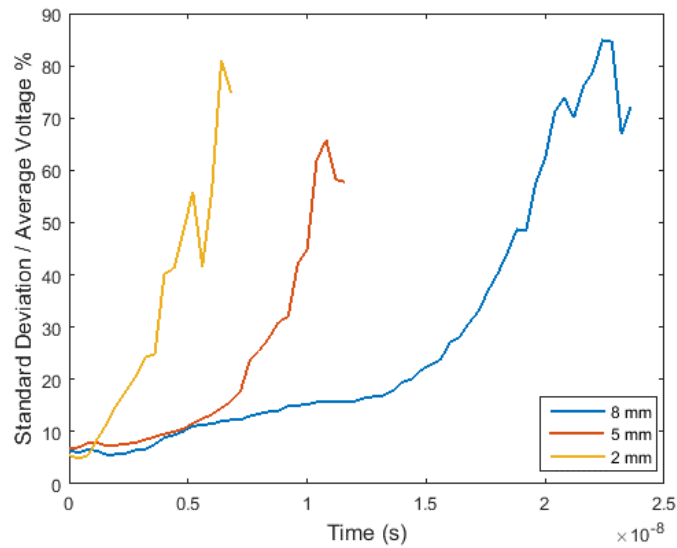
Figure 4-11: Plots of standard deviation over average voltage as a percentage for (a) 8 mm (b) 5 mm (c) 2mm electrode gaps

4.4.2   Repeatability of Flow Field

It was observed that the instantaneous flow fields generated exhibited some similarities in the flow field, while still being very different. The same is true for the magnitude of induced velocity. This section will show the results from standard deviation of velocity field for the 20 experiments conducted, for two time intervals following spark discharge. A qualitative comparison of the flow field of two experimental sets will also be performed. Figure 4-12 shows the standard deviation of velocity for an 8 mm electrode gap approximately 200 μs and 400 μs after the spark. In both cases the standard deviation is high. The maximum velocity 200 μs after the spark was about 16 m/s while that 400 μs after the spark was about 4 m/s. In the 200 μs case (Figure 4-12(a)), a large concentration of standard deviation is in the center of the spark gap where the velocities were highest. It is evident that in many of the trials the velocities in these regions were not quite as high. The absence of large standard deviations in the regions surrounding the center of the electrode gap would suggest that in most cases, approximately 200 μs after the spark, the velocities were concentrated in the center region.   Figure 4-12(b) shows the standard deviation about 400 μs after the spark. In some regions the standard deviation is actually larger than maximum velocity observed in the ensemble correlated velocity fields. Though

the deviation is still high in the center of the electrode gap where most of the flow is concentrated, there are some deviations in surrounding regions which would suggest that some experiment trials had a large concentration of spurious vectors in this region or that the flow field varied significantly and that in some instances the flow had expanded further than in others.

(a)

(b)
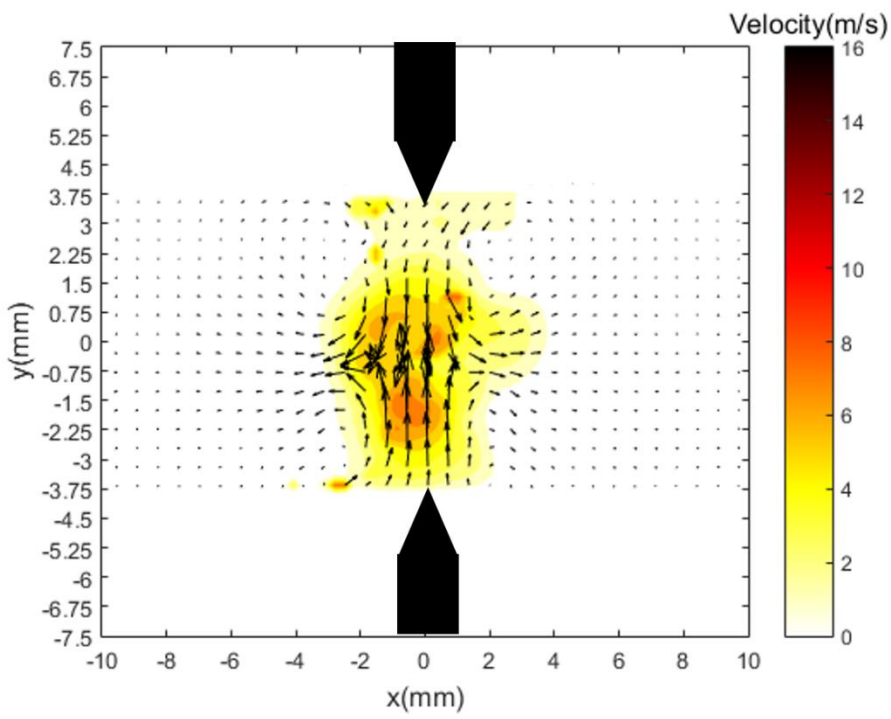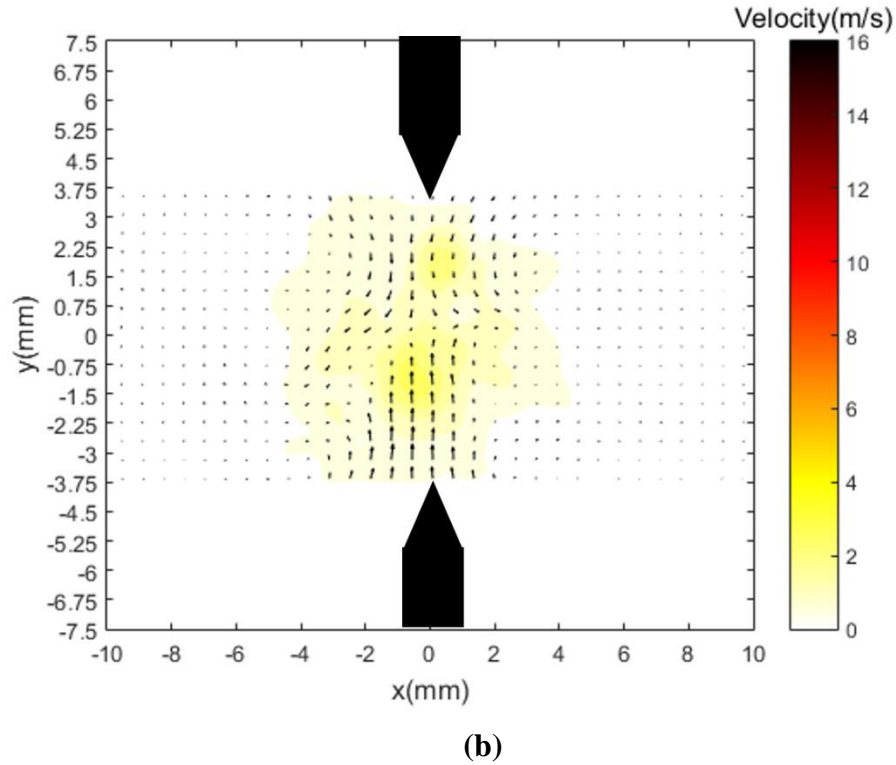
Figure 4-12: Standard deviation of 20 image pairs at approximately (a) 200 μs and (b) 400 μs after the spark for an 8 mm electrode gap

The process of spark formation is in itself random. There are random collisions between molecules and electrons that lead to the formation of the spark. By definition this randomness cannot be replicated from one experiment to the next. It would therefore follow that the induced flow field, and magnitude of the flow field would be difficult to replicate. There are still some similarities in the flow field. More than one trial, two separate regions of high velocity were observed. Some only exhibited one region of very high velocity. The gas was also observed to flow toward the center of the spark gap from the regions around the electrodes and out of the center, toward the surrounding regions in most cases. Figure 4-13 shows two instantaneous velocity fields for the 8 mm electrode gap approximately 200 μs after the spark. In both cases, the flow is concentrated in the center region of the spark gap. There the induced velocity is more "spread out" in the field in Figure 4-13(c) than the field in Figure 4-13(a). The magnitude of velocity is also fairly similar in both cases, however, (a) shows the presence of two separate regions of high velocity, one closer

to the top electrode and one closer to the bottom electrode, while (c) shows one large concentration area of flow in the center of the gap. Taking a closer look at the vorticity, (a) shows 2 clear regions of positive vorticity and one region of negative vorticity in the center of the gap. The vorticity from dataset 2 seen in (d) also shows two regions with positive vorticity in the center of the gap and one region of negative vorticity. In this dataset however, the negative vorticity is not between the two regions of positive vorticity as was the case with dataset 1. The magnitudes of vorticity are almost twice as high in dataset 1 compared to dataset 2.

(a)

(b)

(c)

(d)
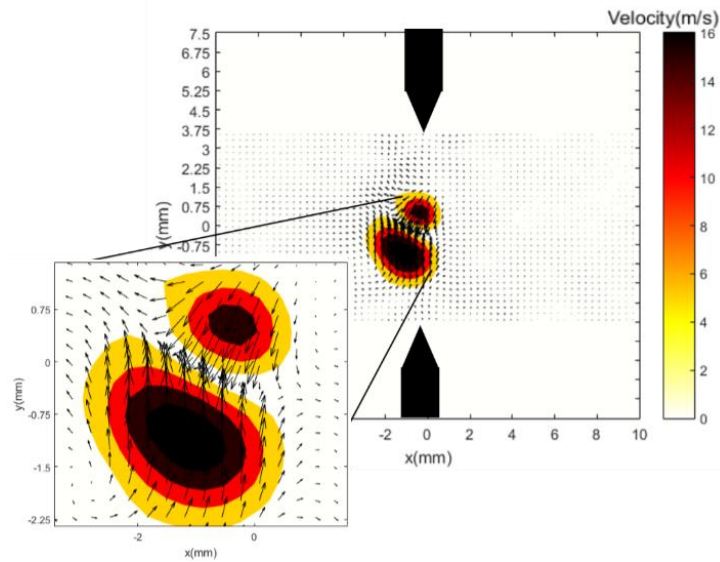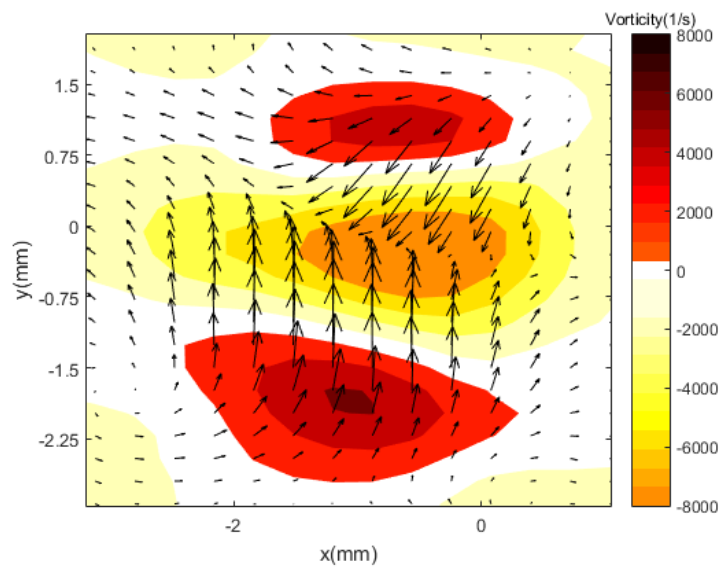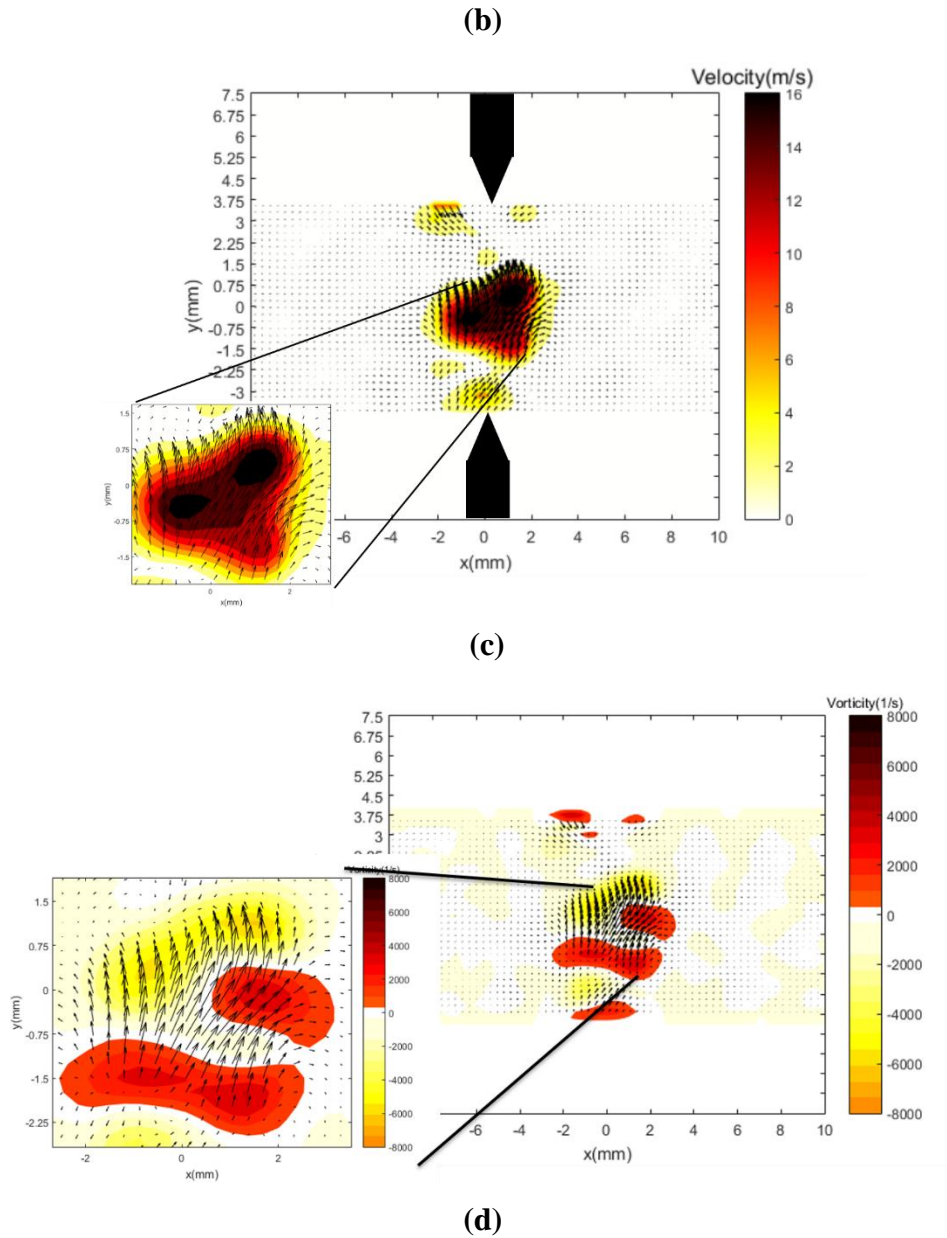
Figure 4-13: Instantaneous flow fields for an 8 mm electrode gap at approximately 200 μs after the spark of (a) velocity field for dataset 1 (b) vorticity at the center of the spark gap for dataset 1 (c) velocity field for dataset 2 (c) vorticity for dataset 2.

The experiment shows promise of repeatability in terms of velocity magnitudes and overall structure of the flow field, in that in most experiments the concentrations of high velocity are located in similar regions, such as center of electrode gap at early times or

surrounding regions at later times. Replication of exact flow field however seems to not be possible as should be expected of turbulent flows.

4.5   Summary of Results

Preliminary results have been obtained to assess the performance of the current set-up. Three different averaging techniques are tested on the flow field to determine the optimal analysis method to use. Ensemble correlation, ensemble averaging and a correlation of ensemble images are used to analyze the velocity field generated by a 5mm electrode gap. Correlation of ensemble images was found to be the least reliable, with the flow field showing no resemblance to the other two techniques. Analysis at different phases that is at later times of flow evolution, using the same technique yielded more bias velocity vectors than the other two averaging methods. Ensemble averaging and ensemble correlation both yielded similar flow fields but differed in the magnitude of velocity. The ensemble correlation showed higher magnitude of velocity compared to the ensemble averaging technique. Ensemble correlation was determined to be best method at increasing signal to noise ratio. Because spurious vectors affect the ensemble flow field less in this method, it was chosen as the primary averaging method used to show flow fields in this thesis. It should be noted however that the ensemble averaging technique is useful when preservation of the instantaneous velocity fields is needed, such as when assessing repeatability of the measurement technique or when determining Reynold's stresses.

The flow field obtained shows that the velocity of the flow field is initially highest at the center of the spark gap, with velocities up to 16m/s observed for the 8mm electrode gap case. Flow from near the electrodes moves toward the center of the gap, as flow from the center of the gap moves out to the surrounding gas. It is observed that at later times, the flow moves further out from the center of the gap, and the initial concentration of velocity at the center is significantly weaker, and eventually dissipates.

Larger magnitudes of velocity were observed when the electrode gap was higher. This was attributed to the larger amounts of energy deposited in the electrode gap which leads to hotter plasma as well as larger pressure gradients. The decay rate was also higher for the larger electrode gap of 8mm.

The flow field was found to be somewhat repeatable, with the flow generally moving to the center of the spark gap from near the electrodes at initial times, then flowing out to the surrounding gas. The exact structures could not be replicated in every experiment, with the vortical structures differing in most instantaneous cases. The voltage measurements showed about 22% deviation from the maximum in the 8mm gap and about 16% deviation in the 2mm gap, with the 5mm gap showing the least deviation at about 6%. These trends are expected due to the chaotic nature of the spark, leading to formation of turbulent flow structures and the fact that though all experiments are performed under quiescent conditions, the conditions in the chamber are never exactly the same, as well as the fact that the surface of the electrodes gets corroded due to the spark, may lead to non-repeatable measurements.

When dealing with plasma in air or other gases, there is interaction between two different media. After plasma is formed by a spark for example, there is high pressure in the region of the spark gap where hot plasma is formed. The density and pressure difference between the surrounding medium and the region with plasma can generate baroclinic torque. The misalignment of pressure and density gradients leads to unequal acceleration between the two media and vortices can be observed similar to those explained by the Kelvin-Helmholtz instability. These vortices play a key factor in changing the flow field and are mechanisms used for flow control. Viscous forces as well as convection of hot gas are also contributors to the turbulent nature of the flow field. A better characterization of the flow field is necessary before such applications can be made with the current flow control actuator. Future work will focus on analyzing and characterizing the flow field in more detail.

CHAPTER 5. CONCLUSIONS

5.1 Set-up and Preliminary Results

Preliminary experiments have been successfully performed to measure the induced flow resulting from a long-duration (~1 μs), high-energy (~50-100 mJ) spark. The spark plasma produces a high-temperature, high-pressure gas channel that immediately expands and emits a shockwave. As the shockwave propagates outward from the electrode gap, it moves flow with it at its propagation speed. Once this shock dissipates the flow continues to evolve due to pressure gradients created in the wake of the shock. The focus of the current work was the development of particle image velocimetry (PIV) methods for measuring these plasma-induced flows.

A 2-D PIV set-up was used to image the flow field. The first part of the current effort required the determination of the appropriate laser pulse to use for each electrode configuration. A 20 μs pulse separation was used for the 8 mm electrode gap, a 30 μs pulse separation was used for the 5 mm electrode gap and a 40 μs pulse separation was used for the 2 mm electrode gap. In all cases but the 2 mm electrode gap, the maximum displacements observed were about $1/4^{th}$ of the window size.

The appropriate PIV processing parameters were determined for accurate measurement of all length and time scales in the flow fields. These parameters were found by investigating the effect of the size of the interrogation window on the resolution of the flow field. The smallest interrogation window size capable of resolving the flow field at early times (approximately 200 μs) after the spark was determined to be a 48 x 48 pixel window. A constant window size of 48 x 48 was then used to perform the rest of the analysis. A set of 20 experiments were performed at each of three spark gap lengths: 2, 5, and 8 mm. Three different averaging techniques were investigated to increase the signal-to-noise ratio (SNR). The ensemble correlation, ensemble averaging and correlation of

ensemble images each showed some similarities in the flow field they were evaluating, however the correlation of ensemble images consisted of more outliers compared to the other two techniques at the different phases of analysis. Prior work performed on a steady flow showed results favoring the ensemble correlation technique, however no such consensus on the best averaging method was reached from the current tests. It remains to be determined if averaging over the flow fields would accurately describe the flows, and if so, more analysis needs to go into determining the best technique to use.

The flow fields calculated using PIV were assessed to provide insight on the ability of the PIV to capture the main flow structures. Approximately 200 μs after the spark, the PIV results show flow moving inward from the electrodes and jetting out from the center of the electrode gap. Approximately 500 μs after the spark, the PIV results still show flow moving inward from the electrodes, however at a lower magnitude that earlier times. About 4.9 ms after the spark, the PIV images show very low magnitudes of velocity with small, weak vertical structures, and the flow has expanded further outward from the spark gap. Further analysis of the PIV results suggests that, at early times (on the order of 200 μs after the spark) the high flow velocities are initially concentrated at the center of the electrode gap, which is particularly obvious in the 8 mm electrode gap. In the 5 mm electrode gap, a region of high velocity is observed close to the top electrode. In the 2 mm electrode gap case, the flow has already expanded out to the edges of the specified region of interest, though at a much lower magnitude of velocity. The shock structure and hence the flow field is greatly affected by the electrode configuration [31] and the flow field at very short times after the spark needs to be studied in more detail to better understand the flow physics. The flow field was observed to decay over time due to entrainment, with the 8 mm electrode gap exhibiting the fastest decay rate. In all electrode gaps, about 4-5 ms after the spark, little change in the maximum induced velocity is observed.

A repeatability investigation showed that the breakdown voltage was somewhat repeatable (less than 10% variation) for a given gap size but there were high deviations in voltage from the mean voltage near the end of the spark discharge. While the breakdown voltage, and hence the energy deposited in the plasma, was relatively repeatable, the flow field exhibited more significant deviation from the average velocity. For example, for the

8 mm electrode gap, the standard deviation of the velocity was high as 70-90% of the average velocity.

The current system shows capabilities of measuring the flow field about 200μs after the spark. The flow trends suggest that the initial energy deposited in the spark gap slowly dissipates as it moves out of the gap to the surrounding regions until equilibrium is achieved in the region. The processing techniques used to generate the flow field are capable of evaluating the complex nature of the flow induced by the spark plasma. A procedural analysis of the best parameters to use when analyzing this flow structure at the given time scales has proven useful in finding the limits of the current set-up.

5.2   Future Work

These flow fields have not been studied or measured in detail before, and significant work remains to be done to understand the flow fields, the physics behind the features observed, and how to control the induced flow and use it for flow control purposes. Obtaining accurate, resolved measurements of the induced flow field is the critical first step. Simultaneous PIV and schlieren images will provide further insight into the flow field and the schlieren images will provide some qualitative validation of the PIV analysis. An attempt has been made to understand the nature of the flow field using a 2-D PIV system. The flow itself is however 3-D in nature, with a lot of out of plane motion. An analysis at different planes will be performed to characterize the three dimensionality of the flow field as best as possible. This will be performed by taking PIV measurements of the flow field, a few mm forward and backward of the spark gap. The sensitivity of this system to determine the actual distances to analyze will need to be determined. The flow immediately following the spark <10μs after the spark needs to be captured and examined to determine the factors influencing the flow field at later times. In order to do this, a laser capable of pulsing at higher frequencies is necessary to illuminate the flow field.

A more sophisticated pulser to generate sparks will be incorporated into the set-up. This will allow the investigation of the effect of the electrical pulse parameters on the induced flow field. An NSP-3300 nanosecond high voltage pulser by Eagle Harbor Technologies will be used. The pulse parameters can be independently varied, with

voltages up to 35 kV, pulse widths from 20 to 100 ns, and output frequencies up to 400 kHz. The pulse voltage and current waveforms will be measured using high-speed probes and used to calculate the energy deposited in the plasma. Current as well as voltage measurements will need to be taken to determine the energy deposited in the spark gap, and enable the use of this information to quantify the body force generated by the system. Full characterization of the flow field will also involve determination of Reynold's shear stresses.

Continual improvement to the processing techniques used to analyze the images will be made. The two pulses used to illuminate image pairs differ in intensity. This then means that the tracer particle intensities used to correlate images between the two image pairs is different. Thresholding techniques can be used to set particle intensities to be similar, such that light intensities above a certain threshold are reduced or eliminated. This ensure that similar tracer particles between image pairs can be more easily identified and correlated. This also eliminates background reflections. These methods were attempted in this thesis, however a detailed analysis was not performed, therefore the thresholds and effects of higher or lower thresholds was not determined. An improved mask will also need to be employed such that the region surrounding the electrodes is resolved, to observe flow features in these regions.

Measurement uncertainties will also be quantified. This will involve further assessment of the repeatability of the experiment as well as uncertainties associated with the PIV processing techniques implemented in PRANA. The uncertainty analysis would involve determination of the error associated with each vector value that is processed. This would be useful when a full quantitative characterization of the flow field is performed.

A full characterization of the flow field generated will thus be performed in the future with improvements to the set-up.

REFERENCES

LIST OF REFERENCES

[1]   ATAG, "Facts and Figures", *Air Transport Action Group* [Online webpage], URL: http://www.atag.org/facts-and-figures.html [cited 11 June 2015].

[2]   US DOT, "Airline Fuel Cons and Consumption", *Bureau of Transportation Statistics* [online database], URL: http://www.transtats.bts.gov/fuel.asp [cited 11 June 2015].

[3]   ICAO Secretariat, "Aircraft Technology improvements", *ICAO Environmental Report 2010* [online report], URL: http://www.icao.int/environmental-protection/Documents/EnvironmentReport-2010/ICAO_EnvReport10-Ch2_en.pdf [cited 11 June 2015].

[4]   NASA, "Winglets Save Billions of Dollars in Fuel Costs", *NASA Technology Transfer Program* [Online news article], URL: https://spinoff.nasa.gov/Spinoff2010/t_5.html [cited 11 June 2015].

[5]   Moreau, E. (2007). "Airflow Control by Non-Thermal Plasma Actuators," *Journal of Applied Physics D: Applied Physics,* Vol. 40, 605-36

[6]   Gad-el-Hak. M. (2000) *Flow Control: Passive, Active, and Reactive Flow Management*, Cambridge University Press.

[7]   Liepmann, H. W., and D. M. Nosenchuck. (1982) "Active control of laminar-turbulent transition." *Journal of Fluid Mechanics* 118: 201-204.

[8]   Fransson, J. H., Talamelli, A., Brandt, L., & Cossu, C. (2006). Delaying transition to turbulence by a passive mechanism. *Physical review letters*, *96*(6), 064501.

[9]   Flatt, J. "The history of boundary layer control research in the USA", in *boundary later and flow control,* ed. G.V. Lahmann, Vol. 1, 1961, pp. 122-143.

[10]   H. Schlichting. *Boundary Layer Theory,* 8th ed., Springer-Verlag, New York, 2000

[11]   Hwang, S. D., & Cho, H. H. (2003). "Effects of acoustic excitation positions on heat transfer and flow in axisymmetric impinging jet: main jet excitation and shear layer excitation." *International Journal of Heat and Fluid Flow*, *24*(2), 199-209.

[12]   Bityurin, V. A., Bocharov, A. N., & Lineberry, J. (2005). MHD flow control in hypersonic flight. *AIAA Paper*, *3225*, 2005.

[13]   Bradshaw, P. (1985). *An introduction to turbulence and its measurement,* Pergamon Press Ltd.

[14]   Roth, J. R. (2003). "Aerodynamic Flow Acceleration Using Paraelectric and Peristaltic Electrohydrodynamic Effects of a One Atmosphere Uniform Glow Discharge Plasma," *Physics of Plasmas*, Vol. 10(5), 2117-26.

[15]   Sosa, R., Moreau, E., Touchard, G., and Artana, G. (2004). "Stall Control at High Angle of Attack with Periodically Excited EHD Actuators," *35th AIAA Plasmadynamics and Lasers Conference (Portland, OR, 28 June – 1 July 2004)* AIAA Paper 2004-2738.

[16]   Post, M. L. and Corke, T. C. (2004). "Separation Control on High Angle of Attack Airfoil Using Plasma Actuators," *AIAA Journal*, Vol. 42(11), 2177-84.

[17]   Goossens, M. (2012). *An introduction to plasma astrophysics and magnetohydrodynamics* (Vol. 294). Springer Science & Business Media.

[18]   Roth, J. R., Sherman, D., Wilkinson, S. (1998). "Boundary Layer Flow Control with One Atmosphere Uniform Glow Discharge," 36th AIAA Aerospace Science Meeting and Exhibit, AIAA Paper 1998-0328..

[19]   Corke, T. C., Enloe, C. L., and Wilkinson, S. P. (2010). "Dielectric Barrier Discharge Plasma Actuators for Flow Control," *Annual Review of Fluid Mechanics*, Vol. 42, 505-29.

[20]   Thomas, F. O., Corke, T. C., Iqbal, M., Kozlov, A., and Schatzman, D. (2009). "Optimization of Dielectric Barrier Discharge Plasma Actuators for Active Aerodynamic Flow Control," *AIAA Journal*, Vol. 47(9), 2169-78.

[21]   Cattafesta, L. and Sheplak, M. (2009). "Actuators and Sensors." *Fundamentals and Applications of Modern Flow Control,* edited by R. D. Joslin and D. N. Miller, Progress in Astronautics and Aernautics (231), AIAA, Inc., Reston, VA, 1-20.

[22]   Cybyk, B. Z., Wilkerson, J. T. and Grossman, K. R. (2004). "Performance Characteristics of the Sparkjet Flow Control Actuator," *2nd AIAA Flow Control Conference (Portland, OR, 28 June – 1 July 2004)* AIAA Paper 04-2131.

[23]   Rathay, N. W., Boucher, M. J., Amitay, M., and Whalen, E. (2012). "Performance Enhancement of a Vertical Stabilizer Using Synthetic Jet Actuators: No Sideslip," *50th AIAA Aerospace Sciences Meeting (Nashville, TN, 9-12 January 2012)* AIAA Paper 2012-0071.

[24]   Lambert, T. J., Vukasinovic, B., and Glezer, A. (2012). "Unsteady Aerodynamic Flow Control of a Wire-Suspended, Moving Axisymmetric Body," *50th AIAA Aerospace Sciences Meeting (Nashville, TN, 9-12 January 2012)* AIAA Paper 2012-0073.

[25]   Narayanaswamy, V., Raja, L. L., and Clemens, N. T. (2012). "Control of a Shock/Boundary-Layer Interaction by Using a Pulsed-Plasma Jet Actuator," *AIAA Journal*, Vol. 50(1), 246-9.

[26]   Reedy, T., Kale, N. V., Dutton, J. C. and Elliott, G. S. (2012). "Experimental Characterization of a Pulsed Plasma Jet," *50th AIAA Aerospace Sciences Meeting (Nashville, TN, 9-12 January 2012)* AIAA Paper 2012-0904.

[27]   DeBlauw, B., Elliot, G. and Dutton, C. (2014). "Active Control of Supersonic Base Flows with Electric Arc Plasma Actuators," *AIAA Journal, 1-16*.

[28]   Utkin, Y.G., Keshav, S., Kim, J.-H., Kastner, J., Adamovich, I. V. and Samimy, M. (2007). "Development and Use of Localized Arc Filament Plasma Actuators for High-Speed Flow Control," *Journal of Applied Physics D: Applied Physics,* Vol. 40, 605-36.

[29]   Samimy, M., Kearney-Fischer, M., Kim, J.-H., and Sinha, A. (2012). "High-Speed and High-Reynolds-Number Jet Control Using Arc Filament Plasma Actuators," *Journal of Propulsion and Power*, Vol. 28(2), 269-80.

[30]   DeBlauw, B., Sanders, B., Glumac, N., Dutton, C., and Elliott, G. (2012). "Correlation Between Emission, Electric, and Flow Properties of Arc Filament Plasma Actuators," *50th AIAA Aerospace Sciences Meeting (Nashville, TN, 9-12 January 2012)* AIAA Paper 2012-0190.

[31]   Bane, S. P. M., Ziegler, J. L., and Shepherd, J. E. (2014). "Investigation of the Effect of Electrode Geometry on Spark Ignition," *Combustion and Flame,* DOI: *10.1016/j.combustflame.2014.07.017.*

[32]   Leonov, S. B., Isaenkov, Y. I., Firsov, A. A., Nothnagel, S. L., and Gimelshein, S. F. (2010). "Jet Regime of the Afterspark Channel Decay," *Physics of Plasmas, 17*, 053505.

[33]   Shurupov, M. A., Leonov, S. B., Firsov, A. A., Yarantsev, D. A., and Isaenkov, Y. I. (2014). "Gasydynamic Instabilities During Decay of the Submicrosecond Spark Discharge Channel," *High Temperature*, Vol. 52(2), 169-178.

[34]   Macheret, S. (2015) "Plasmas and Electric Discharges". *Lecture Notes: Streamers, Coronas and Sparks*

[35]   Belmouss, Mounia (2015), "Effect of Electrode Geometry on High Energy Spark Discharges in Air," *MS Thesis,* Purdue University School of Aeronautics and Astronautics

[36]   Adrian, R. J. (2005). "Twenty years of particle image velocimetry," *Experiments in fluids*, *39*(2), 159-169.

[37]   Melling, A. (1997). "Tracer particles and seeding for particle image velocimetry." *Measurement Science and Technology*, *8*(12), 1406.

[38]   Hamdi, M., Havet, M., Rouaud, O., & Tarlet, D. (2014). "Comparison of different tracers for PIV measurements in EHD airflow". *Experiments in Fluids*, *55*(4), 1-12.

[39]   Raffel, M., Willert, C. E., Wereley, S. T., & Kompenhans, J. (2007). *Particle Image Velocimetry: A Practical Guide*. Springer.

[40]   Ragni, D., Schrijer, F., Van Oudheusden, B. W., & Scarano, F. (2011). "Particle tracer response across shocks measured by PIV." *Experiments in fluids*, *50*(1), 53-64.

[41]   Urban, W. D., & Mungal, M. G. (2001). "Planar velocity measurements in compressible mixing layers." *Journal of Fluid Mechanics*, *431*, 189-222.

[42]   Urban, W. D., (1999). "Planar velocity measurements in compressible mixing layers." *PhD Thesis,* Stanford University.

[43]   Tarlet, D., Bendicks, C., Roloff, C., Bordás, R., Wunderlich, B., Michaelis, B., & Thévenin, D. (2012). "Gas Flow Measurements by 3D Particle Tracking Velocimetry Using Coloured Tracer Particles." *Flow, turbulence and combustion,88*(3), 343-365.

[44]   Zouzou, N., Dramane, B., Moreau, E., & Touchard, G. (2011). "EHD flow and collection efficiency of a DBD ESP in wire-to-plane and plane-to-plane configurations". *Industry Applications, IEEE Transactions on*, *47*(1), 336-343.

[45]   Hecht, J., *Understanding lasers: an entry-level guide.* John Wiley & Sons, Vol. 21, 2011, pp 21-59, pp 210-245, pp 129-169.

[46]   Svelto, O., Hanna, D. C., *Principles of lasers*. Plenum Publishing Corp. Fourth Edition, 1998, pp 375-430.

[47]   Wereley, S. (2014) "Particle Image Velocimetry". *Lecture Notes: Particle Image Pattern Tracking*

[48]   Willert, C. E., & Gharib, M. (1991). Digital particle image velocimetry. *Experiments in fluids*, *10*(4), 181-193.

[49]   Dabiri, D. (2006). "Cross-correlation digital particle image velocimetry—a review."*Turbulencia. ABCM, Curitiba*, 155-199.

[50]   Keane R. D. & Adrian, R.J, (1992). "Theory of cross-correlation analysis of PIV images," *Applied Scientific Research 49:* 191-215

[51]   Smith, S. W. (1997). The scientist and engineer's guide to digital signal processing.

[52]   Eckstein, A., & Vlachos, P. P. (2009). Digital particle image velocimetry (DPIV) robust phase correlation. *Measurement Science and Technology*, *20*(5), 055401.

[53]   Overmars, E. F. J. Bias errors in PIV: the pixel locking effect revisited. EFJ Overmars, NGW Warncke, C. Poelma and J. Westerweel.

[54]   Voges, M., Klinner, J., Willert, C., Beversdorff, M., & Schodl, R. (2007, September). "Assessment of powder-based seeding materials for PIV applications in transonic, supersonic and reacting flows", In *7th International Symposium on Particle Image Velocimetry, Rome, Italy*.

[55]   D'Entremont, J.H., Gejji, R., Venkatesh, P.B., and Bane, S.P.M. (2014). "Plasma Control of Combustion Instability in a Lean Direct Injection Gas Turbine Combustor," 52nd AIAA Aerospace Sciences Meeting (National Harbor, MD, 13-17 January 2014) AIAA Paper 2014-0622.

[56]   Hart, D. P. (2000). "PIV error correction." *Experiments in fluids*, *29*(1), 13-22.

[57]   Charonko, J., Drew, B., Raben, S. (2011). "PRANA PIV Manual", *Aether Lab*, Virginia Polytechnic Institute and State University.

[58]   Scarano, F., & Riethmuller, M. L. (1999). "Iterative multigrid approach in PIV image processing with discrete window offset." *Experiments in Fluids*, *26*(6), 513-523.

[59]   Westerweel, J., Geelhoed, P. F., & Lindken, R. (2004). "Single-pixel resolution ensemble correlation for micro-PIV applications". *Experiments in Fluids*, *37*(3), 375-384.

[60]   Delnoij, E., Westerweel, J., Deen, N. G., Kuipers, J. A. M., & Van Swaaij, W. P. M. (1999). "Ensemble correlation PIV applied to bubble plumes rising in a bubble column". *Chemical Engineering Science*, *54*(21), 5159-5171.

[61]   Li, F., Gao, C., Zheng, B. R., & Wang, Y. S. (2013). "Study of the Boundary Layer on a Plate Aerodynamically Induced by Multiple DBD Plasma Based on PIV". *Applied Mechanics and Materials*, *421*, 163-167.

[62]   Kriegseis, J., Schwarz, C., Tropea, C., & Grundmann, S. (2013). "Velocity-information-based force-term estimation of dielectric-barrier discharge plasma actuators". *Journal of Physics D: Applied Physics*, *46*(5), 055202.

[63]   Bordás, R., Hagemeier, T., Wunderlich, B., & Thévenin, D. (2011). "Droplet collisions and interaction with the turbulent flow within a two-phase wind tunnel". *Physics of Fluids (1994-present)*, *23*(8), 085105.

[64]   Tarlet, D., Bendicks, C., Roloff, C., Bordás, R., Wunderlich, B., Michaelis, B., & Thévenin, D. (2012). "Gas Flow Measurements by 3D Particle Tracking Velocimetry Using Coloured Tracer Particles." *Flow, turbulence and combustion*,*88*(3), 343-365.

[65]   Atten, P. (1996). Electrohydrodynamic instability and motion induced by injected space charge in insulating liquids. *Dielectrics and Electrical Insulation, IEEE Transactions on*, *3*(1), 1-17.

[66]   Masati, A., Sydney, A.J., and Sedwick, R.J. (2014). "Parametric Study of Particle Size for Plasma Actuator PIV Measurements," *52nd AIAA Aerospace Sciences Meeting (National Harbor, MD, 13-17 January 2014)* AIAA Paper 2014-0147.

[67]   Hinds, W. C. (2012). *Aerosol technology: properties, behavior, and measurement of airborne particles*. John Wiley & Sons.

[68]   Meinhart, C. D., Wereley, S. T., & Santiago, J. G. (2000). "A PIV algorithm for estimating time-averaged velocity fields." *Journal of Fluids Engineering*, *122*(2), 285-289.

APPENDICES

Appendix A   Validation of Experimental Set-up

The next step of the experiment procedure was to validate the implementation of the PIV measurement technique using a known flow. In this case, the exit flow from a sonic nozzle was used. A bent tube with a 4 mm inner diameter was flared at 37° and connected to the sonic nozzle as shown in Figure 5-1. The sonic nozzle was connected to the shop air via flexible tubing. A pressure regulator was placed between the shop air and the sonic nozzle and the pressure reading was used to determine properties of the flow entering the nozzle. The exit was enclosed in a small chamber that was seeded using smoke particles.

Figure 5-1: Experimental aparatus for sonic nozzle flow test.

The pressure at the nozzle inlet is known and is considered to be the total pressure. The sonic nozzle is designed so that incoming flow is accelerated to Mach 1 at the throat (choked flow). The sonic nozzle used here has a diameter of 0.014 inches (0.000356 m) at the throat. The benefit of using a sonic nozzle is that since the flow is choked at the throat, the mass flow rate at this point is known, and then continuity can be used to calculate the velocity of the jet exiting the tube connected to the sonic nozzle.

The jet exiting the tube will spread due to fluid entrainment, but for the validation it is assumed that immediately upon exiting the jet diameter is equal to the tube inner diameter (0.004 m). It is necessary to determine the theoretical exit velocity from the 0.004 m tube for comparison to the experimental data. To do this, the mass flow rate exiting the

nozzle is written using the ideal gas law and the definition of the Mach number (assuming a perfect gas):

$$\dot{m} = \frac{P}{\sqrt{RT}} M \sqrt{\gamma} A_v \qquad (5.1)$$

Using isentropic relations, the pressure P can be rewritten in terms of total pressure and temperature:

$$P = P_t \left(\frac{T}{T_t} \right)^{\frac{\gamma}{\gamma-1}} \qquad (5.2)$$

and the temperature ratio can be written in terms of Mach number:

$$\frac{T}{T_t} = \left(1 + \frac{\gamma-1}{2} M^2 \right)^{-1} \qquad (5.3)$$

Substituting equations 2 and 3 into equation 1 and setting $M = 1$ (choked flow at the throat), the final expression for the mass flow rate exiting the sonic nozzle is obtained:

$$\dot{m} = \frac{A_v P_t C_d}{\sqrt{T_t}} \sqrt{\frac{\gamma}{R}} \left(\frac{\gamma+1}{2} \right)^{\frac{-\gamma+1}{2(\gamma-1)}} \qquad (5.4)$$

Using Equation (5.4) the average velocity of the jet at the exit was determined to be 14.7 m/s.

The region surrounding the jet was enclosed and seeded. Two images were taken in double frame mode at 3000 fps (equivalent to 6000 fps in single frame mode). The laser was pulsed at 3000 Hz. The DaVis software was used to process the images and the resulting average velocity of the jet was determined to be 9m/s ± 4m/s with some regions of the flow displaying a maximum velocity of 15 m/s. As can be seen in Figure 5-2, the velocity of the jet closest to the exit is between 14-16 m/s, much closer to the theoretical value than the average value. A likely cause of the large discrepancies is that as the flow moves further from the exit the jet entrains air and transitions to a turbulent jet. The result was considered to be sufficient as the purpose of this step was to ensure that a reasonable order of magnitude of velocity was being measured with the PIV set-up.
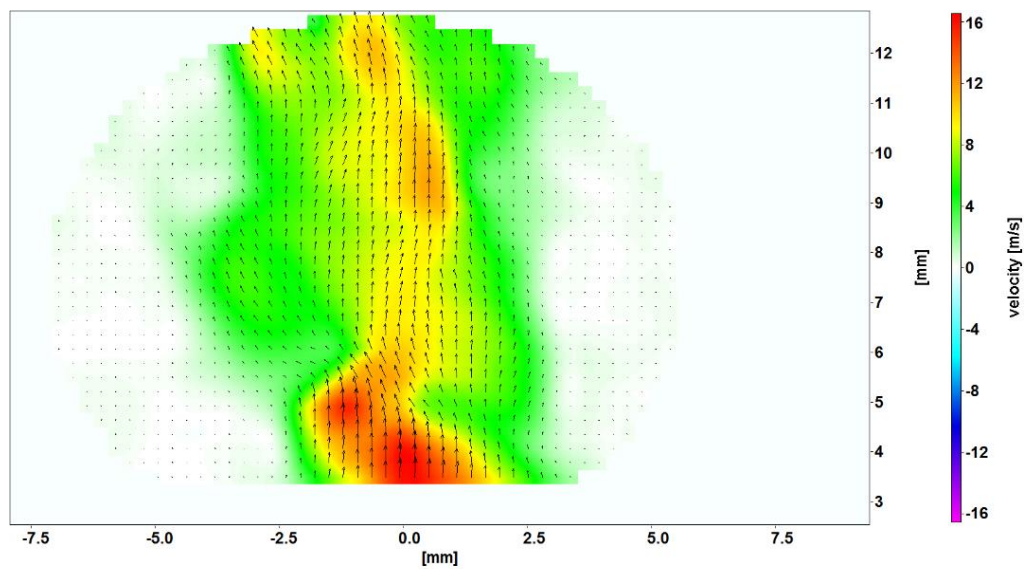
Figure 5-2: Velocity vectors obtained using PIV for the air jet exiting the sonic venturi.

Appendix B   Standard Operating Procedures

B.1.   High Voltage Discharge Box SOP

1. Verify that the box is unplugged from the wall and that the power switch is turned to "Off."

2. Place the electrodes/spark gap on an insulating surface, and ensure that there are no metallic or conducting objects near the gap.

3. Connect output cables to electrodes/spark gap connections. Also connect the high voltage probe to the output connections.

- tighten all connections with a wrench

- once tightened, cover exposed connections with high voltage insulating putty

Note that if the output cables are already connected to the electrodes then the above steps are unnecessary.

4. Ensure that the power supply and the delay generator are connected to the appropriate inputs on the HV discharge box.

5. Turn on the power supply and verify that the voltage is approximately 5V. Turn the power supply back off.

6. Check the settings on the delay generator. If they have changed since the last use, you must check the DG output on the oscilloscope.

In the absence of a delay generator, a function generator is used. Note the following settings for the function generator:

a) The default settings for operation of the spark have been saved in "BS03" settings of the function generator. To access these settings turn on the function generator and push the store/recall button, Select the recall option (second from the left) and navigate to the 1st setting (BS03). Navigate to the recall selection and push the corresponding button.

The following settings should match "BS03"

- Pulse waveform in Burst mode (1 cycle)

- Frequency = 1 Hz

- Amplitude = 5 V$_{PP}$

- Offset = 2.5 V$_{DC}$

- Width = 100 ms

7. Plug in the HV discharge box power cord and turn the power switch to "On."

8. Ensure that no one is standing within 2 feet of the spark gap and inform bystanders before arming the circuit.

9. Turn on the power supply to arm the circuit, connect the BnC cable to the function generator and when ready, push the output button to fire.

10. After firing, press the output button (light should go off) and unplug the BNC cable from the function generator.

11. Turn off the 5V power supply to unarm the circuit, unplug the power cord from the wall socket, and turn the power switch to "Off."

12. Before touching any conductor/electrode, use the grounding sticks to discharge any remaining electrical energy in the circuit (touch one stick to the HV electrode and then the other stick to ground).

B.2. Nd:YAG Laser SOP

Operation

1. Put safety glasses on before entering room (safety glasses located in room 18B) and keep eyewear on while using the laser. Verify that everyone in the room has on safety eyewear.

2. Ensure that chain is secured on both doors and that they are both locked.

3. Verify that the laser power supply is unplugged and the laser is off.

4. Verify that the chiller is turned off.

5. Turn on the chiller using the up arrow key marked "On/Off". If there is a beeping noise, fill distilled water into the chiller to "max" marker.

6. Turn on the "main power switch" – the main power switch light turns on and the water pump of the cooling system starts.

7. Turn the key-switch into the "On" – positions (vertically).

8. Push the "Start" – button - The white signal on the lamp on the laser head shines.

9. Open the EdgeWave software to control the laser by double clicking the icon on the desktop.

10. Ensure that there are no errors in the laser by running a Query from the installed software on the computer.

11. Ensure that the currents for both laser heads is at or below 20A.

12. Select the "laser on" push button on the software on the computer used to run the laser.

13. The white signal in the lamp on the laser head should now be blue. – if this is red, hit the laser off button and check to see if there are any errors using the commands described in the laser manual (included in this folder).

14. In order to begin lasing, turn the Amperage up slightly for the first laser head(Laser 1) (in increments of 5A). The laser head begins lasing at 43A.

15. Then slowly raise the current on the second laser head (Laser 2), once again in small increments. This laser head begins lasing at 39A.

16. Before running tests, turn both these to maximum current and use power meter to ensure that Laser is lasing well with no power losses.

17. Use this minimum lasing power (or slightly higher brighter beams) to align the laser sheet (see "Creating the laser sheet" for instructions on this.

18. When not using the laser, turn the laser off using the push buttons on the laser software. Remember to run the current down slowly (in decrements of 5A) until about 20A, after which the "Laser off" Push button can be pressed.

19. When finished with the laser, turn the key to the off position.

20. Turn the "main power switch" off

21. Turn the chiller off by pushing the "up" arrow.

<u>Aligning/changing beam overlap</u>

22. The frequency doubled beams from both independent oscillators are combined in the side box.

23. In order to align or change the overlap lose the four screws on the corner of the combination box (narrower box) and take the cover off.

24. You now have access to the opto-mechanic components.

25. The two adjustable holders can be used to align or change the overlap of the two beams.

<u>Creating the laser sheet</u>

26. Turn on the laser to minimum lasing power as per the instructions in "Operation" above.

Appendix C   Determination of Optimal Tracer Particles for Characterization of Flow Control Actuators based on Spark Discharge Plasmas

I.   Introduction

In cases where flow is perturbed by electrical force, such as in plasma flow control, and analyzed using tracer particles, it is necessary to consider the effect of electrohydrodynamics (EHD) on these tracer particles and determine the best properties suited to the experiment in question. The three main aspects of the tracer particles that are of interest are: The size of the tracer particles should be small enough to follow the flow accurately but also large enough to be visible by the camera [38], [39]; The size and density of the particles need to be such that sedimentation and inertial effects can be neglected [39]; The physical characteristics of the particles should be such that charge and polarization effects are negligible [39].

PIV as a velocity measurement technique is indirect in its measurements. This means, that the PIV method actually collects velocity data for the tracer particles used to seed the test section as opposed to the actual fluid in the flow. This means that the particles used to trace the fluid should follow the fluid flow pattern almost if not exactly. This makes choosing the right tracer particles to use for seeding an important step before performing PIV.

II.   Theoretical and Experimental Analysis of Tracer Particles

N. Zouzou et al noted that for particles larger than 2μm, field charging was dominant while for particles smaller than 0.2 μm, thermal diffusion was observed [44]. Numerous experiments have been done with seeding particles between this range, with no noticeable deviation in flow patterns in results from the expected [61], [62]. M. Hamdi et al used a needle/ring electrode to create EHD flow to study different tracer particles. The PIV measurements taken were compared to pressure measurements taken by a pitot tube to check if there was significant velocity lag [38] . This paper calculated Stokes number,

Archemedes number and mobility (non-dimensional values) to compare the different seeding particles and sizes of these particles. The stokes number determines "the ability of the tracer particles to adapt to abrupt changes in flow velocity" [63], [64]. For Stokes number less than or equal to 10^{-3} the deviation of tracer particles is negligible [64]. The Archimedes number is used to predict whether or not sedimentation will occur due to difference in density between the tracer particle and the fluid [64]. It was determined by Tarlet et al that if this number is less than 10^{-2} then sedimentation effects can be neglected. The mobility ratio determines how well the particle mobility matches that of the fluid in the presence of an electric field [65]. Atten et al determined that when mobility ratio is greater than or equal to 3, the mobility of the particles is influenced more by the fluid than the electric field.

Figure 5-3 below has been obtained from M. Hamdi et al to show the different seeding particles various experiments used. Information on the different particle sizes as well as some densities can be seen, however it should be noticed that no information on the charging properties of these particles is given. Few researchers have sought to determine when particles get charged [66] however the most conclusive results found so far have been by M. Hamdi et al.

Publication	Tracer	Mean diameter (μm)	Density (kg m^{-3})	Application in EHD
Léger et al. (2001)	Dielectric oil smoke	0.3	–	PIV
Chang et al. (2005)	TiO_2	0.2	–	PIV
Podlinski et al. (2005)	TiO_2	<1	–	PIV
Balagopal and Go (2011)	Incense	1	1,100	PIV
Niewulis et al. (2009)	Cigarette smoke	<1	–	PIV 3D
Ullum et al. (2004)	Olive oil smoke	0.5–2	900	PIV 3D
Moghaddam et al. (2006)	Glass microspheres	2.5	–	LDV
	Polystyrene nanospheres	0.5	–	LDV
Kotsonis and Ghaemi (2011)	Olive oil	1	–	PIV
Kriegseis et al. (2012)	(DEHS) aerosol	0.9	–	PIV
Joussot et al. (2013)	Olive oil smoke	1	–	LDV
Benard et al. (2013)	Dielectric oil (Odina919)	0.3	–	PIV

Figure 5-3: Tracers and their Sizes Obtained from a Literature Review Performed by M. Hamdi et al [38], [38].

According to M. Hamdi et al, there are two ways in which ion attachment is possible, diffusion charging and field charging. Diffusion charging is only considered

for tracer particle sizes with diameters less than 0.1 μm [66]. Therefore, considering only field charging for the particles being researched in this literature review, consider the two figures below. shows the different particles that were analyzed as well as their sizes and the calculated 3 dimensionless values discussed above. Figure 5-4 shows that the Stokes number (St) in most cases was similar but that cigarette smoke and conductive oil smoke had better values (close to 10^{-3}). Archimedes number was relatively small in all cases but for EMS and conductive oil smoke particles. Mobility ratio for all particles was much greater than 3 but for EMS and conductive oil smoke.

Tracer	Diameter (μm)	Density (kg m^{-3})	Stokes number (St)	Archimedes number (Ar)	Mobility ratio (M)
Cigarette smoke	0.3–1	1,900	6.9×10^{-3}–5.7×10^{-2}	1.8×10^{-6}–6.8×10^{-5}	228–20.5
Incense smoke	0.8	1,100	2.2×10^{-2}	2×10^{-5}	27.9
Microballoons	1	1,800	5.4×10^{-2}	6.4×10^{-5}	17.4
EMS	20	70	1.3×10^{-2}	2×10^{-2}	4.18×10^{-2}
Conductive oil smoke	0.6–4	1,360	1.6×10^{-2}–5.7×10^{-3}	1.1×10^{-2}–3.1×10^{-3}	8.8×10^{-2}–1.44×10^{-2}
TiO$_2$ metallic particles	0.7	4,000	6.3×10^{-2}	4.9×10^{-5}	24.1

Figure 5-4: Values of Dimensionless Parameters St, Ar and M for Various Particles [38]

Figure 5-5 below shows that for the currents shown, the SiO$_2$, incense and TiO$_2$ tracer particles are negligibly affected by the field charge and follow the flow almost exactly.
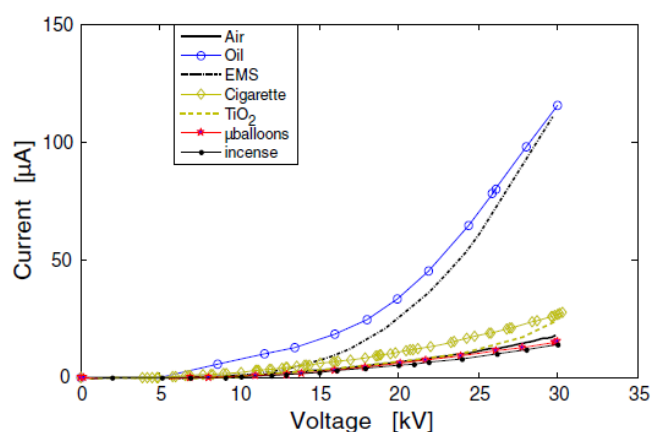

Figure 5-5: Current Voltage Characteristic Curves with Different Tracers [38]

From Figure 5-5 above it can also be noticed that the solid particles in general follow the flow better in the presence of an electric field. According to Hamdi et al and Hinds, the oil particle gets charged in its entire volume and the charge is up to 3 times that of solid particles. Hamdi et al also note that particle charging is predominant at

the tips of the needles where the electric field strength is highest and reduces significantly as the particles move away from the tip and becomes negligible as far enough distances.

Hamdi et al then compared the PIV for the three tracer particles mentioned above that followed the flow best to pitot tube measurements and in all three cases it was found that the PIV measurements agree well with the pitot tube measurements. Hamdi et al suggest that of the three tracers, SiO_2 is most recommended as they have better laser light reflection and thus produce better images. These are however expensive and it is recommended that they be recycled.

III.   Conclusion

This literature review concludes that particles sizes between 0.2 μm and 2 μm are ideal for seeding flow to be analyzed using PIV in the presence of an electric field. Particles between these sizes correspond to minimal particle charging and thermal diffusion. It was further found that most particles analyzed behaved within the prescribed limits of the non-dimensional Stokes number, Archimedes number and mobility ratio except for EMS and conductive oil smoke particles. Current – voltage characteristics were then plotted and it was noted that silicon dioxide, titanium dioxide and incense were the least affected by the electric field and almost accurately followed the flow. Comparisons were made of the PIV velocities obtained for these particles to pitot tube measurements and in all three cases the velocities were similar to the pitot tube measurements of the flow. Silicon dioxide (of diameter 1 μm) has been determined to be the best of the three as it reflects light best to produce good images used in PIV. It is however the most expensive of the three seeders and should be recycled when possible.